Strategic inversion approach to improve the resistivity image of an offshore CO_2 storage site

Lone Zimmer Bøe

Thesis submitted for the degree of
Master of Science in Geophysics
60 credits

Department of Geosciences
Faculty of Mathematics and Natural Sciences

UNIVERSITY OF OSLO

June 1, 2017

UiO : Department of Geosciences
University of Oslo

Strategic inversion approach to improve the resistivity image of an offshore CO_2 storage site

Master thesis in Geophysics
June 2017

Lone Zimmer Bøe

Strategic inversion approach to improve the resistivity image of an offshore CO_2 storage site

Supervisors: Joonsang Park (NGI) and Valerie Maupin (UiO)

http://www.duo.uio.no/

Printed: Reprosentralen, University of Oslo

Preface

This thesis was written as part of a two year master study in Geosciences at the University of Oslo (UiO), to complete an MSc degree in Geophysics. The thesis represents 60 ECTS credit points, which is equivalent to a one year study.

The study was conducted in collaboration with the Norwegian Geotechnical Institute (NGI), under supervision of Joonsang Park (NGI) and Professor Valerie Maupin (UiO). The data for the study was provided by NGI, who received access to it through the CO2ReMoVe project and Statoil. The study is sponsored by FME SUCCESS, a research center for subsurface CO_2 storage, under grant 193825/S60 from the Research Council of Norway (RCN).

Acknowledgements

First of all, I would like to thank my supervisor at NGI, Joonsang Park, for valuable guidance and support during my work with the thesis, for always being available for questions, and for gladly sharing of his knowledge and experience. I would also like to thank my supervisor at UiO, Valerie Maupin, for valuable guidance and feedback on my work, and thank you to NGI and FME SUCCESS for providing the data for the study.

I want to thank Malte Vöge at NGI for the guidance and technical support related to NGI's in-house software, and Guillaume Sauvin for providing depth converted seismic data. Also, a big thanks to everyone at the PGG department, and the rest of NGI, for being so welcoming and including during my time there. Finally, I would like to thank my friends at the university for helpful discussions and encouragements, and my family for patience and great support.

Abstract

In 2008 a controlled-source electromagnetic (CSEM) dataset was acquired from the Sleipner field area in the North Sea, where every year since 1996 nearly one million tons of CO_2 has been injected into the Utsira Formation. The Norwegian Geotechnical Institute (NGI) has successfully inverted the dataset and located the CO_2 plume and its resistivity profile, but there are various challenges related to the inversion. These challenges include a pipeline network at seabed, interfering with the CSEM signal and generating artefacts in the resistivity image of the subsurface. Also, the shallow water in the area causes a strong airwave influence on the data, the injected CO_2 shows up as a weak resistivity anomaly, and the target appears shallower than expected in the resistivity models. The objective of this study is to finalize the inversion study of the Sleipner CSEM dataset for NGI, under FME SUCCESS, and to establish an inversion strategy that can be applied to solve the different challenges related to inverting the dataset.

Data analysis and tuning of different inversion parameters are conducted in order to establish an inversion strategy for the dataset. Inversion parameters such as the inversion grid, offset range, a priori model, data density and error estimates are optimized, with respect to the response and location of the resistivity anomaly of the CO_2 plume. The strategy also includes a systematic method developed to identify and filter out data strongly influenced by the pipelines, which reduces the artefacts in the resistivity image generated by the pipelines significantly. The inversion strategy is applicable to CSEM data from similar case studies, and for hydrocarbon exploration and production in similar environments.

An inversion study of synthetic time-lapse CSEM data, generated for a CO_2 storage case study in the Skade Formation, is also conducted. This demonstrates the value of a baseline survey, which was not acquired in the Sleipner project. The inversion strategy for the Sleipner dataset was successfully applied for the synthetic Skade data, with some modifications, and some of the findings in the inversion study of the Sleipner data are further examined in the synthetic Skade data inversion study.

Contents

List of figures

1 Introduction

1.1 Motivation and background

In 2008 a controlled-source electromagnetic (CSEM) dataset was acquired by Electromagnetic Geoservices (EMGS) from the Sleipner field area in the North Sea (Figure 1.1), where every year since 1996 nearly one million tons (Mt) of CO_2 has been injected into the Utsira Formation (Fm). The Norwegian Geotechnical Institute (NGI) has been studying the dataset in order to validate the feasibility of using marine CSEM data for CO_2 injection monitoring in offshore reservoirs. They have successfully inverted the dataset and located the CO_2 plume and its resistivity profile, but there are various challenges related to the inversion (Park et al., 2011; Park et al., 2013; Park et al., 2014). The water depth is only around 80 m, which causes strong influence from the generated airwaves. There is also a pipeline network at seabed, which interferes with the CSEM signal and generates artefacts in the resistivity image of the subsurface. Also, the injected CO_2 shows up as a weak resistivity anomaly, and the target appears shallower than expected in the inversion results.

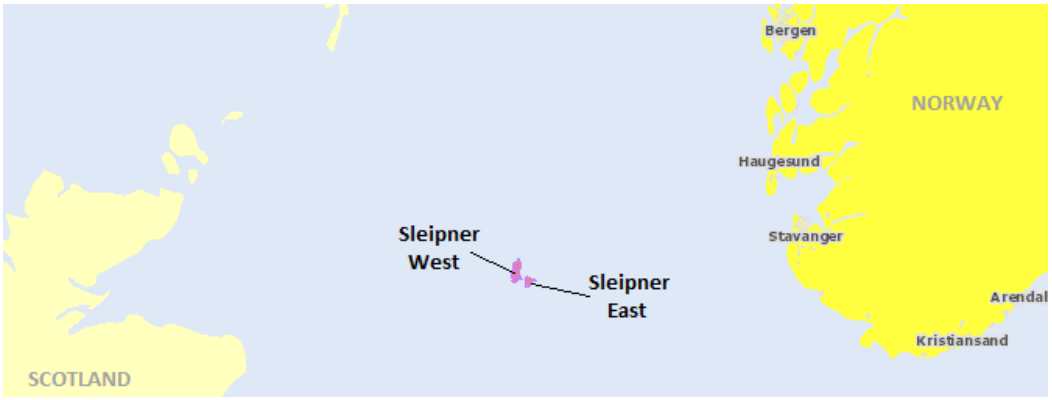

Figure 1.1: The location of the Sleipner field, North Sea (Norsk Petroleum, 2017).

The purpose of this MSc thesis is to establish an inversion strategy which can be applied in order to resolve some of the challenges described above. These challenges may also be present in other places on the Norwegian Continental Shelf (NCS), and relevant when it comes to hydrocarbon exploration and production as well. An inversion strategy may therefore be useful for different applications in the industry.

At the moment NGI is also conducting studies related to the planning stage of potential future CO_2 storage projects, similar to the Sleipner CO_2 project, under FME SUCCESS. In 2011 the Norwegian Petroleum Directorate (NPD) developed a CO_2 storage atlas for the NCS, requested by the Ministry of Petroleum and Energy. The atlas documents the distribution and properties of potential sites for long-term storage of CO_2, including saline aquifers (bodies of porous and permeable sedimentary rocks with

saline water in the pore space that is in communication throughout) and abandoned oil and gas fields (NPD, 2011). Diffferent candidates have been evaluated in terms of sealing capacity, reservoir quality and injectivity, and the Skade formation is considered to be among the best candidates. NGI is currently involved in the assesment of this potential injection site, and producing and analyzing both synthetic seismic and CSEM data, based on simulations of CO_2 injections done by Uni Researh CIPR (Centre for Integrated Petroleum Research). An inversion study based on synthetic CSEM data from the Skade case study is also included in the thesis, to demonstrate the potential and sensitivity of a time-lapse CSEM survey.

1.2 Objective

This MSc thesis have been conducted to finalize the inversion study of the Sleipner CSEM dataset for NGI, under FME SUCCESS. The main objective of the thesis is to establish an inversion strategy that can be applied in order to resolve some of the challenges related to the inversion of the dataset, and improve the resulting resistivity image. In addition, an inversion study of synthetic data from the Skade CO_2 storage case study have been conducted, to study the potential and sensitivity of the CSEM method for a similar scenario, but at a much earlier stage in the project life.

1.3 Carbon capture and storage

Carbon capture and storage (CCS), sometimes referred to as carbon capture and sequestration, is a process where CO_2 is captured, transported and stored, normally in an underground geological formation. Detailed information about this process is provided by e.g. the Global CCS institute (2016a), and IPCC (2005). CO_2 produced by large industrial plants is captured, compressed for transportation, and then injected into a carefully evaluated geological formation for permanent storage. CCS serves as a mitigation measure to prevent large amounts of the greenhouse gas to be released into the atmosphere, contributing to a reduced rate of global warming.

Globally there are around 21 large-scale CCS projects in operation or under construction, and the project at the Sleipner site was not only the first demonstration of CCS technology for a deep saline reservoir, but is also one of the largest CCS projects in the world (Global CCS Institute, 2016b).

1.4 The Sleipner CO_2 storage project

The Sleipner CO_2 storage project was initiated by Statoil in 1996, and is a pilot project for monitoring CO_2 stored in the subsurface. The details and configuration of the project is described by the Global CCS institute (2016b), while experiences related to CO_2 monitoring gained at the site can be found in

e.g. Arts et al. (2008), and quantification of the CO_2 volume by analyzing 4D seismic data in Chadwick, Arts, & Eiken (2005).

The Sleipner area gas development is located offshore Norway, in the Central North Sea, around 240 km west-southwest of Stavanger (Figure 1.1 and Figure 1.2). It is operated by Statoil, and produces natural gas and condensate from the Sleipner East and Sleipner West fields, as well as a number of satellite fields. The natural gas produced from Sleipner West has a CO_2 content between 4 and 9 %, which is much higher than the European market requirements of a CO_2 content lower than 2.5 %. The need for reducing this content, combined with a CO_2 tax implemented by the Norwegian government in 1991, and a commitment to sustainable energy production, are the motivation behind the initiation of CO_2 storage at Sleipner (Global CCS Institute, 2016b). Natural gas from the Sleipner West field is processed on the Sleipner T platform, before it is transported and injected into the Utsira Fm, located above the Sleipner East field (Figure 1.2).

The properties of the Utsira Fm (Upper Miocene to Lower Pliocene) are presented in e.g. Arts et al. (2008), Chadwick, Arts, & Eiken (2005) and NPD's CO_2 storage atlas (NPD, 2011). It constitutes a major saline aquifer with an extent around of 26 000 km^2, extending over 400 km from north to south, and 50 to 100 km from west to east. The location, horizontal extent, depth and thickness of the formation can be seen in Figure 1.3. The formation consists of stacked, overlapping sandstone fan lobes, separated by thin mudstones or shales. The Sleipner field is located near the southern limit of the formation, and in this area the Utsira reservoir is located at depths between 800 and 1100 m below sea level (Figure 1.2). The injection of CO_2 takes place at a depth of 1012 m, near the base of the formation, via a deviated well. The porosity and permeability of the aquifer are between 30 and 40 %, and 1 to 3 Darcy, respectively.

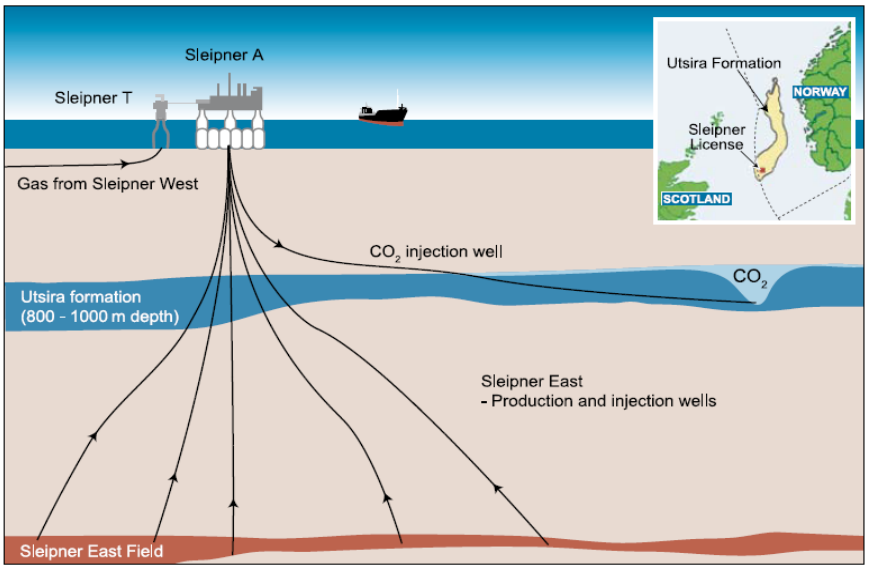

Figure 1.2: Simplified diagram of the Sleipner CO_2 storage project configuration (IPCC, 2005).

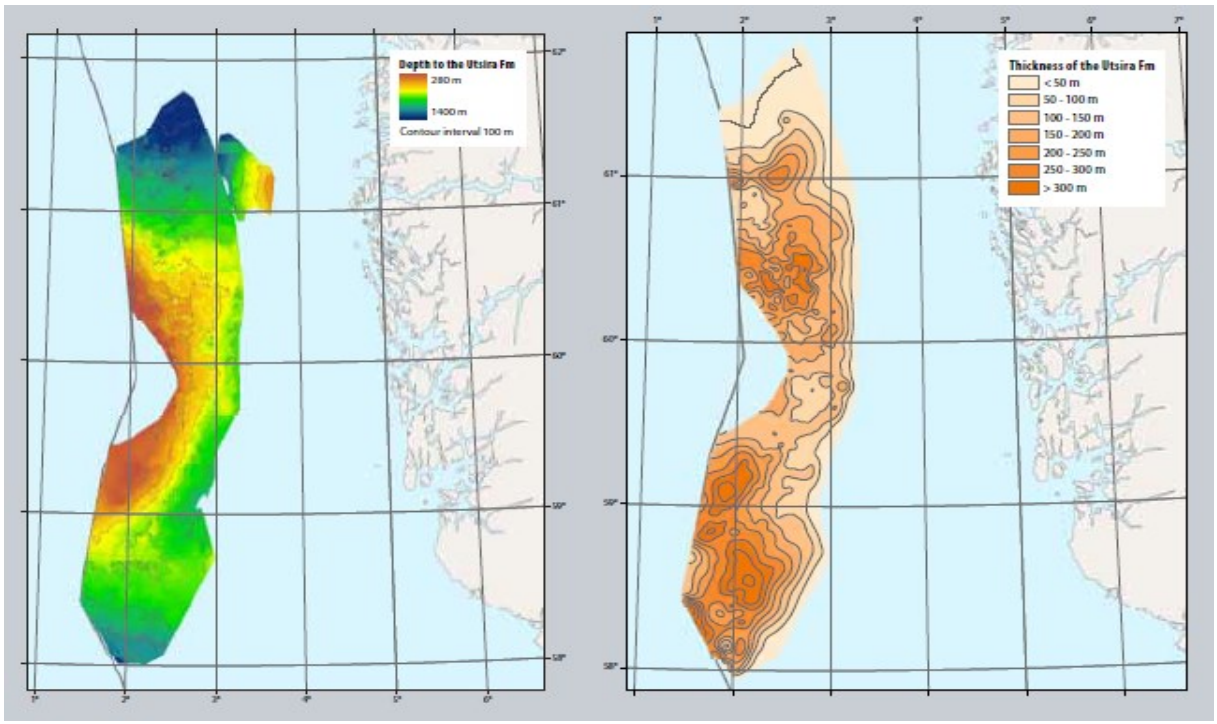

Figure 1.3: Depth surface (left) and thickness map (right) of the Utsira Fm (NPD, 2011).

The sandstone units in the Utsira Fm are estimated to be approximately 30 m thick, with beds of intra-reservoir mudstone and shale from less than one meter to over two meters thick. Arts et al. (2008) operates with eight mudstone units when modelling the reservoir in the Sleipner area, but points out that there are large uncertainties related to their distribution, geometry and continuity. The mudstone beds constitute important permeability barriers within the reservoir sand, and has a significant effect on the migration and entrapment of the injected CO_2.

Approximately 0.85 Mt of CO_2 has been injected into the Utsira reservoir every year, and by June 2016 the total amount was around 16.2 Mt (Global CCS Institute, 2016b). In the Sleipner area a 200 to 300 m thick shale package forms the main cap rock of the Utsira reservoir. The seal has been estimated to hold a supercritical CO_2 column of at least 100 m, maybe up to 400 m depending on the density, which is significantly in excess for the project estimations (Arts et al., 2008). No evidence of leakage has been observed, and the uppermost accumulation of CO_2 appears to be trapped beneath the reservoir cap rock, with no indications of migration into the overburden (Chadwick, Arts, & Eiken, 2005).

The CO_2 plume forms a compressible but buoyant supercritical fluid of low viscosity and high mobility, and is located between the injection point and the top of the reservoir. It is assumed to be present as one main component of high-saturation CO_2, and one lesser component of lower saturation (Chadwick, Arts, & Eiken, 2005).

1.5 Available data from Sleipner

During the Sleipner CO_2 project life, a number of geophysical surveys have been conducted to closely monitor the behavior of the injected CO_2. This includes a 4D seismic survey, four seabed micro gravimetric surveys, one CSEM survey and two seabed imaging surveys (Global CCS Institute, 2016b). Figure 1.4 shows the different surveys conducted over the area (until 2013), together with the total amount of injected CO_2 at the time of acquisition. This study focuses on data from the CSEM survey conducted in 2008, but data from the 4D seismic survey and well log data from wells in the area are also included. Integration of different geophysical data is of great value both for a priori information as input in the CSEM inversion process, and for evaluation of the resistivity images resulting from inversions of the CSEM data.

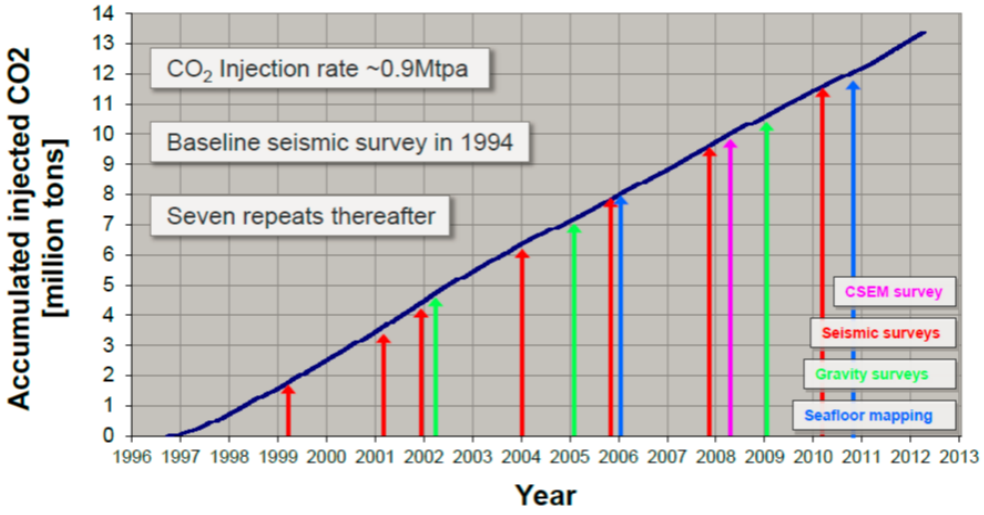

Figure 1.4: Time of acquisition of different geophysical surveys acquired in relation to the Sleipner CO_2 storage project. The year notations along the x-axis represent the middle of the year, and the total amount of injected CO_2 is plotted along the y-axis (Statoil, 2012).

1.5.1 2008 CSEM survey

In 2008 a CSEM dataset was acquired by EMGS over the CO_2 plume, and NGI received access to it through the research center FME SUCCESS, the EU project CO2ReMoVe, and Statoil. The data was acquired from south to north along a single towline of about 30 km (line 01Tx001a), above the accumulated CO_2 plume in the Sleipner field area. 27 receivers (Rx) were deployed on seabed, covering a stretch of about 9.5 km. A horizontal electric dipole (HED) source (Tx) was towed 20-30 m above seabed, and both inline electric and broadside magnetic fields were acquired for frequencies 0.5, 1, 1.5, 2, 2.5 and 7 Hz (Park et al., 2013; Park et al., 2014). Figure 1.5 shows the CSEM survey line and receiver positions, together with the location of the CO_2 plume and the deeper located Sleipner East field. The focus of this study is the magnitude and phase of the inline electric field.

A big challenge in interpreting the CSEM dataset, in terms of monitoring, is the fact that there is no baseline CSEM survey acquired prior to the CO_2 injection. At the time of the CSEM survey, in September 2008, the total amount of injected CO_2 was close to 10 Mtons (Figure 1.4), and a baseline survey would have given valuable insight to the effect of the CO_2 and the sensitivity of the CSEM method.

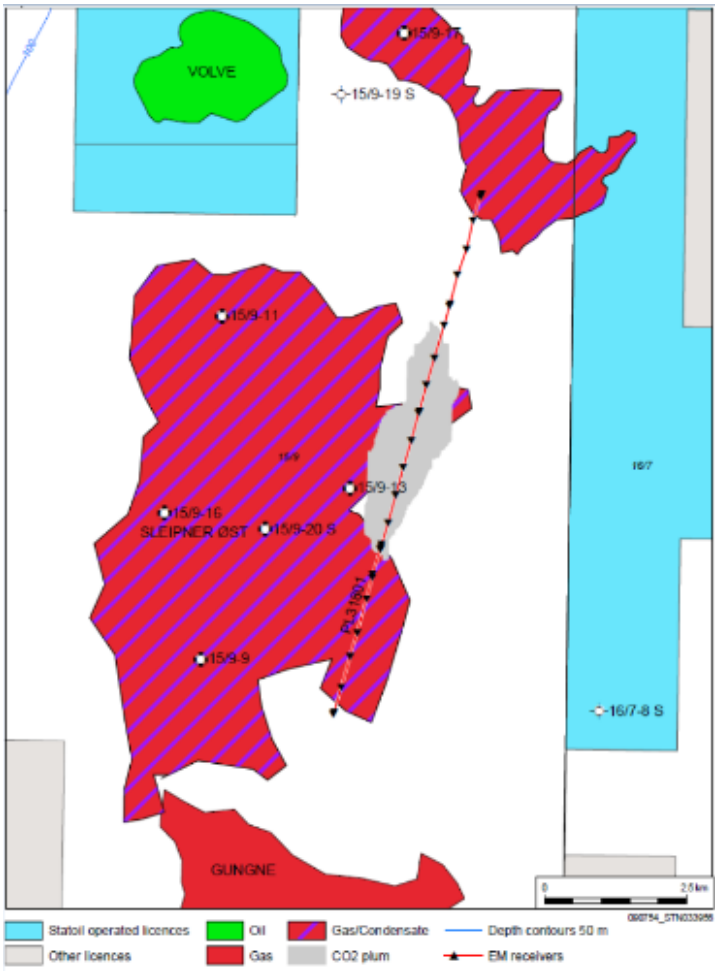

Figure 1.5: CSEM survey line and receiver positions over the Sleipner East field and the accumulated CO_2 plume. From Park et al. (2013), provided by Statoil.

1.5.2 4D seismic survey

A 4D seismic survey has been acquired to monitor the CO_2 injection at the Sleipner location. The 4D image of the growing CO_2 plume is formed by a baseline 3D seismic survey of the reservoir acquired in 1994, before the injection of CO_2 was initiated, and eight repeat time-lapse surveys (Global CCS Institute, 2016b). For this study the data from the baseline seismic survey from 1994, and the repeat survey from 2008 was available. On request from SUCCESS, Guillaume Sauvin at NGI has provided depth converted seismic data, which is used to determine the location and approximate extent of the CO_2 plume, and evaluate the results of the CSEM data inversions. Figure 1.6 shows depth converted seismic sections along the CSEM survey line, from the baseline seismic survey acquired in 1994, prior to any CO_2 injection (upper profile), and from the repeat survey acquired in 2008, when around 10 Mt of CO_2 had been injected (bottom profile). For this study, data from the 2008 repeat survey is available only near the region of the CO_2 plume.

The plume has an evident effect on the seismic data, and appears as a number of bright sub-horizontal reflections in the seismic from 2008. The plume is detectable at a depth approximately between 750 and 1000 m, and latitude coordinates 6470000 and 6473000. Arts et al. (2008) have interpreted the reflections to arise from up to nine discrete layers of CO_2, each up to a few meters thick, trapped beneath the intra-reservoir mudstones.

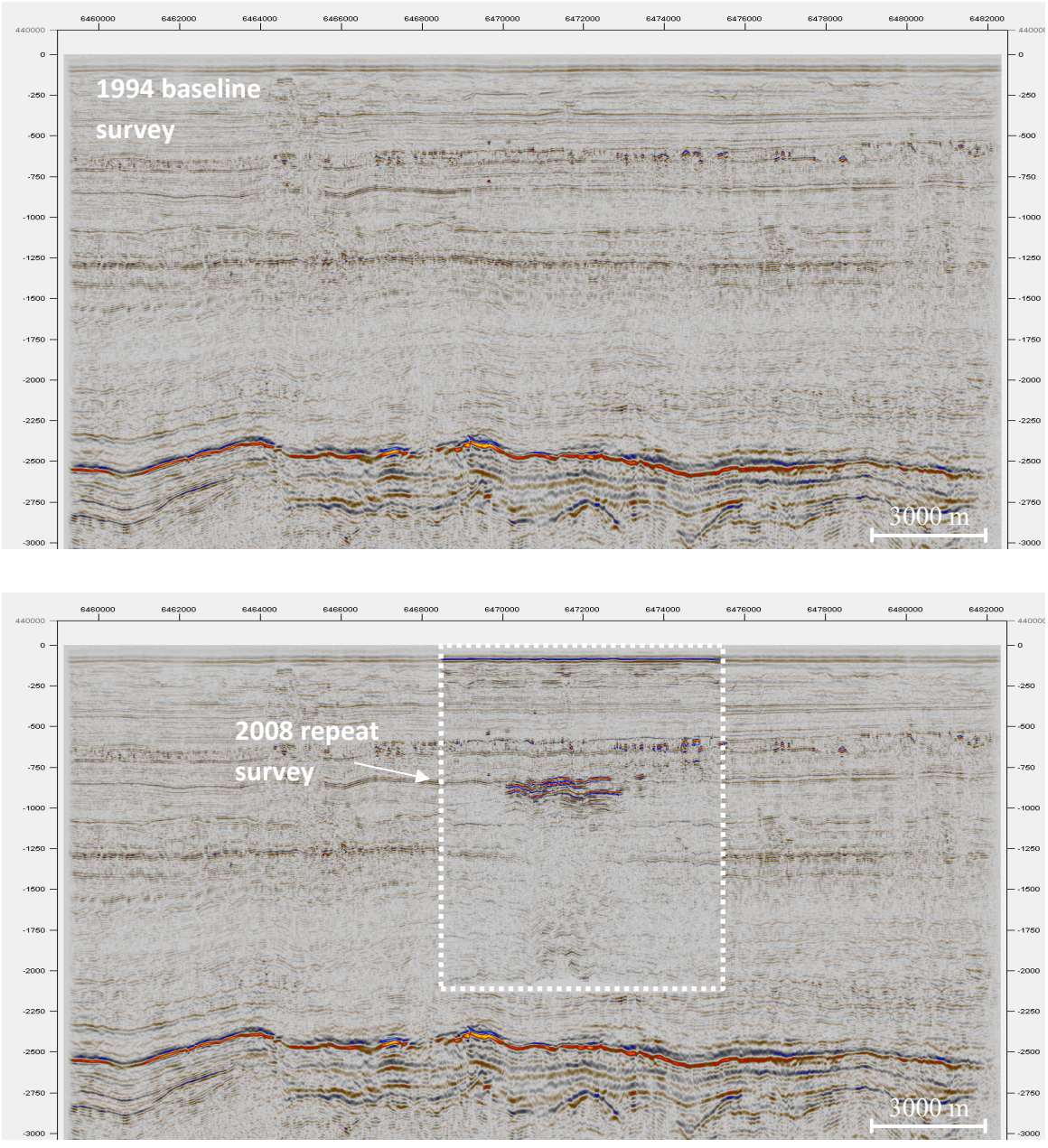

Figure 1.6: Depth converted seismic sections along the CSEM towline over the Sleipner area. The upper section is from the baseline survey acquired in 1994, prior to any CO_2 injection, while the seismic in the lower section (white rectangle) was acquired in 2008, the same year as the CSEM survey. The available data from the 2008 survey is covers a smaller area, and is superimposed on the baseline seismic.

1.5.3 Well log data

As can be seen from Figure 1.5, there are several wells in the vicinity of the CO_2 plume. Data from these wells are available from NPD (2017) and Statoil, and the resistivity logs from some of them have been studied for the purpose of establishing an a priori model for the CSEM data. The completion logs from the wells assumed to best represent the subsurface in the area of the CO_2 plume can be found in the Appendix. This includes data from well 15/9-13, which is located very close to the CO_2 plume, and well 15/9-16. Well 15/9-20 S is also located quite close to the plume, but well log data from this well was not available for the depth of interest, so data from well 15/9-16 have been employed instead.

1.6 The Skade CO_2 storage case study

The Lower Miocene Skade Fm is a saline aquifer in the North Sea, considered by the NPD as an option for large-scale storage of CO_2. The properties of the formation are presented in NPD's CO_2 storage atlas (NPD, 2011). It consists of marine sandstones, possibly turbidite deposits, covering a large area in the Viking Graben. The formation has a maximum thickness of over 300 m, and is located in the same area as the Utsira Fm, at larger depths. The Utsira and Skade Fm constitute the main parts of a sand system deposited by a deltaic system developed from the Shetland Platform towards the Norwegian parts of the North Sea. Figure 1.7 shows the location, horizontal extent, depth and thickness of the Skade Fm. The outer (deeper) part of the Skade Fm is sealed by Middle Miocene shale, and assumed to be suitable for CO_2 storage. NGI is currently involved in a case study of this potential injection site, where synthetic time-lapse seismic and CSEM data have been generated from CO_2 injection simulations.

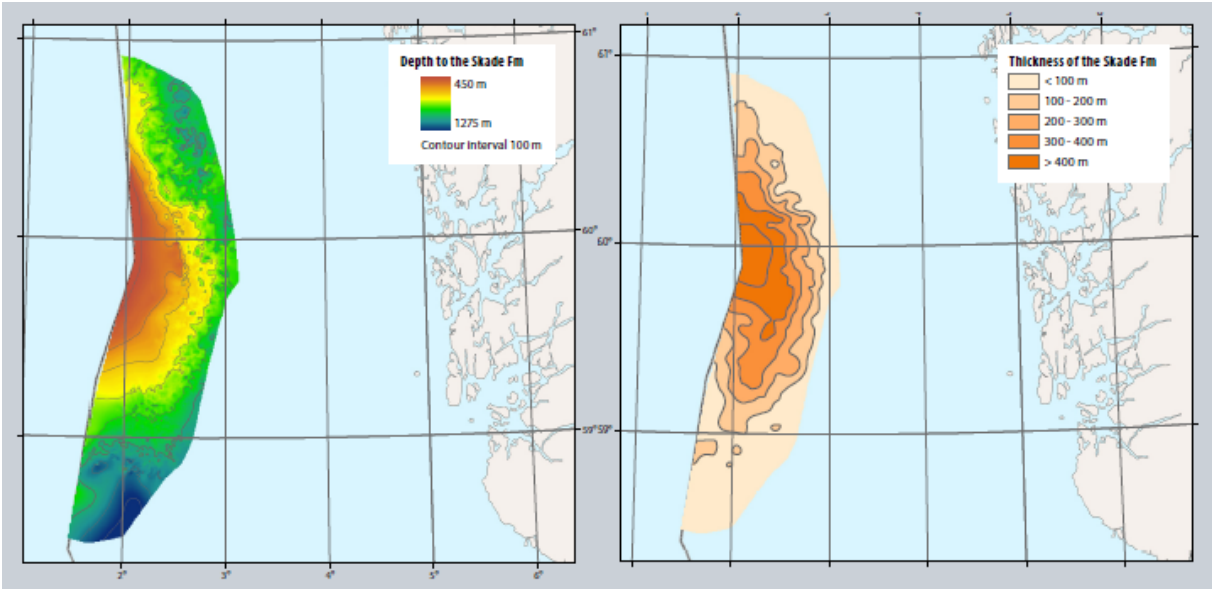

Figure 1.7: Depth surface (left) and thickness map (right) of the Skade Fm (NPD, 2011).

1.7 Available data from Skade

The Skade CO_2 storage case study comprises the simulation of CO_2 injection into the Skade Fm for 50 years, through three different wells. The initiation of the injection is set to year 2020, and simulated to end in 2070. Under the scope of work of FME SUCCESS, synthetic seismic and CSEM data have been produced, based on simulations of CO_2 injection done by Uni CIPR. Horizontal resistivity profiles covering the three injection sites in the Skade Fm, from both the 2020 model and the 2070 model, are presented in Figure 1.8. The resistivity profiles are provided by NGI, and the missing resistivity data at the base of the profiles are due to the assumption of a homogenous high resistivity domain in this area in the generation of the models. Synthetic CSEM data from a section covering the middle of the three injection wells, and the accumulating CO_2 plume, have been employed for this study. A CO_2 injection rate of 20 Mt per year was employed in the simulations, resulting in a total amount of 1 Gt CO_2 accumulated at this injection site in 2070. The CO_2 accumulation at this site is located at depths between 900 and 1100 m approximately, with a horizontal extent of around 12000 m (Figure 1.8).

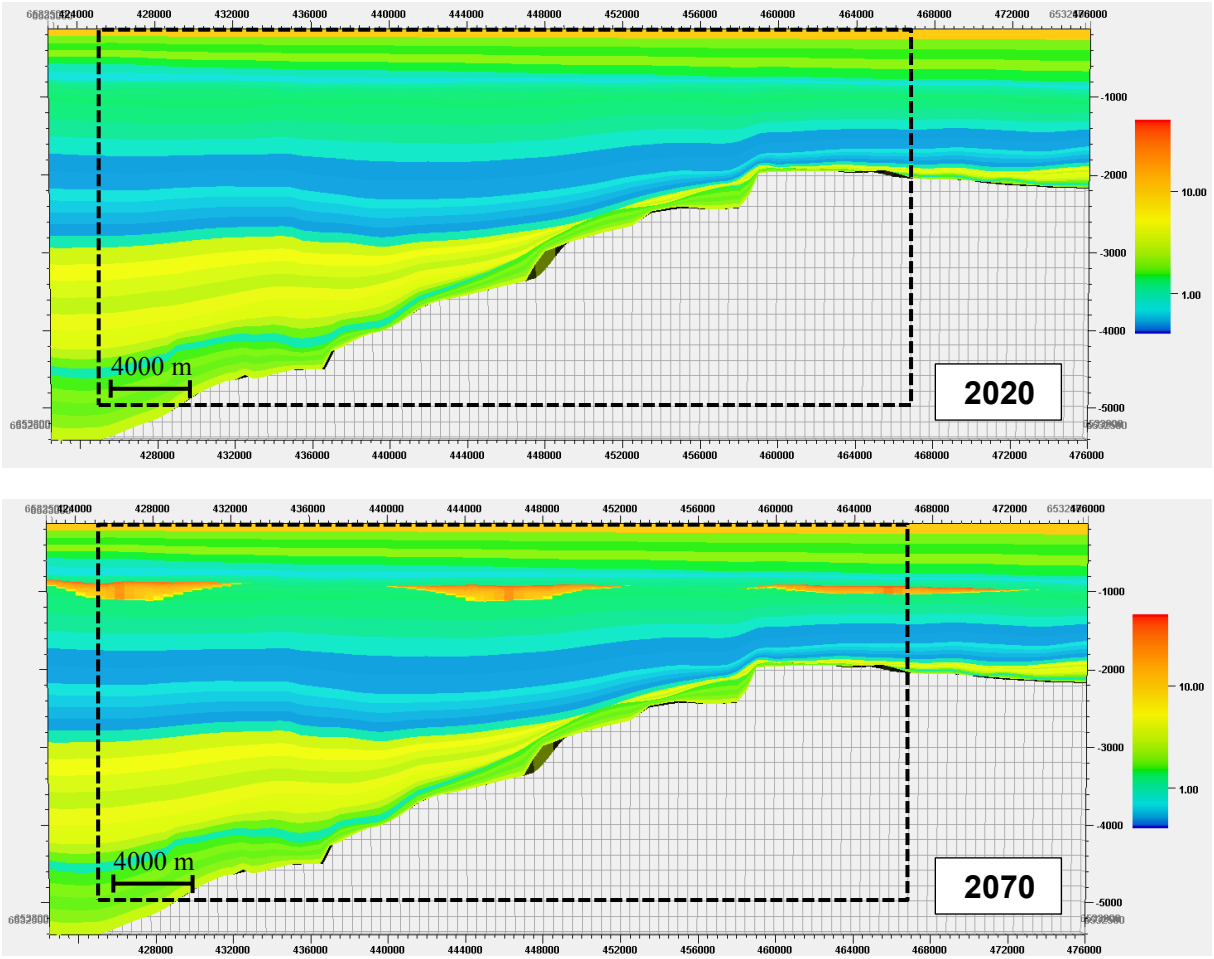

Figure 1.8: Horizontal resistivity profiles covering the three injection sites in the Skade Fm. The upper profile shows the resistivity from the 2020 model, while the lower profile shows the resistivity from the 2070 model. The resistivity models are provided by NGI, and obtained from data received by UniCIPR. The focus of this study is the area of the middle injection well, indicated by the black frame. Note the logarithmic color scale.

The section studied covers a stretch of 42 km along the CSEM towline (marked by the black frame in Figure 1.8). The water depth is 150 m, and the source positions are modeled 30 m above seabed. Receivers are placed every 1 km, between 11 and 31 km along the profile (21 in total). The data includes synthetic baseline data and time-lapse data for every fourth year until 2052, as well as data from the end of the injection period in 2070. This study focuses on the response before and after the simulated injection, e.g. the synthetic data from year 2020 and 2070. In the datasets the source sampling density is 100 m, and signals of nine different frequencies are available; 0.1, 0.25, 0.5, 0.75, 1, 2, 3, 4 and 5 Hz. Like in the Sleipner data study, the focus of the Skade synthetic data study is the magnitude and phase of the inline electric field.

1.8 Thesis structure

This chapter has given an introduction to the motivation and objective for the study performed in this MSc thesis, together with some background information and presentation of the available data. Chapter 2 gives a summary of electromagnetic (EM) methods, mostly focusing on the marine CSEM method, providing insight to the history and theory behind the method, as well its applications and limitations, and some general inversion theory for CSEM data.

Chapter 3 gives an introduction to the software employed in the CSEM data study, *ngi25em*, which is an in-house forward modeling and inversion software for EM data, developed by NGI. In chapter 4 the results from a forward modeling study is presented, with the purpose of demonstrating the sensitivity of the CSEM method, to different parameter variations.

Chapter 5 presents the inversion setups and results from an inversion study of the 2008 CSEM dataset from Sleipner, while the findings from these results are discussed in chapter 6. Based on this, an inversion strategy for the Sleipner CSEM dataset is presented. In chapter 7 the inversion setups and results from an inversion study of the synthetic CSEM data from Skade is presented, together with a discussion of the findings. The conclusions drawn from the inversion studies of the Sleipner and Skade datasets are presented in chapter 8.

2 Marine CSEM

The following chapter gives an introduction to the marine CSEM method. Section 2.1 gives a short introduction to marine EM methods in general, and some basic EM wave theory. Section 2.2 focuses on the CSEM method, and includes a short summary of the history (section 2.2.1), the basic principles and theory (section 2.2.2), the main applications (section 2.2.3) and the limitations (section 2.2.4) of the method. In section 2.3 the basic concepts of inversion are presented, with emphasis on inverting CSEM data.

2.1 Marine EM methods

The seismic method is the most commonly used method in hydrocarbon exploration, but it has limitations when it comes to discriminating between oil and water as a pore fluid, as well as high and low saturations of gas. This can be complemented by EM technology, which measures the resistivity of the subsurface by studying electromagnetic fields. As a marine EM method has been developed and commercialized (Eidesmo et al., 2002), it has become an attractive complementary method to seismic surveying, because it reduces the need for drilling expensive test wells to determine the reservoir fluid.

In literature on electrical properties (e.g. Lowrie, 2007), the electric resistivity (ρ) is defined as a physical property of the material of a conductor, which expresses the materials ability to oppose the flow of electric current. The resistivity is measured in Ohm-meters (Ωm), and the inverse of ρ is defined as the conductivity of the material (σ), measured in Siemens per meter (S/m). Ω is the unit of resistance, while S is the unit of conductance (the reciprocal of Ω). Figure 2.1 shows characteristic resistivity and conductivity values for different materials.

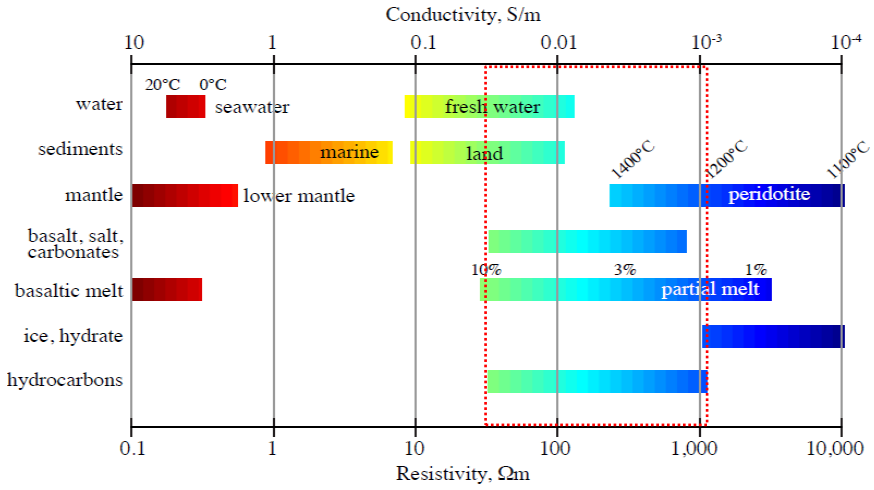

Figure 2.1: Conductivity (top scale) and resistivity (bottom scale) for different materials. The resistivity/conductivity range of hydrocarbons are marked in red. Mark the large difference in resistivity between seawater and hydrocarbons, as well as the resistivity overlap of hydrocarbons and basalt, salt and carbonates. Modified from Constable (2016).

There are a lot of literature on EM methods, where the concepts of marine CSEM, also known as seabed logging (SBL), and magnetotelluric (MT) methods are presented (e.g. Constable 2010; Johansen & Gabrielsen, 2015). These are the two basic types of marine EM methods, which both use seafloor recordings of electric and magnetic fields to examine the resistivity of the subsurface. In the CSEM method electromagnetic fields are induced by a controlled source, while the MT method measures electrical resistivity from variations in the Earth's natural electromagnetic field.

2.1.1 Basic EM wave theory

The propagation of EM waves can be derived by combining Faraday's law, Amperes law and Ohm's law (Gelius, 2016; Løseth & Ursin, 2007). Together with Gauss' law and Gauss' magnetism law these constitute Maxwell's equations, which describe the relation between electric and magnetic fields, and when including material properties, their behavior in different materials. Faraday's law says that time varying magnetic fields will generate electric fields, and is defined by:

$$\nabla \times \vec{E} = -\frac{\partial \vec{B}}{\partial t} = -\mu_0 \frac{\partial \vec{H}}{\partial t} \tag{2.1}$$

Here $\vec{E}$ represents the electric field vector, containing the three orthogonal components E_x, E_y and E_z, $\vec{B}$ is the magnetic flux density, and $\vec{H}$ represents the magnetic field vector, containing the orthogonal components H_x, H_y and H_z. The electric and magnetic field vectors are perpendicular to each other, and to the direction of propagation. μ_0 is the permeability of free space, also known as the magnetic constant, equal to $4\pi \times 10^{-7}$ (Amundsen et al., 2006; NIST, 2016). This version of Faraday's law applies for a source-free case, but for macroscopic media a magnetic source current vector, $\vec{M}$, can be introduced with a negative sign on the right handside of Faraday's law.

Amperes law says that magnetic fields are generated by time varying electric fields, defined by:

$$\nabla \times \vec{H} = \vec{J} + \frac{\partial \vec{D}}{\partial t} = \sigma \vec{E} + \varepsilon \frac{\partial \vec{E}}{\partial t} \tag{2.2}$$

where $\vec{D}$ represents the electric displacement field, $\vec{J}$ is the total current density and ε represents the electric permittivity of the material. Ohm's law describes the relation between the current density and the electric field by $\vec{J} = \sigma \vec{E}$, where σ is the electrical conductivity.

By combining Amperes law, differentiated with respect to time, with Faraday's law for a source-free case, the 3D electromagnetic wave-equation for the electric field can be derived (Gelius, 2016):

$$\nabla^2 \vec{E} - \mu_0 \sigma \frac{\partial \vec{E}}{\partial t} - \mu_0 \varepsilon \frac{\partial^2 \vec{E}}{\partial t^2} = 0 \tag{2.3}$$

A similar approach can be used for the magnetic field. A Fourier transform with respect to time transforms the wave-equation from time to frequency domain, which is commonly used in EM methods. This implies a transformation of $\partial/\partial t$ to $i\omega$ (Løseth & Ursin, 2007), and gives:

$$\nabla^2\vec{E} = (i\sigma\omega - \varepsilon\omega^2)\mu_0\vec{E} \equiv k^2\vec{E} \tag{2.4}$$

For high frequencies, σ will be much smaller than $\varepsilon\omega$, and the second derivative term will dominate. Neglecting the first derivative term, the wave equation will be analog to the seismic wave equation, and the waves will be propagating and very little attenuated. For low frequencies σ will be much larger than $\varepsilon\omega$, the first derivative term will dominate, and the second derivative term can be neglected. This gives $k^2 = i\sigma\mu_0\omega$, and the waves will be diffusive and reflect conductivity (and resistivity) differences. Such diffusive waves are employed in EM methods for mapping the resistivity of the subsurface.

The monochromatic (i.e. unique frequency and wavelength) 2D plane wave solution of the diffusion equation;

$$\vec{E} = \vec{E}_0 e^{-i(\omega t - kx)} \tag{2.5}$$

gives the following expression for the wavenumber k:

$$k = \sqrt{i\omega\mu_0\sigma} = (1+i)\sqrt{\frac{\omega\mu_0\sigma}{2}} = (1+i)\alpha \tag{2.6}$$

where de Moivre's theorem is applied for $\sqrt{i} = (1+i)/\sqrt{2}$. The low frequency EM signals decay exponentially with distance, and the diffusive waves are characterized by the skin depth. This is defined as the distance, d, where the EM signal has been attenuated by a factor 1/e. This can be expressed by the following relation, when inserting $2\pi f$ for ω (Gelius, 2016):

$$\frac{E}{E_0} = e^{-\alpha d} \equiv e^{-1} \quad \Rightarrow \quad d = \frac{1}{\alpha} = \sqrt{\frac{1}{\pi\mu_0\sigma f}} \tag{2.7}$$

By inserting for μ_0 this can be approximated to an expression only depending on frequency and conductivity (or resistivity):

$$d \cong 503.3\sqrt{\frac{1}{\sigma f}} = 503.3\sqrt{\frac{\rho}{f}} \tag{2.8}$$

The skin depth increases with increased resistivity and/or decreased frequency, and the expression shows how EM waves propagating in resistive material will be less attenuated than waves propagating in more conductive materials. This is the fundamental theory behind EM methods.

The fact that MT signals are very much attenuated on their way through the conductive seawater, and that CSEM signals are more sensitive to thin layers of hydrocarbons, makes the CSEM method more suitable for the marine environment and hydrocarbon detection (Constable, 2010; Gelius, 2016).

2.2 The CSEM method

2.2.1 Brief history

The marine CSEM method was originally developed for academic studies of oceanic lithosphere and mantle. In the 1960s several publications proposed the use of marine CSEM to measure seafloor resistivity, and suitable equipment was developed during the same period (Constable & Srnka, 2007). The method that is used today for hydrocarbon exploration was developed by Charles Cox of Scripps Institution of Oceanography (Cox, 1981), also this with the focus of mapping electrical properties of oceanic lithosphere. Academic development of the method have been carried out since, but the method has only been of significant use for the purpose of hydrocarbon exploration since 2000, when the first survey of an oil field was carried out (Ellingsrud et al., 2002). More details around the history and development of the method can be found in e.g. Constable (2010) and Constable & Srnka (2007).

The hydrocarbon industry started to show interest for the method in the 1990's, when production technologies developed so that exploration could move into deeper waters. Prior to this, exploration had been confined to shallow environments, and majority of the attention had been directed towards the increasingly good results from 3D seismic methods (Constable, 2010). Modeling studies and field trials showed that CSEM data could be used to evaluate reservoir resistivity for targets at several thousand meters depth, and it became a promising tool for solving challenges associated with exploration in deep-water environments. By using CSEM to reduce uncertainties related to seismic hydrocarbon indicators, the need for expensive deep-water exploration wells decreased. The companies in the exploration industry became aware of the possibility of reducing both drilling expenses and risk by collecting additional information from CSEM data.

2.2.2 Basic CSEM theory

The CSEM method have many similarities with the theory and acquisition of the seismic reflection method. The main differences are the use of electromagnetic energy instead of acoustic energy, which measures the differences in the resistivity instead of differences in density and seismic velocity, and that an array of receivers is placed at seabed instead of using mobile streamers. However, in the recent years PGS has developed an acquisition design with mobile receivers. Also, the energy propagation for low frequent electromagnetic energy is by diffusion, not wave propagation as for seismic energy. The CSEM

method measures the resistivity of the subsurface, which is highly increased if the pore fluid in geological formations changes from mainly water to mainly hydrocarbons (mark the large difference in resistivity between seawater and hydrocarbons in Figure 2.1).

Since the hydrocarbon industry became aware of the advantages of the CSEM method, many articles on the topic have been published. The concept of the CSEM method is accounted for in detail in articles by e.g. Constable (2010) and Constable and Srnka (2007), and can be summarized as follows. A powerful horizontal electric dipole (HED) source, usually 100 to 300 m long, is towed close to seabed, normally between 25 and 100 m above, to maximize the energy coupling with seafloor rocks, and minimize coupling with the air. The source produces an electromagnetic signal of low frequency (0-10 Hz) that propagates through the water and into the subsurface. Normally the acquisition is done in the frequency domain, where the source transmits a continuous square signal, corresponding to a base frequency and higher harmonics. A series of receivers are placed at seabed, and record the horizontal and vertical components of the electric and magnetic fields. The signal is measured for source-receiver ranges up to several tens of kilometers, and the recorded signal depends on the signal transmitted from the source, the resistivity of the subsurface, and the source-receiver distance. Figure 2.2 illustrates the configuration of a marine CSEM survey.

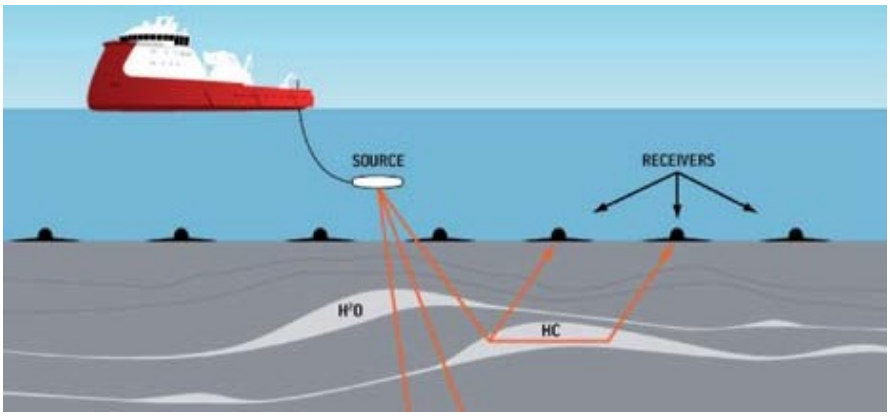

Figure 2.2: Configuration of a marine CSEM survey, with a HED source towed close to seabed, emitting an electromagnetic signal recorded by receivers at seabed. From Carstens (2009).

The total EM response recorded at the receivers is a combination of several energy pathways. This includes signal transmission directly through the seawater, reflection and refraction from the air-water interface, reflection and refraction from seabed, and potentially reflection and refraction from high resistivity subsurface layers (Johansen & Gabrielsen, 2015).

Figure 2.3 illustrates different mechanisms that produce changes in amplitude and phase of the electric signal as a function of source-receiver offset (Constable, 2010). Geometrical spreading causes the amplitude to decay by a factor of $1/r^3$, where r is the source-receiver offset. Galvanic effects are caused

by a jump in the electric field when the current crosses a conductive boundary. According to Ohm's law the current density $(\vec{J})$ is the product of the material conductivity (σ) and the electric field $(\vec{E})$, so when the conductivity changes, the electric field must change in order to keep the current density constant. These two mechanisms produce amplitude variations, but no associated change in phase. Inductive attenuation is the decay of electromagnetic fields within a medium, which is expressed by the skin depth (section 2.1.1). Inductive attenuation also causes changes in the phase of the signal. When the signals has travelled a distance of one skin depth, the phase is shifted one radian.

For the low frequencies used in CSEM methods the skin depth is normally around a couple of hundred meters for seawater, while it can be more than tens of kilometers in igneous seafloor rocks (Constable, 2010). Typical skin depths for a 0.25 Hz signal can be computed from equation 2.8, with typical resistivities from Johansen & Gabrielsen (2015), and are around 551 m in seawater (typically 0.3 Ωm), 1424 m in sediments of 2 Ωm, and 10^8 m in air (typically 10^{10} Ωm). Since the EM signals are rapidly attenuated in seawater and seafloor sediments saturated with saline water, signals propagating through these media will only dominate at near source-receiver offsets.

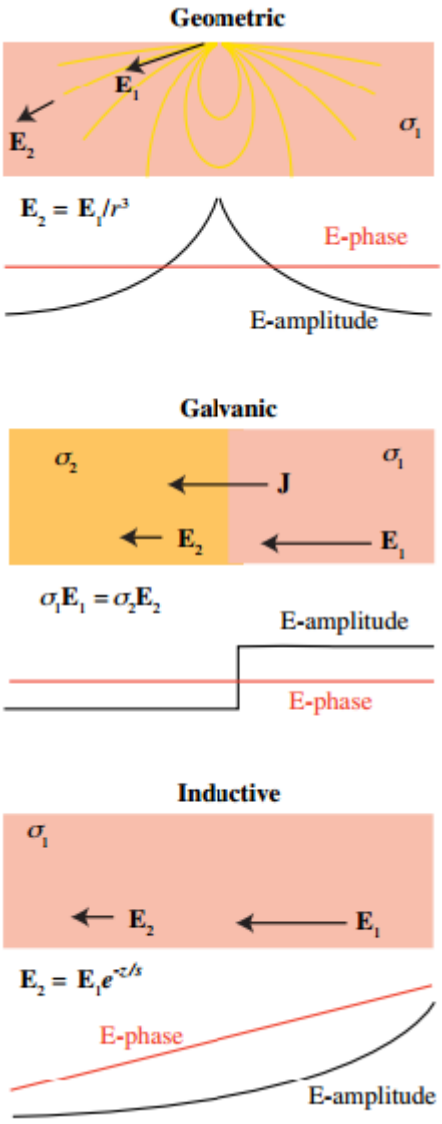

Figure 2.3: Three different mechanisms producing changes in amplitude and phase of the electric signal as a function of source-receiver offset. From top: geometrical spreading; galvanic effects; and inductive attenuation (Constable, 2010).

The measured EM signal at the receivers can be divided into three main contributions; the direct mode, the guided mode and the airwave. The direct mode is the part of the EM signal transmitted directly through seawater from source to receiver. The guided mode arises from relatively thin layers of high resistivity where the energy is guided along the layer and attenuated less, constantly leaking energy back to the receivers at seabed, analogous to refraction of seismic waves. In deep water (water depths larger than 300 m) the guided mode can be detected at an offset typically about 2-3 times the target depth (Gelius, 2016), when the direct mode has been significantly attenuated by diffusion through the water, so that the guided mode starts to dominate. With increasing offsets, depending on the water depth and subsurface resistivity, the contribution from the airwave starts to dominate. The airwave is the portion of the EM energy that is refracted along the air-water interface. In shallow waters (less than 300 m), the onset of the airwave

domination of the response will be at much smaller offsets, and the airwave signal can partially mask, or even completely dominate, the response from the guided mode (Gelius, 2016).

CSEM data can be collected in an inline or broadside configuration (Gelius, 2016). For inline configurations the receiver line is parallel with the source polarization while for broadside configurations the receiver line is orthogonal to the source polarization (Figure 2.4). For 3D surveys most of the data measured at the receivers will have an azimuth component, since the receivers measure both inline and broadside data, referred to as azimuthal data (Johansen & Gabrielsen, 2015).

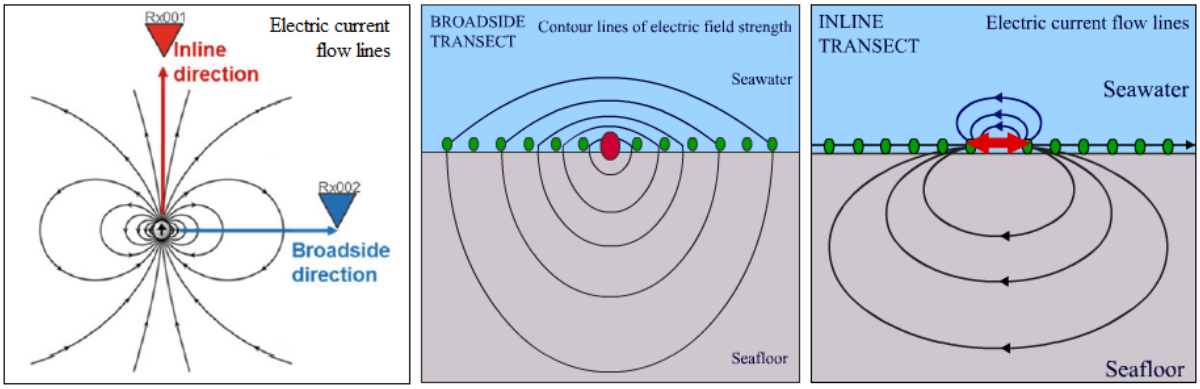

Figure 2.4: From left: illustrations of inline and broadside survey configuration; transect of a broadside survey configuration; transect of an inline survey configuration. Modified from Gelius (2016) and Johansen & Gabrielsen (2015).

A 1D layered model can be a good approximation to the subsurface of the Earth. For such a model, a broadside configuration implies that the electric current measured at the receivers have not crossed any conductivity boundaries, as the flow direction is normal to the plane in the middle figure in Figure 2.4. The strength of the electric field is thus modified by geometric and inductive effects, but no galvanic effect occurs. Three components of the electromagnetic field will be measured at the receivers; the inline horizontal and vertical components of the magnetic field, and the broadside horizontal component of the electric field (H_x, H_z and E_y if the figure plane is defined as the x-z plane). The other electromagnetic field components will be zero.

The figure to the right in Figure 2.4 shows the electric current flow lines for an inline transect. The vertical component causes the electric current to cross conductivity boundaries, and the electric field will additionally be modified by galvanic effects, corresponding to a guided mode existing in a layer of high resistivity (Gelius, 2016). The inline horizontal and vertical component of the electric field, and the broadside horizontal component of the magnetic field will be measured at the receivers (E_x, E_z and H_y if the figure plane is defined as the x-z plane), while the rest of the electromagnetic field components will be zero. For such layered models, the inline configuration carries the most relevant information for detecting high resistivity layers in the subsurface, due to the galvanic effect that generates the higher

CSEM response from high resistivity layers. Such an inline configuration was employed in the acquisition of the 2008 CSEM data from Sleipner, and in the modeling of the synthetic Skade data.

Normally the properties of the subsurface are directionally dependent, resulting in different horizontal (ρ_h) and vertical (ρ_v) resistivity. Constable (2010) demonstrates how the inline electric field is more sensitive to the vertical resistivity, while the broadside field is more sensitive to horizontal resistivity.

Different data processing steps are employed to convert the recorded data into amplitude and phase of the transmitted signal, as a function of source-receiver offset and frequency. This is referred to as amplitude versus offset (AVO) and phase versus offset (PVO) (Constable & Srnka, 2007; Johansen & Gabrielsen, 2015), which are used for further analysis and as input to CSEM data inversion algorithms. A resistive target will yield a higher amplitude and less steep phase curve compared with the response of a model without the target structure. To highlight larger amplitudes associated with such structures, the amplitude can be normalized (nAVO) by baseline data, or by the response recorded by an instrument assumed to be off-target by

$$nAVO = \frac{A_E}{A_{E_b}} \tag{2.9}$$

where A_E is the measured magnitude of the electric field over the target structure, and A_{Eb} is the background response without the target structure. The same can be done for the phase (φ) of the electric field (nPVO) by subtracting the phase of the background response (φ_{Eb}) from the phase of the measured response over the target structure (φ_E);

$$nPVO = \varphi_E - \varphi_{E_b} \tag{2.10}$$

Marine CSEM data is generally of high quality, due to a low noise level at seabed, high sensitivity and low system noise of the recorders, and large source strength of the transmitted signal (Constable & Srnka, 2007). The receivers can measure very weak electric fields, typically as low as 10^{-15} V/m per unit dipole moment of the transmitter, which is defined as the noise level (Gelius, 2016). The ability to sample different frequencies makes it possible to control the depth of sensitivity, but it is important to keep in mind that by increasing the frequency, the attenuation of the signal will also increase. For lower frequencies the skin depth will increase, making it possible to detect deeper structures, but at the same time the resolution will decrease. In general, the resolution of the CSEM method is inferior of the seismic method (Constable 2010), but the interpretation of the data can be significantly improved by integrating the data with other geoscientific information, such as seismic data and/or well log data.

2.2.3 Applications

The main application of marine CSEM today is in hydrocarbon exploration, as a complementary method to seismic. The two methods have different sensitivities to hydrocarbons, and can thus provide different information about the subsurface. Seismic provides high-resolution structural images of the subsurface, and can also give quantitative information from e.g. AVO analysis and seismic attribute extraction. The method is most sensitive to low saturations of gas, as this has the largest effect on the seismic P-wave velocity (V_p). Also, the method often has difficulties discriminating between oil and water as a pore fluid, since the impedance contrast between these may be low. The CSEM method is, on the other hand, more sensitive to the fluid content. Since hydrocarbons generally have a much higher resistivity than brine (Figure 2.1), this method easily discriminates between oil and brine as pore fluid. It is also much more sensitive to higher gas saturations, as the effect in resistivity increase with increasing saturation of hydrocarbons. The CSEM method can thus provide useful information about saturation and pore fluid type that cannot be detected by seismic.

Figure 2.5 illustrates the sensitivity of the two methods to different gas saturations by plotting V_p and resistivity in a sandstone of 50 % porosity, as a function of gas saturation. The largest effect in V_p occurs for the first few percent of gas saturation, while for saturations above 0.25, V_p is almost unaffected. The resistivity has larger variations for all saturations, with the largest effect for saturations above 0.7. Drilling based on seismic hydrocarbon indicators caused by low saturation of gas can thus be avoided by acquiring CSEM data.

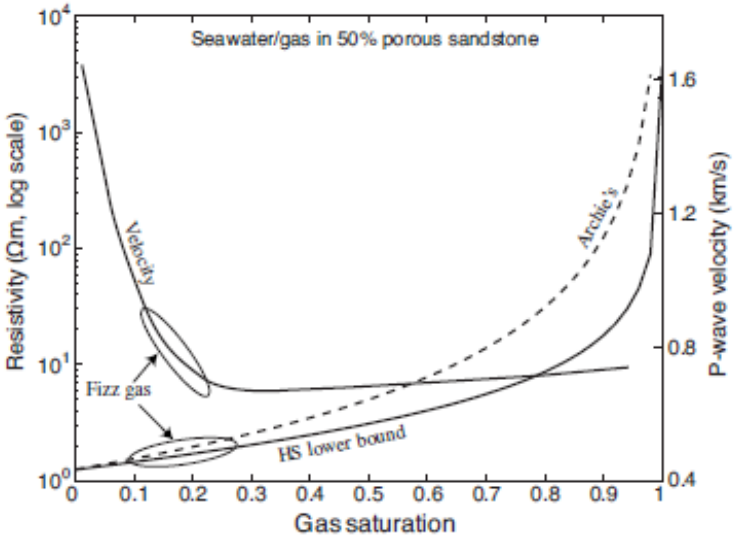

Figure 2.5: Seismic P-wave velocity and electric resistivity of a sandstone with a porosity of 50 %, as a function of gas saturation. The largest effect on the P-wave velocity occurs for low fractions of gas saturation, while the largest effect in resistivity are for saturations above 0.7 (Constable, 2010).

Combined with seismic and well-log data, the CSEM method can help improve the image and interpretation of the subsurface, and give valuable information about saturations and fluid content.

Consequently, both drilling costs and risk can be reduced, as the need for drilling expensive test wells, and the risk of drilling dry wells, decrease.

The CSEM method has proven successful in several cases where it has been applied for exploration purposes, for example in the Barents Sea for the Wisting and Bjaaland prospects (Carstens, 2015). In both prospects the seismic showed indications of hydrocarbons, while a CSEM anomaly only was observed over the structure in the Wisting prospect. Drilling confirmed the CSEM indications; the Wisting prospect was an oil discovery, while the Bjaaland well was dry.

The CSEM method also has potential when it comes to hydrocarbon field development and production, especially when it comes to reservoir monitoring. This is closely related to CO_2 injection monitoring, where the same principles are applied. The increasing interest in subsurface CO_2 storage may also give an increased interest in applying CSEM for this purpose. The saturation information extracted from CSEM data can be of great value when evaluating the behavior of the injected CO_2, and CSEM data can also be useful to improve discrimination between time-lapse changes in saturation and pressure (Tveit, Mannseth, & Jakobsen, 2016). For monitoring purposes, baseline CSEM surveys should be acquired prior to injection/production, as this will make the effect of the changes easier to determine, and the normalization and interpretation of the data easier.

2.2.4 Limitations

As mentioned above, the resolution of CSEM data is much lower than for seismic data. The demand for low frequencies to generate diffusive waves that reflects the resistivity differences also causes limitations when it comes to resolution. However, the resolution of the method is much better than potential-field methods such as gravity and magnetic methods, which previously have been the other geophysical methods used in the exploration industry, in addition to seismic data (Constable 2010). Constable (2010) estimates both lateral and vertical resolution of inductive EM methods to around 5 % of the depth of burial of the target, but also points out that the resolution can be improved significantly by including additional information into the interpretation.

The method also have limitations when it comes to penetration depth, as attenuation of the diffusive waves will occur when the waves diffuse in the conductive water and the subsurface of varying resistivity. The penetration depth will depend on the skin depth, which again depends on resistivity and frequency.

It is also important to be aware of the fact that different subsurface structures can generate the same CSEM response. This is demonstrated by Constable (2010), which shows how almost identical responses can be generated by so-called T-equivalent models. T-equivalent models are characterized by

identical products of the layer thickness and resistivity. He also demonstrates how this can be solved by looking at two well-spaced frequencies. For one frequency the different models may give the same CSEM response, but for another frequency the responses may be distinguishable.

Another known limitation of the method is that targets appear shallower than in reality. This may be rooted in the low resolution of the method, and the target location may be improved by employing e.g. constrained inversions, or including higher frequencies. Integration with other geophysical datasets is essential in exploration, as the resistivity alone is not a certain indicator of hydrocarbons. The resistivity of other media, such as basalt, salt and carbonates, overlaps the resistivity range of hydrocarbons (Figure 2.1). This is important to keep in mind when analyzing marine CSEM data.

2.3 Basic CSEM inversion theory

The CSEM method measures the electric and magnetic field recorded at seabed, with the goal of determining the resistivity distribution in the subsurface. This parameter cannot be directly estimated from the data, and an inversion procedure is necessary to transform the data into interpretable resistivity values. The concept of inverting electromagnetic data is explained by Johansen & Gabrielsen (2015). Inversion represents a more advanced approach to processing compared to forward modeling. In forward modeling, subsurface models are used to simulate geophysical experiments and produce synthetic data that would be generated by such models. The objective of solving an inverse problem is to find the model m that best explains the measured data d:

$$d = G(m) \tag{2.11}$$

where the operator G describes the relation between the model and the measured data. The inversion yields possible subsurface models that could account for the values of the measured data, but the solutions are normally non-unique, meaning that several resistivity models could generate the same data measurements.

An outline of the inversion concept is given by the Department of Earth, Ocean and Atmospheric Sciences at the University of British Columbia (2007), and can be summarized as follows. For CSEM data, the inversion process uses the acquired CSEM data and a priori information as input, and produce a set of resistivity models. There are many different inversion methods available (e.g. Auken & Christiansen, 2004; de Groot-Hedlin & Constable, 2004; Constable, Parker, & Constable, 1987), and the choice of method will impact the resulting models. An initial resistivity model m_0 is determined, based on a prior information, such as seismic data, well log data, core samples etc. The starting model, as well as the measured data, act as a constraint, and limits the possibilities of solutions from the inversion. The data that would be produced by the initial model is determined from forward modeling,

employing the electromagnetic wave equation, and source-receiver geometry identical to the real survey configuration. The generated synthetic data are then compared to the measured data, and the difference shows how well the model explains the measurements. A desired value is assigned to this misfit, and the process is repeated with a new computed model as a starting point, until the difference between the synthetic and measured data satisfies the desired misfit criterion. Normally the misfit is minimized using least square methods.

The resistivity model consists of a grid of cells, assigned different resistivity values. The parametrization of the model includes choosing the size and shape of the cells, and how the resistivity values are distributed. One way of parameterizing an area is by a gradual transition, where the resistivity of the cells are given by a varying function. Another way is to apply a layered transition, where the different layers in the model are given different constant resistivity values.

Finding the solution that minimizes the misfit between the estimated and the real data will normally not constrain the solution to one single model. Therefore regularization is introduced, where additional information is added to solve the inversion problem. This can for example be done in the form of seeking a smooth horizontally layered resistivity model, or by minimizing the change in the model from one iteration to the next. The data misfit and the regularization cost constitutes the total cost function, and the inversion iterates until the total misfit is within a certain value. The schematics of the inversion process is presented in Figure 2.6.

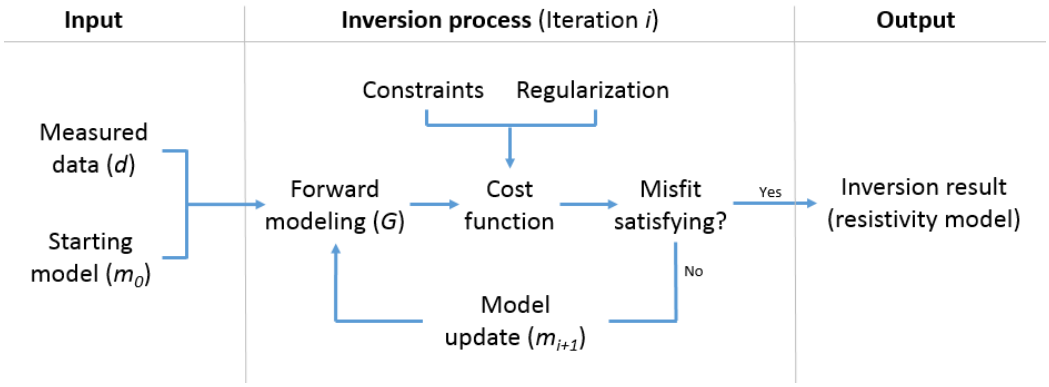

Figure 2.6: A schematic representation of the inversion process. Modified from Johansen & Gabrielsen (2015).

The inversion result depends on the starting model, the regularization, and the a priori information used to constrain the results. Adding constraints limits the solutions, by for example restricting a resistivity interval for different layers based on well log data. In the inversion process, one can add several restrictions to the solution, expressed mathematically by what factors desired to minimize. However, increasing amount of restrictions leads to more complicated equations and solutions, and it is important to keep in mind that restrictions on the model update also can cause incorrect results. The solution is

directly affected by the constraints, and will be incorrect if the constraints are based on incorrect assumptions. Such constraints should therefore only be employed in case of reliable a prior knowledge, and inversions without the restrictions can be performed for comparison.

3 Software used for forward modeling and inversion of CSEM data

This chapter gives an introduction to the software employed to perform data editing, forward modeling and inversion of CSEM data in this study; *ngi25em 5.0 RC-023*. The software is developed by NGI to perform 2.5D forward modeling and inversions of EM data, and comprises graphical user interfaces (GUI) for data editing (*ngi25em_data_browser*), forward modelling (*ngi25em_model_gui*), and inversion (*ngi25em_inversion_gui*). The model handles 3D navigation data, but resistivity models are presented in 2D. The subsurface model is generated along a specified towline (x), for the desired depth (z). The software can handle inversions for multiple 2D lines, but only single-line surveys were available for this study.

3.1 Forward modeling

The forward modeling in the software is based on a finite element formulation of the solution of Maxwell's equations in the frequency domain (NGI, 2010; Vöge et al., 2014). The model is considered to be homogeneous in the y-direction, so the resulting resistivity model is a 2D model in the x-z plane. However, the modeled electromagnetic wave field is in 3D, hence the 2.5D notation in the name of the software. A Fourier transform is applied to the solution of Maxwell's equations, with respect to the y-direction, and the corresponding wavenumber k_y is introduced. The derivation of the governing equation for 2.5D EM wave motion in the k_y wavenumber domain is similar to that of Mitsuhata (2000), except for the material properties and the use of the wave component from left to right, instead of right to left, causing some deviation in terms of signs. After rewriting the EM wave equation in the k_y wavenumber domain, and solving for E_x, E_z, H_x and H_z, the governing equations for the 2.5D EM wave motion are expressed by:

$$\begin{aligned}&\frac{\partial}{\partial x}\left[\frac{i\omega\varepsilon_x}{k_y^2-\omega^2\mu_z\varepsilon_x}\frac{\partial E_y}{\partial x}\right]+\frac{\partial}{\partial z}\left[\frac{i\omega\varepsilon_z}{k_y^2-\omega^2\mu_x\varepsilon_z}\frac{\partial E_y}{\partial z}\right]-i\omega\varepsilon_y E_y\\&-\frac{\partial}{\partial x}\left[\frac{ik_y}{k_y^2-\omega^2\mu_z\varepsilon_x}\frac{\partial H_y}{\partial z}\right]+\frac{\partial}{\partial z}\left[\frac{ik_y}{k_y^2-\omega^2\mu_x\varepsilon_z}\frac{\partial H_y}{\partial x}\right]\\&=J_{sy}+\frac{\partial}{\partial x}\left[\frac{ik_y}{k_y^2-\omega^2\mu_z\varepsilon_x}J_{sx}\right]+\frac{\partial}{\partial z}\left[\frac{ik_y}{k_y^2-\omega^2\mu_x\varepsilon_z}J_{sz}\right]\\&-\frac{\partial}{\partial z}\left[\frac{\omega^2\varepsilon_z\mu_x}{k_y^2-\omega^2\mu_x\varepsilon_z}M_{sx}\right]+\frac{\partial}{\partial x}\left[\frac{\omega^2\varepsilon_x\mu_z}{k_y^2-\omega^2\mu_z\varepsilon_x}M_{sz}\right]\end{aligned}\tag{3.1}$$

$$\frac{\partial}{\partial x}\left[\frac{i\omega\mu_x}{k_y^2-\omega^2\mu_x\varepsilon_z}\frac{\partial H_y}{\partial x}\right]+\frac{\partial}{\partial z}\left[\frac{i\omega\mu_z}{k_y^2-\omega^2\mu_z\varepsilon_x}\frac{\partial H_y}{\partial z}\right]-i\omega\mu_y H_y$$
$$+\frac{\partial}{\partial x}\left[\frac{ik_y}{k_y^2-\omega^2\mu_x\varepsilon_z}\frac{\partial E_y}{\partial z}\right]-\frac{\partial}{\partial z}\left[\frac{ik_y}{k_y^2-\omega^2\mu_z\varepsilon_x}\frac{\partial E_y}{\partial x}\right]$$

$$= i\omega\mu_y M_{sy}-\frac{\partial}{\partial x}\left[\frac{k_y\omega\mu_x}{k_y^2-\omega^2\mu_x\varepsilon_z}M_{sx}\right]-\frac{\partial}{\partial z}\left[\frac{k_y\omega\mu_z}{k_y^2-\omega^2\mu_z\varepsilon_x}M_{sz}\right] \quad (3.2)$$
$$-\frac{\partial}{\partial z}\left[\frac{i\omega\mu_z}{k_y^2-\omega^2\mu_z\varepsilon_x}J_{sx}\right]+\frac{\partial}{\partial x}\left[\frac{i\omega\mu_x}{k_y^2-\omega^2\mu_x\varepsilon_z}J_{sz}\right]$$

In these two equations, $\overrightarrow{J_s}$ and $\overrightarrow{M_s}$ represent the electric and magnetic source current vectors, respectively. Since the x- and z-components of the electric and magnetic fields have been expressed in terms of the corresponding y-components, only the E_y and H_y terms are present in the two equations. To solve the equations for a discrete grid, these terms are substituted by a linear or second order interpolation or shape function, which leads to an approximation of Maxwell's equations with a residual (NGI, 2010). The weighted residual procedure is used to minimize the residual averaged over the area of each grid cell, and integration over the area of each respective element. The source is represented by a 2D Dirac delta function, representing an electric dipole source in line with the horizontal model axis. The resulting equations for the electric inline source are assembled for each finite element. The response is convert back to the (x,y,z)-space, by integrating all the wavenumber responses. The wavenumber sampling is defined by the minimum and maximum offsets for which an accuracy of 1 % relative error is required, and based on empirical testing (NGI, 2010).

Discretization

The input to the forward modeling engine is a geometric representation of the subsurface, where material properties are assigned to given areas. These areas are separated by straight line segments, and each area/layer can be assigned with different resistivity and anisotropy values. The layers can be assigned homogeneous material properties, or with gradient material properties within a layer by discretizing the layer with a specified grid, populated by material properties with a vertical gradient. This gridding is mainly for inversion purposes, where each grid cell is assigned a material property value, and the initial values represent the a priori model.

For the finite element forward modeling, the model geometry has to be subdivided into finite elements, and this is done by a grid of either rectangles or triangles. The modeling mainly use triangle elements, as this provide the highest flexibility when it comes to subdividing the model, as it can represent any geometry. In order to reduce boundary effects large domains are added at the boundaries of the defined model. To the sides and base of the model the CSEM signal is absorbed, while the top boundary

represents the water-air interface, with infinite resistivity, in order to include the airwave in the forward modeling.

In *ngi25em* a so-called Delaunay triangulation is used for generating triangular meshes for given geometries in the finite element modeling. In such a mesh the Delaunay criterion is valid for all triangles, stating that the circumcircle of each triangle contains no other nodes than those of the triangle itself (NGI, 2010). The Delaunay triangulation is generated by starting with a single triangle covering the whole model, and normally more, and whenever a new node is inserted to define geometries, it is attached to all the nodes of the triangle it is enclosed by, and the one triangle becomes three.

The mesh generated by such Delaunay triangulations will only consist of the nodes defined in the model geometry, and thus be too coarse for finite element modeling. A refinement procedure based on Ruppert's Delaunay Refinement (Ruppert, 1995) is applied to increase the mesh density. This adds an additional node in the center of a triangles circumcircle if any internal angle of the triangle exceeds a given value. It also checks whether any other node is within the circle defined by the midpoint of each line of the geometry, and diameter equal to the length of the line segment. If so, a new node is placed at the center of the line segment. The triangulation will also refine the mesh until no triangle has an internal angle below a specified value, set to 20 degrees for all the inversions performed in this study.

Several additional conditions are defined to ensure that the meshing is fine enough for the finite element calculations of the electromagnetic wave field to produce accurate results, while at the same time the number of elements are kept as small as possible. The most important parameter for determining the correct mesh density at a given location in the model is the skin depth. In practice 1 or 2 triangles/elements per skin depth are appropriate (NGI, 2010). The higher number of elements per skin depth, the finer grid/mesh is used in the calculations. In the forward modeling and inversions performed in this study, 1 element per skin depth have been applied.

The modeling engine can apply so-called reciprocity, in order to minimize the computation time. This concept allows for switching source and receiver positions and directions for the finite element calculations. The motivation behind this is that usually the model contains many sources and relatively few receivers, so in the forward model calculations a large number of right hand sides in the linear equation system generated by the finite element system have to be calculated. By switching source and receiver positions this can be done more efficiently.

3.2 Inversion

The inversion part of the software includes three programs; a *data browser* to create inversion datasets, an *inversion GUI* to create and edit inversion project files, monitor the progress of the inversion and display the results, and the inversion program that reads the inversion project file and performs the inversion calculations.

Data browser

The purpose of the data browser is to prepare the EM datasets for inversion, and the resulting data file is used as input to the inversion. Both forward modeling data files containing synthetic data, and data files containing data from EM surveys, can be imported into the data browser. The EM data can be displayed as AVO and PVO for selected receivers and frequencies, and edited in terms of removing selected data (e.g. specified frequencies, receivers, components etc.), defining values for data errors, and deactivation of data points of bad quality by masking. This mask function can also be used to deactivate data points outside a desired offset range. Figure 3.1 shows the user interface of the data browser, where the CSEM towline, source points and receiver positions are plotted in the left window, followed by the data selection window where which data to be displayed and edited can be selected, sorted by frequency and receiver, and PVO and AVO in the upper and lower right windows, respectively.

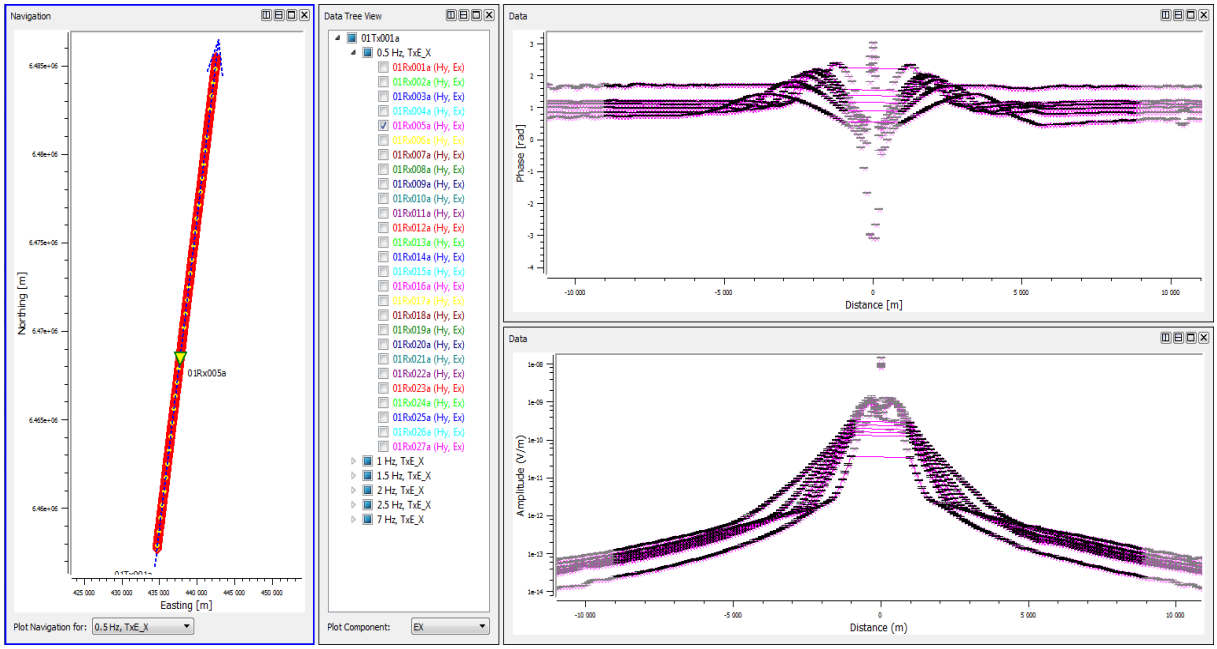

Figure 3.1: The user interface of the *ngi25em_data_browser*. The left window shows the towline with source and receiver positions, followed by the data selection window with data sorted by frequency and receiver, and PVO and AVO in the upper and lower windows to the right, respectively. In the AVO and PVO plots the faded data for offsets larger than 9 000 m and smaller than 1 000 m represents deactivated data, which will not be included in the inversion.

The basic parameters that can be defined in the data browser are the data error estimates, the sampling density, the offset range for data points to include in the inversions, and which frequencies and electromagnetic components to include. The data error estimate specifies an error interval around the recorded data, which means that the data can be assumed to lie within this range when uncertainties are accounted for. The amplitude error is defined as a percentage of the actual data value, while the phase error is defined by a constant radian value. Figure 3.2 shows the magnitude measurements of an electric field before and after the data errors have been estimated, with the original measurements to the left, and with an error estimate of 3 % to the right.

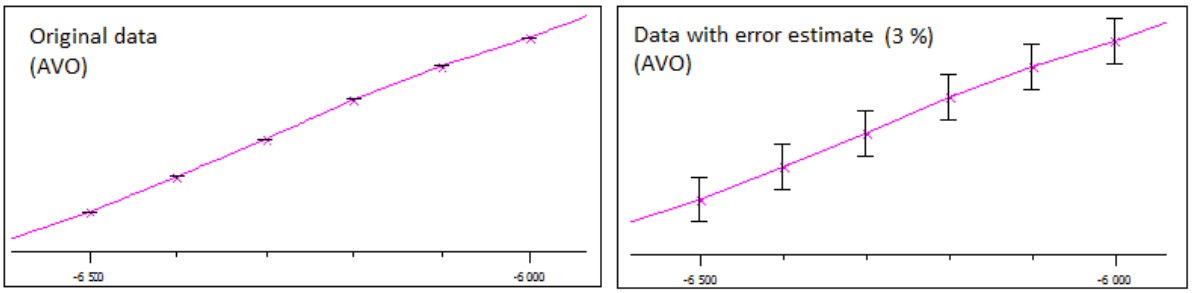

Figure 3.2: Magnitude measurements of an electric field before (left) and after (right) estimating the data errors to 3 %. The figure is zoomed in on a larger curve, with offset along the horizontal axis, and magnitude along the vertical.

In reality, the electromagnetic signal is continuously emitted from the HED source. However, when the data is sampled and discretized, the source signal is transformed to source points. The sampling density of the data can be redefined by resampling the source positions to a constant source point interval. In real surveys, the receivers are placed with unequal spacing, so the source positions will vary from receiver to receiver, and make the forward modelling calculations in the inversion computationally demanding. Resampling the data at a constant interval, will make the computations less demanding. It is also advantageous to resample the data at a larger sampling interval, since less source points will require less calculations during the inversion, and reduce the computational time for each iteration in the inversion. However, it is important to not apply a too coarse sampling interval, as this can cause important information to be lost if the resolution is significantly reduced. Figure 3.3 shows the 2008 CSEM towline from Sleipner, with original source positions (red circles) with an average spacing of 130 m to the left, and the source positions resampled at 300 m to the right.

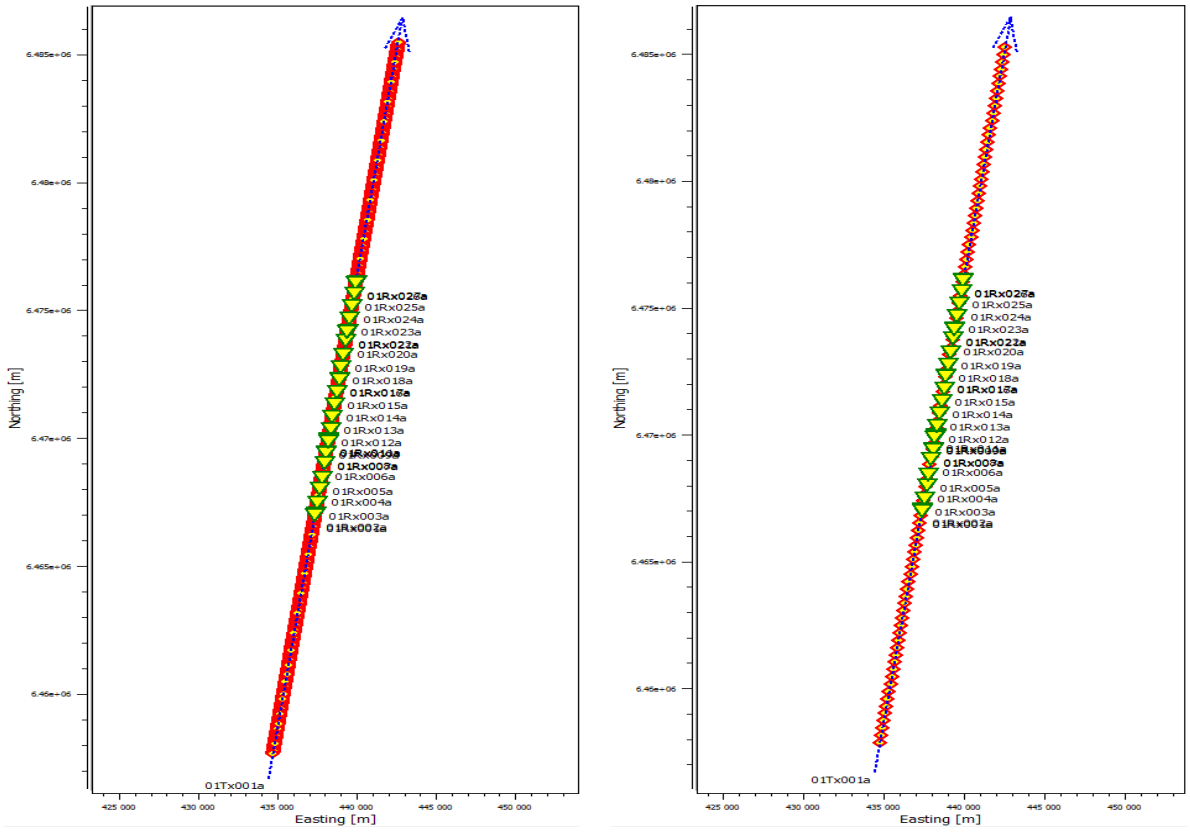

Figure 3.3: The 2008 CSEM towline from Sleipner with receivers (yellow triangles) and source positions (red circles). The original average source sampling interval of 130 m is plotted to the left, and the source points resampled at 300 m to the right.

In addition to the data browser, Matlab was used for data editing purposes. For some of the inversions performed in the study, Matlab filtering was applied to the dataset before it was imported into the data browser, in order to remove data from specified receivers, and also from specified source point intervals. For convenience, these Matlab scripts also filter out specified offset data and electromagnetic components, though this could have been done in the data browser as well.

Inversion

The guided user interface part of the inversion program (Inversion GUI) is used to create and edit inversion project files, and to monitor the inversion progress and display the inversion results. The input data file containing the measured data, prepared in the data browser, is specified in the inversion GUI. Both the inversion project file and the data file are used as input to the inversion program, which reads the specified project file, and performs the inversion.

In the inversions, a Levenberg-Marquardt algorithm (Levenberg, 1944; Marquardt, 1963) is used for optimization of the inversion problem. This is a damped least-squares method, used to solve non-linear least squares problems and curve-fitting, and is a gradient-based algorithm. Inversion using the

Levenberg-Marquardt algorithm is an iterative process, and follows the schematic inversion process in Figure 2.6 in section 2.3. The implementation is based on Auken & Christiansen (2004), with some modifications (NGI, 2010). Not all of the regularization terms in Auken & Christiansen (2004) are applied in the inversions, like the a priori depth values and lateral constraints. The regularization terms that are employed in the *ngi25em* inversions are a specified a priori expectation value for the inversion model, and a roughening term that will ensure a smooth resistivity model. Smooth models are desirable when inverting CSEM data, as the method has relatively low resolution, and cannot resolve sharp resistivity contrasts. When introducing a roughening term, the parameter variations are restricted for neighboring cells in the inversion model.

In Vöge, Park, & Viken (2014), the inversion problem employed in *ngi25em* is described by

$$\big(A + \mu diag(A)\big)\boldsymbol{\delta}_p = \boldsymbol{J}^T \boldsymbol{C}_{obs}(\boldsymbol{d} - \boldsymbol{f}_m) + \boldsymbol{R}^T \boldsymbol{C}_c(-\boldsymbol{R}\boldsymbol{m}) + \boldsymbol{C}_p(\boldsymbol{m}_p - \boldsymbol{m}) \tag{3.3}$$

with

$$A = \boldsymbol{J}^T \boldsymbol{C}_{obs} \boldsymbol{J} + \boldsymbol{R}^T \boldsymbol{C}_c \boldsymbol{R} + \boldsymbol{C}_p \tag{3.4}$$

Where $\boldsymbol{m}$ is the current model parameters, $\boldsymbol{J}$ is the Jacobian matrix (first-order partial derivatives) of $\boldsymbol{m}$, and $\boldsymbol{f}_m$ is the modeled data. $\boldsymbol{m}_p$ is the a priori model parameters, $\boldsymbol{d}$ is the measured data, and $\boldsymbol{R}$ is the roughening matrix, with the corresponding covariance matrices $\boldsymbol{C}_p$, $\boldsymbol{C}_{obs}$ and $\boldsymbol{C}_c$. μ is a damping factor on the difference between the current model and the next, while $\boldsymbol{\delta}_p$ is the change in model parameters, resulting from the equation. The model parameters for the next iteration is defined by $\boldsymbol{m}_{new} = \boldsymbol{m} + \boldsymbol{\delta}_p$. The RMS misfit is described by

$$rms = \delta \boldsymbol{d}^T \boldsymbol{C}_{obs}^{-1} \delta \boldsymbol{d} + \delta \boldsymbol{m}_p^T \boldsymbol{C}_p^{-1} \delta \boldsymbol{m}_p + \delta \boldsymbol{R}^T \boldsymbol{C}_c^{-1} \delta \boldsymbol{R} \tag{3.5}$$

The desired weighted RMS misfit of the cost function have to be specified for the inversions. A normalized misfit of 1 means that the data are perfectly fitted within the error estimate, and is the ideal result. In this study, a desired RMS misfit of 1 was applied, and the smoothing operator was assigned a high weight to generate smooth models. The smoothing operator is used to define the values in $\boldsymbol{C}_c$, which controls the roughness. The weight of the a priori model, which defines the values in $\boldsymbol{C}_p$, was set to zero, in order to reduce the dependence on the a priori model.

4 Forward modeling of CSEM data

This chapter presents the inversion setup and results from a forward modeling study performed using the *ngi25em* forward modeling engine, with the aim of studying the sensitivity of the CSEM method to different model parameter variations. Forward modeling sensitivity studies should be used in the planning of CSEM surveys to determine the best survey configuration for the intended target structure, but are also useful to support interpretation of CSEM data. In more advanced sensitivity studies inversion of synthetic data produced by forward modeling can also be included, which is demonstrated in the study of the synthetic Skade data in chapter 7. The main purpose of this forward modeling study is to demonstrate the variations in the CSEM response when different inversion parameters are varied. The study is conducted for a simplified model of the subsurface, both in 1D and 2D, with variations in signal frequency, water depth, background resistivity and varying target parameters such as target depth and target thickness. The response of the inline electric field is studied.

4.1 Forward modeling setup

For the 1D model a survey configuration with one source, 30 m above seabed, an offset range from 500 to 15000 m, and receivers placed every 100 m at seabed, was employed. A target thickness of 100 m, target resistivity of 50 Ωm and water resistivity of 0.3125 Ωm were kept constant, while the frequency, background resistivity, target depth and water depth were systematically varied, to see the effect on the electric field response. Figure 4.1 shows the 1D model, with background resistivity of 1 Ωm, target depth of 1000 meters and water depth of 1000 meters, which was used as the basis for the 1D model variations.

For the 2D model, sources were placed 30 m above seabed with 100 m spacing, with an offset range from 500 to 15000 m, and receivers every 2 km between -9000 and 9000 m at seabed (10 in total). A water resistivity of 0.3125 Ωm, water depth of 400 meter, background resistivity of 1 Ωm and target resistivity of 50 Ωm were kept constant, while the target depth, width, position and thickness were systematically varied. Figure 4.2 shows the 2D model, with target depth of 1000 meters, target width of 10 km and target thickness of 100 m, which were used as the basis for the 2D model variations.

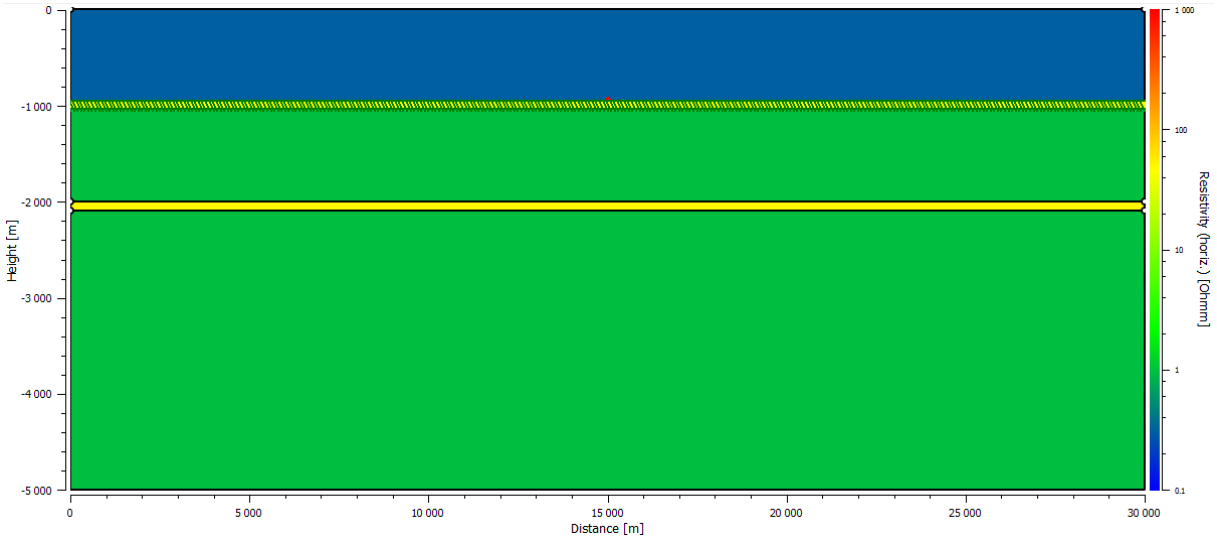

Figure 4.1: 1D model employed in the forward modeling study. The model consists of a 1000 m thick water layer of 0.3125 Ωm, above a 1 Ωm subsurface with a 100 m thick target of 50 Ωm, at a depth of 1000 m. Receivers are placed at seabed, with 100 m spacing, and one source placed 30 m above seabed at the midpoint of the model.

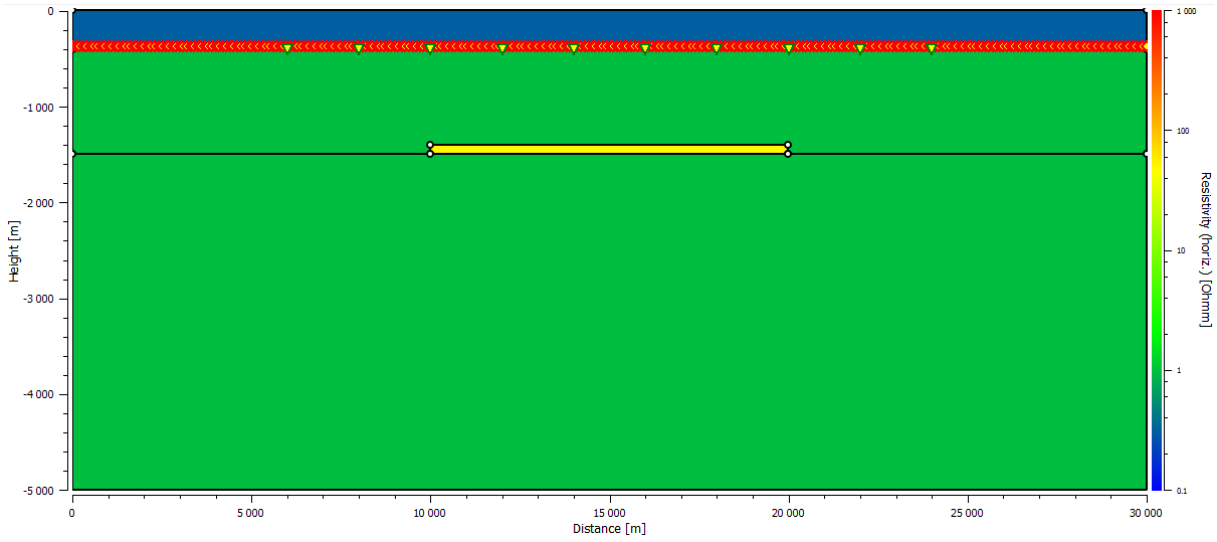

Figure 4.2: 2D model employed in the forward modeling study. The model consists of a 1000 m thick water layer of 0.3125 Ωm, above a 1 Ωm subsurface with a target of 50 Ωm, 100 meter thick and 10 km wide, at a depth of 1000 m. 10 receivers are placed at seabed, with 2 km spacing, and sources are placed 30 m above seabed with 100 m spacing.

4.2 1D Forward modeling results

The results from the 1D forward modeling are presented in the following section, and demonstrate the effect on the modeled CSEM response when different model parameters such as background resistivity, target depth and water depth are varied. Figure 4.3 shows the magnitude (measured in V/m) of the CSEM response for varying frequencies (left) and varying background resistivity (right), when the other model parameters are fixed. When varying the background resistivity, a frequency of 0.25 Hz was employed.

The results show that the magnitude of the electric field decreases with increasing frequency. This can be explained by the decrease in skin depth, and consequent increase in attenuation, for higher frequencies. The magnitude of the electric field increases with increased background resistivity, due to the increase in skin depth with increased resistivity. The effect on the skin depth when changing the background resistivity or the frequency of the signal, can be seen directly from equation 2.8 in section 2.1.1.

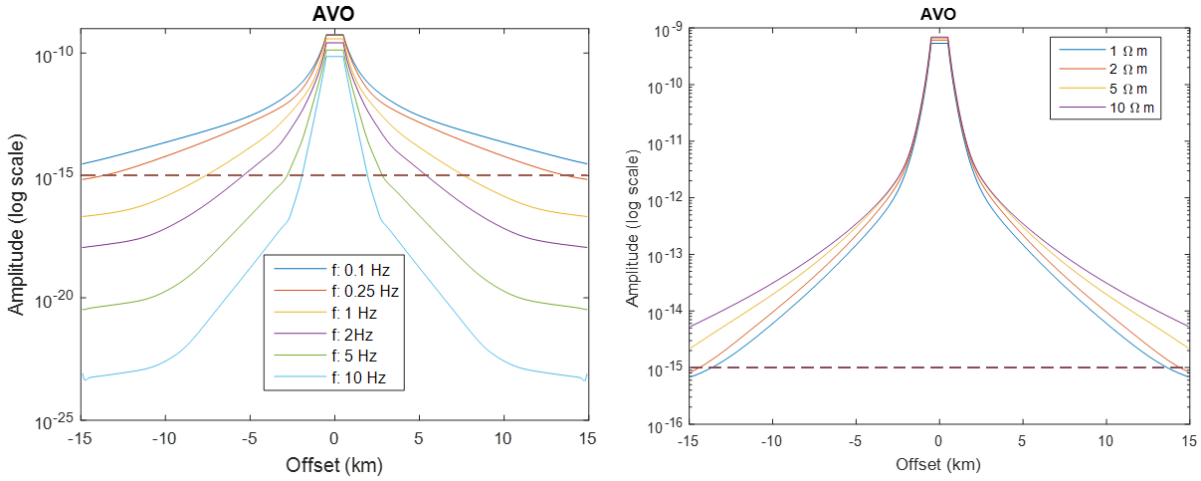

Figure 4.3: AVO (measured in V/m) for the CSEM response from 1D forward modeling for varying frequencies to the left, and varying background resistivity to the right. When varying the background resistivity, a frequency of 0.25 Hz was employed. The dashed line represents the noise level of 10^{-15} V/m.

Figure 4.4 demonstrates the effect in the modeled CSEM response when the depth of the target is varied. For this case a 0.25 Hz frequency was employed, and the background response without the presence of the target was also modeled. The results mainly show a larger magnitude and a more slowly changing phase with offset in the presence of a target structure of higher resistivity, compared to the background model without the target. The results demonstrate that the magnitude of the CSEM response is larger for shallower targets, and thus also the deviation from the background response (nAVO). The deeper the target is located, the longer the EM signal has traveled through a less resistive media, and has thus been attenuated more. The normalized responses also show how the measured response differ mostly from the background response for a given offset range, corresponding to the offsets where the guided mode response dominates. The shallower the location of the target is, the wider is the offset range where the target response can be distinguished from the background response. The largest difference in the responses seem to be for offsets around 7000 m for the magnitude (largest nAVO), and right above 5000 m for the phase (largest nPVO). However, in the case of 2000 m target depth, the nPVO seem to be largest for offsets around 7000 m.

From the AVO and PVO plots, the phase seem to have larger variations, and be more sensitive to the target structure and the target depth variations. However, the magnitude of the field is plotted

logarithmically, so the magnitude variations would appear larger with a linear scale. This makes it difficult to compare the two plots. Since the normalization of nAVO and nPVO is calculated in different ways, the scales of these plots are not really comparable either.

Forward modeling was also performed with the same configuration, for different frequencies. For lower frequencies, the offsets where the maximum nAVO and nPVO could be observed were larger, and smaller for higher frequencies.

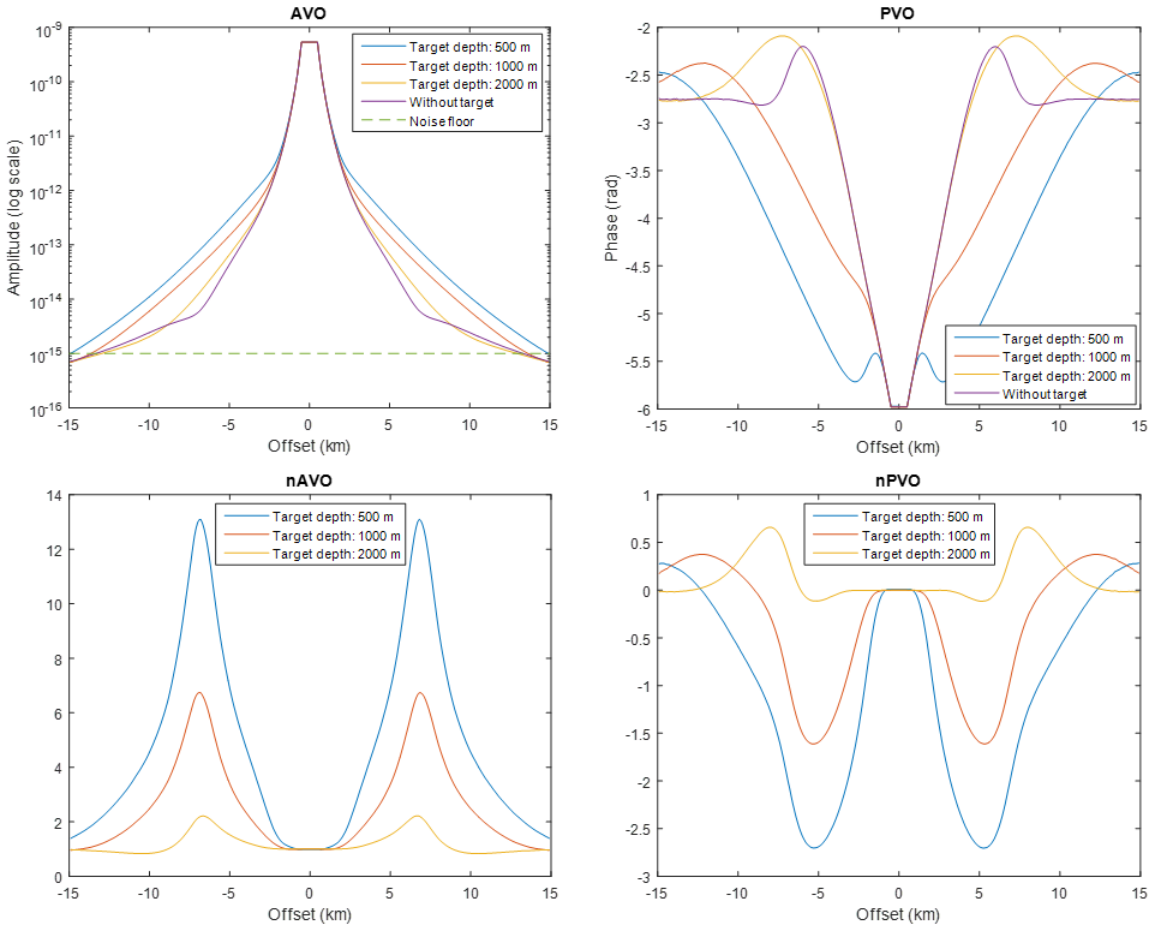

Figure 4.4: The upper row shows the AVO (left) and PVO (right) of the modeled CSEM response of a 0.25 Hz signal for three different target depths, as well as the background response without the target. The bottom row shows the magnitude (left) and phase (right) normalized with respect to the background response.

The magnitude of the measured CSEM response for a 0.25 Hz (left) and 1 Hz (right) signal, with varying water depths, can be seen in the two upper plots in Figure 4.5. The two plots below show the corresponding phase response of the two signals. The other model parameters are fixed, so the difference in the response is only related to the varying water depth. The results demonstrate how the onset of the airwave, e.g. the point where the slope of the magnitude and phase curves flatten out, depends on both frequency and water depth. Due to the high resistivity of air, the magnitude of the signal diffusing at the air-water interface is only reduced by geometrical spreading, so when the airwave starts to dominate the

response, the magnitude of the total field will decrease more slowly with offset. The AVO and PVO curves in Figure 4.5 shows that the onset of the airwave will be at shorter offsets for shallower waters and/or higher frequencies. For the 0.25 Hz signal, the onset of the airwave can be detected around 8000 m for 100 m water, around 10000 m for 400 m water, and above 15000 m for 1000 m water. For the 1 Hz signal, the onset of the airwave occurs at much smaller offsets, around 2500 m for 100 m water, around 5000 m for 400 m water, and around 12000 m for 1000 m water.

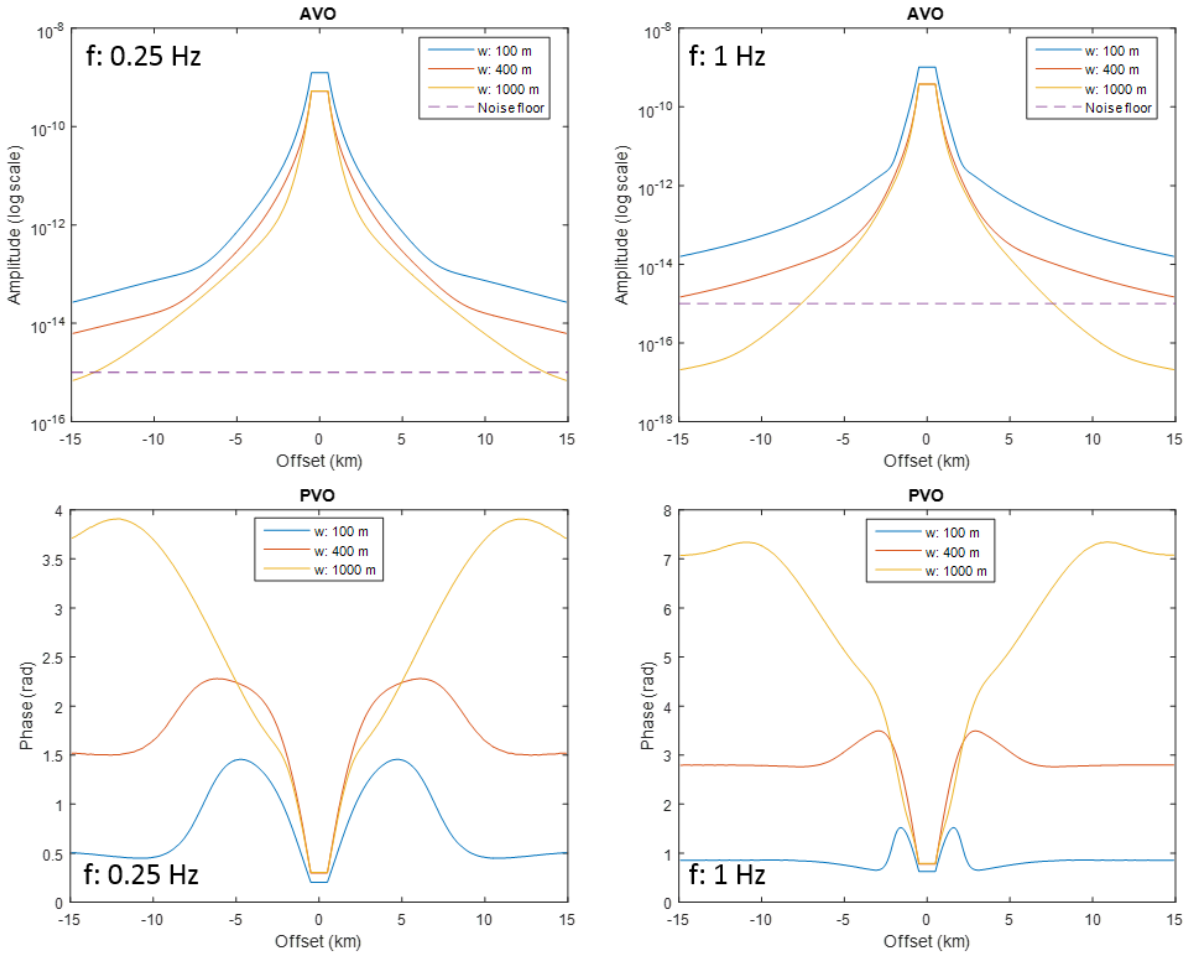

Figure 4.5: AVO and PVO of the CSEM response from 1D forward modeling for varying water depths, for a 0.25 Hz signal to the left, and 1 Hz signal to the right.

To study the target response in a setting similar to the Sleipner case, the response for the case of 100 m water and a target location of -1000 m was studied. This a very simplified approximation, and will not provide results that would be realistic to expect from Sleipner, but they can be helpful to determine at which offset ranges to expect the target response to dominate. Figure 4.6 shows the modeled nAVO and nPVO response for a 0.25 Hz signal. The target response seem to dominate at offsets between 2000 m and 10000 m, approximately. The magnitude of the response when the target is present is larger than the magnitude of the background response for offsets between 2000 m and 5000 m, before it becomes smaller for larger offsets. The signal of 0.25 Hz is of lower frequency than the lowest frequency acquired

in the Sleipner study, which is 0.5 Hz, so smaller offset ranges for the target response can be assumed for the Sleipner data. It is important to keep in mind that these results are obtained from a very simplified 1D model, and the results should be considered with caution.

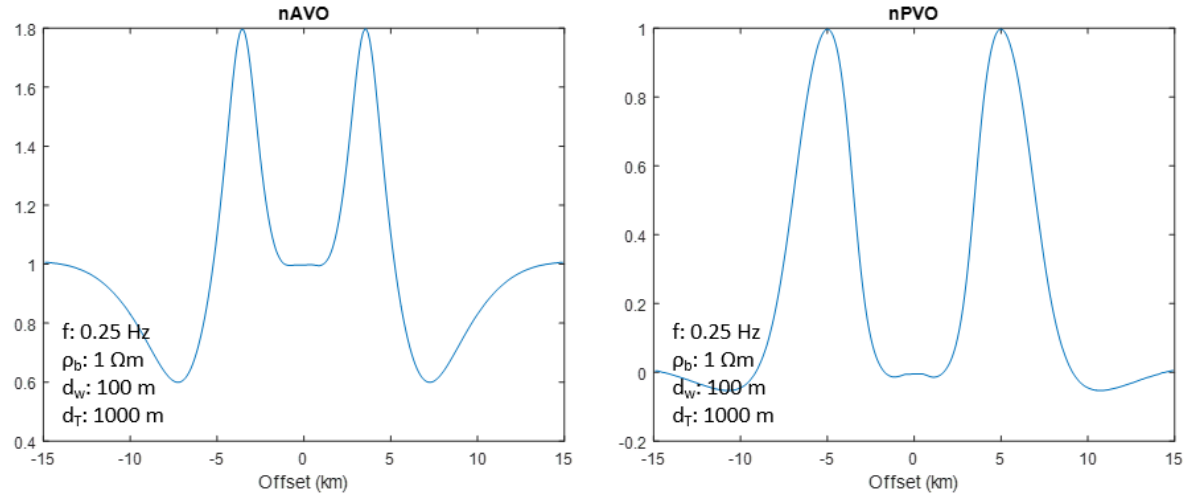

Figure 4.6: nAVO and nPVO of the modeled CSEM response of a 0.25 Hz signal from a 1D model similar to the Sleipner case, with water depths (d_w) of 100 m and target depth (d_T) of 1000 m.

4.3 2D Forward modeling results

The results from the 2D forward modeling demonstrate the effect in the modeled CSEM response for varying target properties such as target depth, target width and target position. In the 2D modeling a 1 Hz signal was employed. Figure 4.7 shows the modeled response over the 2D model for two different target depths, 2000 m to the left, and 1000 m to the right, together with the background response for the same model without the target. The ten different AVO curves represent the measurements form each of the ten receivers, plotted along the survey line, where the midpoint is set to zero. In the case of a target depth of 2000 m, the target response cannot be distinguished from the background response in the figure, and demonstrates how the parameters used in the modeling case make the method insensitive to the target. To be able to distinguish the target response for this case, a lower frequency signal should be applied. For the target located at 1000 m depth, the target response can be distinguished from the background response, for offsets between 1000 m and 6000 m approximately (for each receiver). The difference in the response is quite small, but again, note the logarithmic scale that makes the difference appear smaller than if plotted with a linear scale.

Figure 4.8 shows the modeled response for a target width of 5 km to the left, and 10 km to the right, while Figure 4.9 shows the response for two different positions of a 10 km wide target. Both figures demonstrate how it is mainly the receivers located above the target that are sensitive to the target structure.

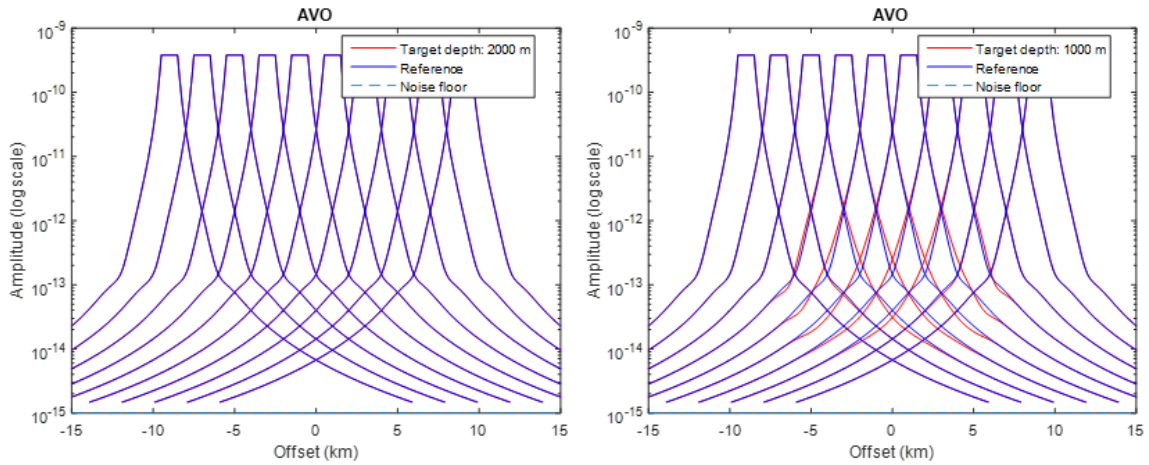

Figure 4.7: AVO of the CSEM response from the 2D model with a target depth of 2000 (left) and 1000 m (right), together with the background response from the model without the target.

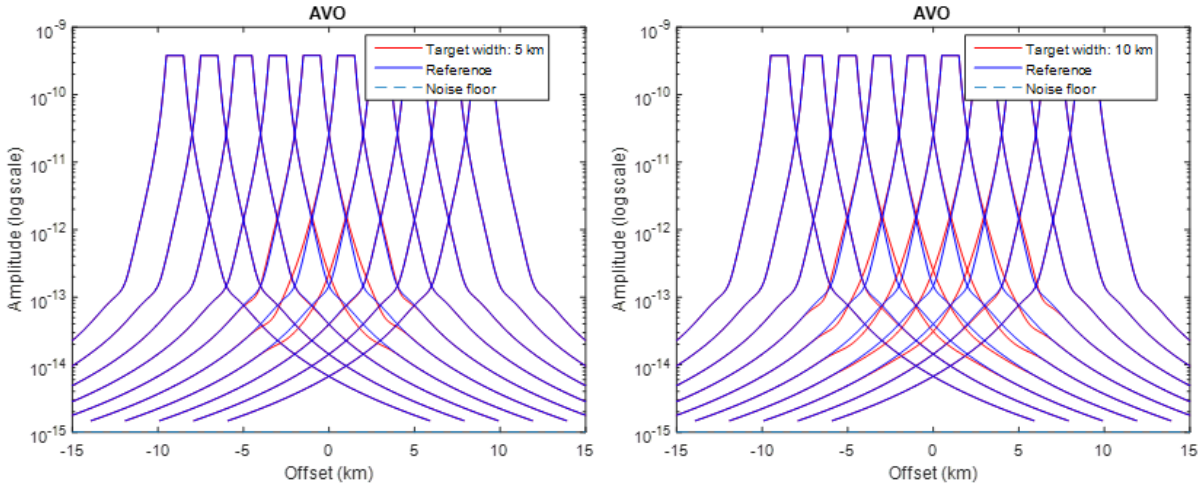

Figure 4.8: AVO of the CSEM response from the 2D model with a target width of 5 km (left) and 10 km (right), and target midpoint at 0, together with the background response from the model without the target.

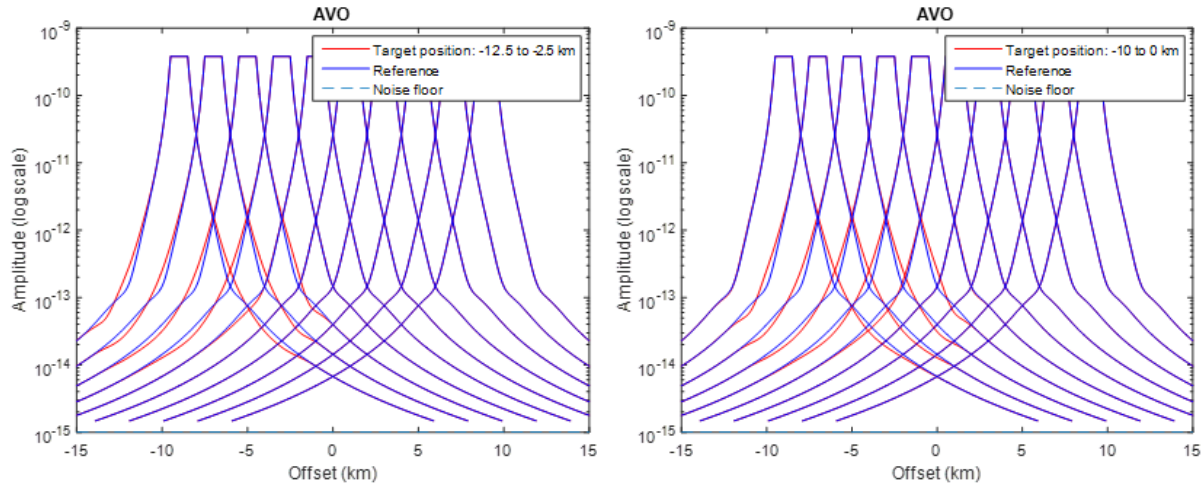

Figure 4.9: AVO of the CSEM response from the 2D model two different target positions, together with the background response from the model without the target.

In Figure 4.10, the magnitude of the modeled CSEM response for a 50 m and a 100 m thick target is shown. The response from the 100 m target model seem to deviate more from the background response, and is also distinguishable for a wider offset range. However, if the resistivity of the target was reduced so that the thickness-resistivity product was to be the same as in the 50 m case, the two results would probably be very similar.

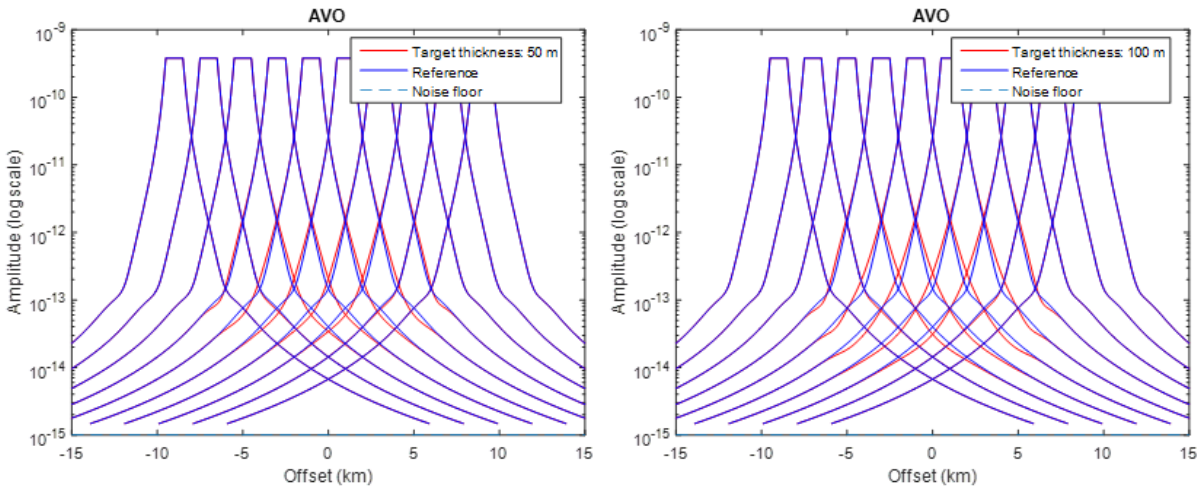

Figure 4.10: AVO of the CSEM response from the 2D model with a target thickness of 50 m (left) and 100 m (right), together with the background response from the model without the target.

In all the results presented in this section the response modeled with the target present seem to be larger than the background (reference) response for a given offset range, before it becomes negative. This was also observed in the 1D forward modeling study, and a positive resistivity anomaly in the subsurface thus seem to generate a positive anomaly followed by a negative anomaly in the normalized response.

5 Inversion of the Sleipner CSEM data

The inversion setup and results from different inversions conducted with the aim of establishing an inversion strategy for the Sleipner CSEM dataset are presented in the following chapter. In the inversion setup, many parameters have to be determined, such as which frequencies to include, which offsets to include, how dense the parameterization of the model should be, the data density, and the parameter values of the starting model (a priori model). In the inversion study of the Sleipner CSEM data, inversions have been performed for a variety of different parameters to study the influence on the resulting resistivity model and optimize the resistivity image resulting from the inversion. All the resistivity models presented in this chapter represent the section along the Sleipner CSEM towline, and are superimposed on the depth converted seismic from 2008, covering more or less the same section. The inversions provide both horizontal and vertical resistivity models, but since the focus of this study is the response from the inline electric field, which is most sensitive to the vertical resistivity of the subsurface, only the vertical resistivity models are presented. The color scale representing the resistivity values in the models is logarithmic, and ranges from 0.2 to 20 Ωm.

Well logs and depth converted seismic from the area were used to determine the a priori inversion models (section 5.1) and the inversion grid (section 5.2) employed in the inversions. The seismic was also used to identify the location and approximate extent of the CO_2 plume, in order to evaluate the inversion results.

The first step in the process of developing an inversion strategy was to perform an inversion for a given set of parameters, where all the frequencies were included, to be able to evaluate the effect on the inversion result when varying different inversion parameters and/or filtering out data. This initial inversion result is presented in section 5.3. The second step was to remove data from receivers with very similar response to reduce the computations in each iteration of the inversion process. This is further discussed in section 5.4.

To approach an inversion strategy, many different inversions were carried out, with different inversion parameter variations. The tuning of the inversion parameters included running inversions for varying frequencies, data density, a priori models and offset ranges, which is elaborated in section 5.5. Section 5.6 presents different approaches to address the challenges related to the influence from the seabed pipelines, while section 0 and 5.8 address the challenges related to the shallow location and the weak resistivity anomaly of the CO_2 plume. One approach is to vary the inversion setup to attempt to improve the inversion result (section 0), while another is to perform inversions constrained only to the layer where the CO_2 is located (section 5.8). In section 5.9 the challenge related to the strong airwave response in the Sleipner CSEM data is addressed.

For the initial inversions performed in this study the amplitude- and phase errors have been set to 3 % and 0.01 radians, respectively. These are the default values in *ngi25em,* expected to lie within the typical error range of EM data in general. Due to the low noise level for CSEM data, these errors are assumed to be representative for the Sleipner data in the in initial inversions. However, after other inversion parameters have been optimized, inversions with varying error estimates were also conducted, in order to find the optimal data error estimates for the dataset.

The criteria that have been emphasized when evaluating the inversion results in the inversion study of the Sleipner dataset are;

1. The presence of a resistivity anomaly in the area of the CO_2 plume, and if present;
    - The strength of the anomaly
    - The location of the anomaly compared to the location of the CO_2 plume defined by the depth converted seismic
2. Realistic resistivity values and geometries in the resistivity image. The main focus of this is the upper half of the resistivity model, which is of higher interest since this is where the CO_2 plume is located.

5.1 A priori model

Based on well logs and seismic, two different a priori models were defined for the inversions. The different resistivity logs provided varying information, and since none of the available well logs are from within the area of the CO_2 plume, this was a challenging task. The defined models are just educated guesses of the subsurface resistivity, which leads to uncertainties in the inversion results due to the dependence of the parameters defined in the initial model. The uncertainty related to the layer boundary positions was taken into account by defining a high smoothing factor both inside the layers and at the layer boundaries. This allows for smooth resistivity transitions within the layers, and also across layer boundaries, which avoids the model to be constrained by the predefined layers in the a priori model. The uncertainty of the a priori model was also considered by applying a weight of zero to the a priori model in the inversions.

In spite of the varying information in the well logs, they provided some indications of the subsurface resistivity in the area. For example, the deeper parts of the model, from between 2400 to 2600 m depth, seem to be characterized by a higher resistivity, between 5 and 10 Ωm. For the rest of the model the resistivity seem to be somewhere between 0.5 and 5 Ωm, mostly between 1 and 2 Ωm. In the well data from well 15/9-13 provided by Statoil, a thin layer of higher resistivity is present at seabed, but this is not present in the well log data from NPD.

The depth of the a priori models extend from the sea surface at 0 m, down to a depth of 3000 m. The seabed topography is modeled by employing the vertical receiver positions from the CSEM data file to define the seabed boundary. The water column is around 80 m, and the water resistivity was set to 0.3125 Ωm. In both a priori models, the subsurface is divided into five layers, all with an anisotropy factor (ρ_v/ρ_h) of 1.5, but with different layer resistivities. The properties of the two models can be seen in Figure 5.1 and Figure 5.2, and they will hereafter be referred to as M1 and M2, respectively. The differences in the models reflect the differences and uncertainties in the well logs, as the two upper layers and the base layer are assigned with lower resistivities in M2.

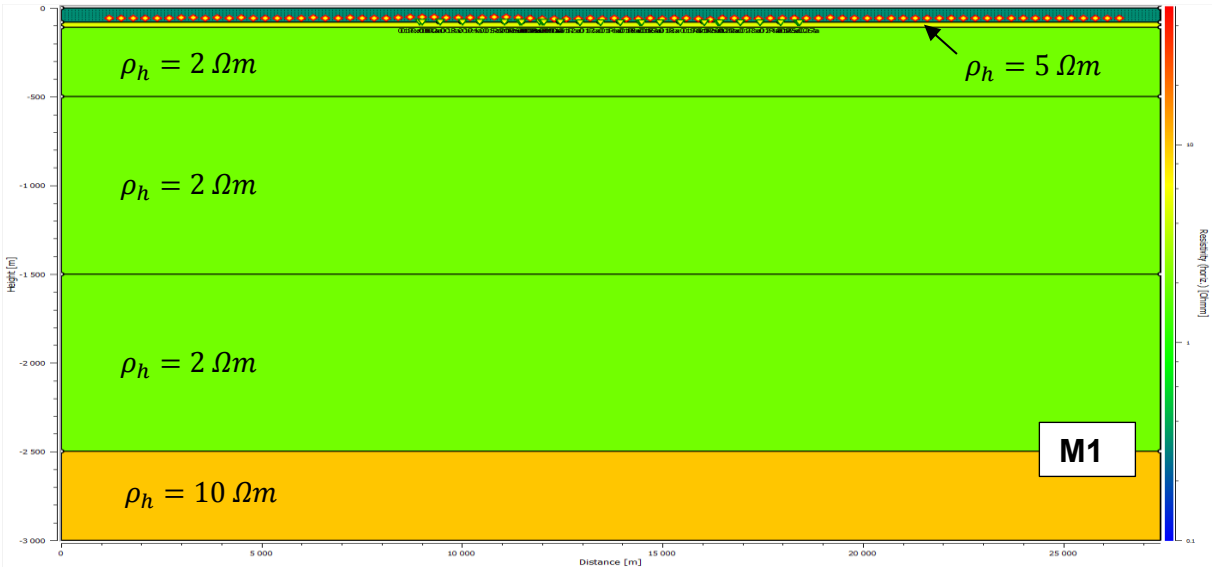

Figure 5.1: A priori model M1. The model is divided into a water layer of approximately 80 m, and 5 subsurface layers. The upper layer represents the seabed, with a thickness of 30 m.

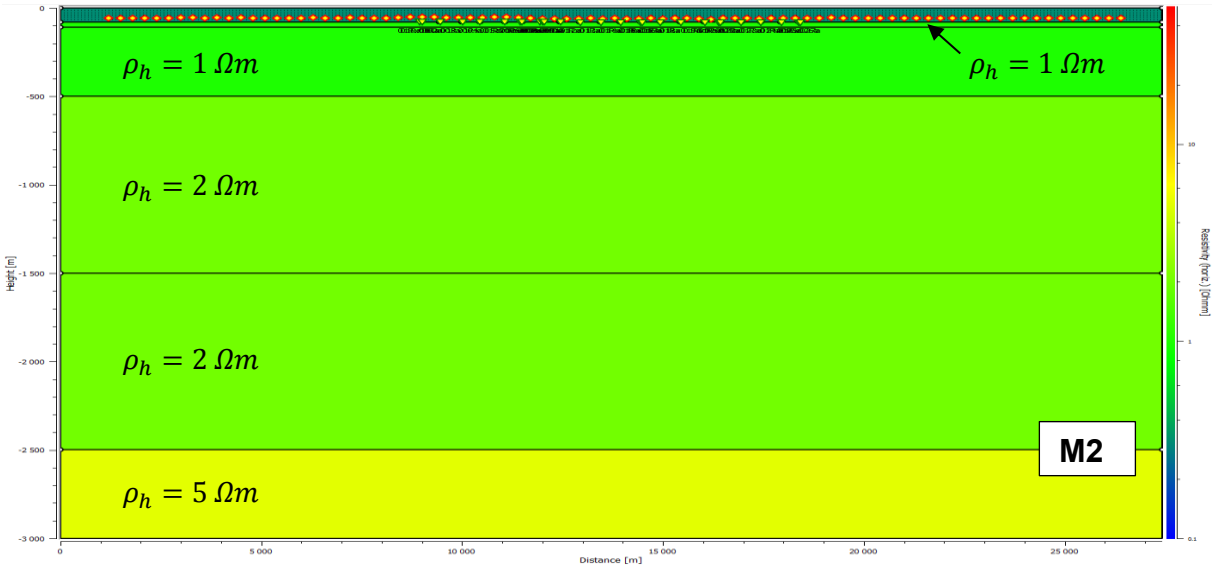

Figure 5.2: A priori model M2. The model is divided into a water layer of approximately 80 m, and 5 subsurface layers. The upper layer represents the seabed, with a thickness of 30 m.

5.2 Inversion grid

The inversion grid divides the layers of the inversion model into cells. In the inversion process, each cell can be assigned with different resistivity values, so the grid defines the resolution of the model. Different layers can be gridded with different resolutions, but the denser the grid of the model is, the more calculations have to be performed in the inversion process, and thus each iteration will take more time. Since the towline covers a large area to each side of the receiver line, there is less data from these areas, and the sensitivity is lower. Consequently, the inversion result are of less confidence and poorer resolution in these areas of the model, and a coarser gridding is therefore applied here. Also, it would be natural to define a grid that is coarsening with depth, as the resolution of the data decrease.

Figure 5.3 shows the three different grids that were employed in the inversions. Grid 1 is quite dense in the whole area below the receiver line, all the way down to 1500 m depth, where it gets coarser. This grid was mainly used for datasets with smaller amounts of data, e.g. when only inverting for single frequencies. For larger datasets, this grid would require a lot of time for each inversion, and thus the coarser grid 2 was applied. Grid 3 is basically a mix between Grid 1 and 2, where only the area between -500 m and -1000 m is densely gridded, and the horizontal extent of the dense gridding is restricted to a smaller area, between 11000 m and 16000 m along the towline, roughly covering the area of the CO_2 plume. This area of dense gridding was determined from the location of the CO_2 in the seismic. In this grid, the third subsurface layer in the a priori models is divided into two layers, to be able to apply a denser horizontal grid only between -500 and -1000 m.

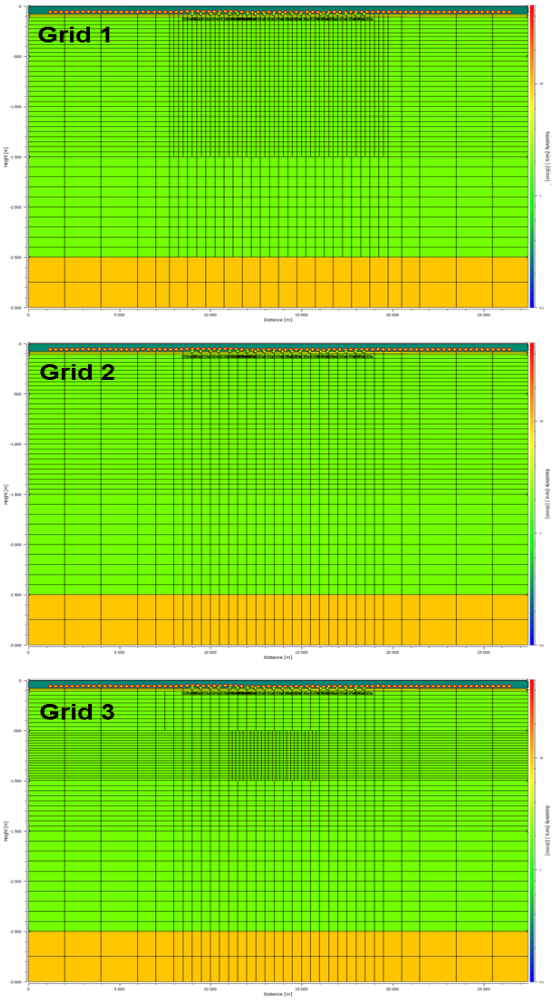

Figure 5.3: The three different grids employed in the inversions of the Sleipner CSEM dataset.

The strategy for the study is to start with a relatively coarse grid while tuning other inversion parameters. When these parameters have been optimized, inversions with a denser grid is tested. A denser grid around the CO_2 plume is applied to try to improve the location and strength of the resistivity anomaly. This will give a better resolution in the target area, and possibly a more detailed image of the plume. A detailed resistivity profile is useful when it comes to CO_2 (and also reservoir) monitoring, as the resistivity

can be used to calculate the saturation and amount of CO_2 present. The resistivity and saturation can be related through EM rock physics, which is further discussed in section 6.7.

5.3 Initial inversion result

An initial inversion was performed to obtain a result that could be applied as a basis of comparison for the resistivity models resulting from inversions performed with different variations of inversion parameters and data. This initial inversion included the response of all the six available frequencies, from all the 27 receivers, and the data was resampled at 300 meters. The 1D forward modeling study in section 4.2 indicated that the target response would be dominating at an offset range between 2000 and 10000 m, for a 0.25 Hz frequency signal, and a very simplified model. Since the lowest frequency available in the Sleipner data is 0.5 Hz, a shorter maximum offset could be expected, and since the frequencies ranges up to 7 Hz, a shorter minimum offset should also be applied. Based on this, data from offsets between 1000 and 8000 m were included in the initial inversion, but different offset ranges are tested later on in the study. The inversion was performed with the coarser Grid 2, and M1 as the initial model. Figure 5.4 shows the resulting vertical resistivity profile. The high-resistivity anomaly corresponding to the CO_2 plume can be observed between -550 and -750 m depth, approximately, considerably shallower than the CO_2 plume in the background seismic. The vertical resistivity in the center of the CO_2 anomaly is 20.4 Ωm.

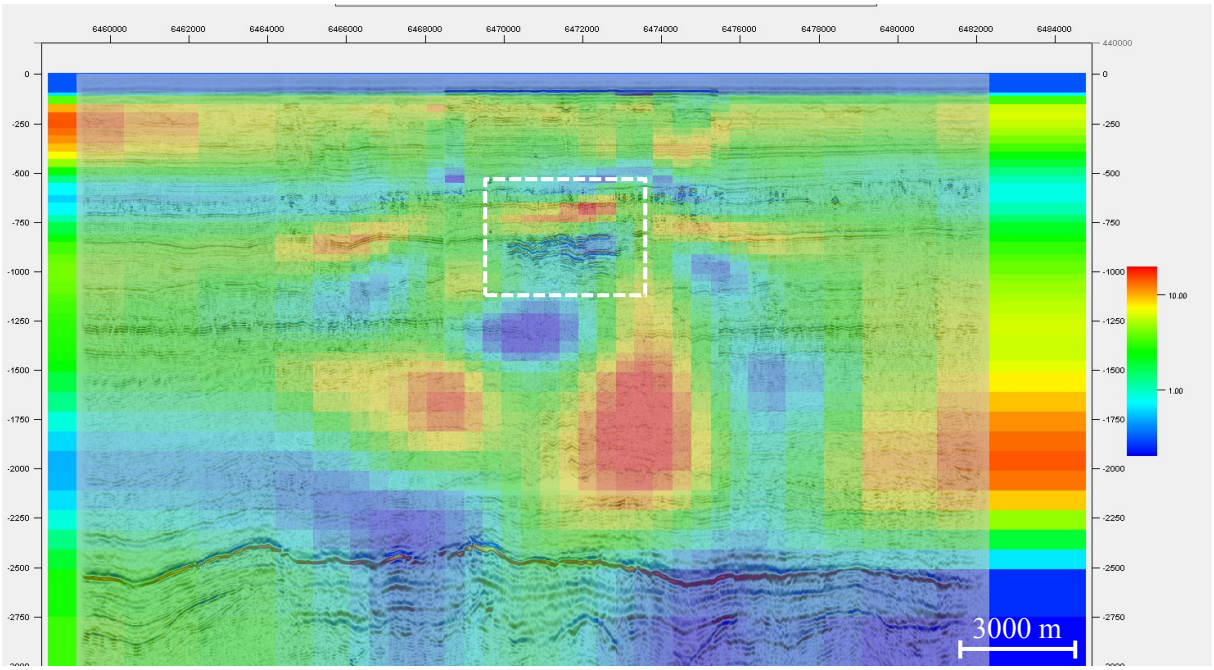

Figure 5.4: Vertical resistivity profile from the initial inversion of the CSEM dataset, where all six frequencies and data from all 27 receivers were included, superimposed on depth converted seismic. The white rectangle marks the location of the CO_2 plume, and the logarithmic color scale shows the vertical resistivity.

The lower half of the resistivity profile is characterized by three areas of higher resistivity around 1300 to 2200 m depth, two located to the left and right of the CO_2 plume, and one at the right boundary of the section. The origins of these are unknown, and no apparent features can be observed in the seismic or well logs to explain the anomalies. Indications of layers of higher resistivity are also present in the upper half of the profile, with a more or less distinct layer around 200 m, and two areas around -750 m, at each side of the CO_2 plume. The deeper parts of the profile are characterized by lower resistivity than expected, with large areas of less than 1 Ωm resistivity below 2000 m depth.

5.4 Removing data from closely spaced receivers

Figure 5.5 shows the Sleipner CSEM survey line to the left (also displayed in Figure 1.5), together with the same survey line superimposed on the seabed pipeline network to the right. As can be seen from both maps, some of the receivers are rather closely positioned, which results in very similar measurements. The AVO of the inline electric field measured by each receiver at 1.5 Hz frequency is plotted along the CSEM survey line in Figure 5.6, and shows how the measurements of the closely spaced receivers 1 and 2, 7 and 8, 9, 10 and 11, 16 and 17, 21 and 22, and 26 and 27 are very similar. This is also the case for the other five frequencies. To reduce the amount of data, and thus the computational time for each inversion, data from seven of these closely spaced receivers were removed; Rx001, Rx007, Rx009, Rx011, Rx017, Rx021 and Rx027), marked in red to the right in Figure 5.5.

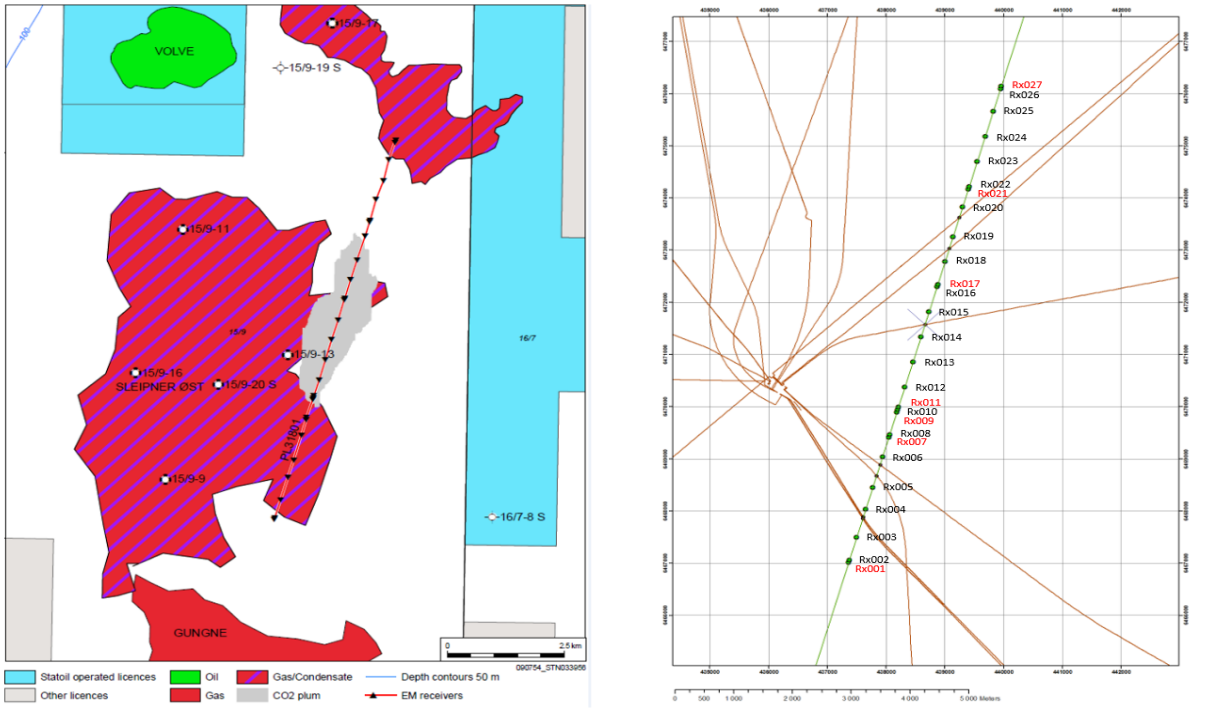

Figure 5.5: CSEM survey line and receiver positions over the Sleipner East field and the accumulated CO_2 plume (left) and the seabed pipeline network (right). Modified from Park et al. (2013). The left figure ranges from latitude 6466000 to 6477400 m, and longitude 434400 to 443000 m.

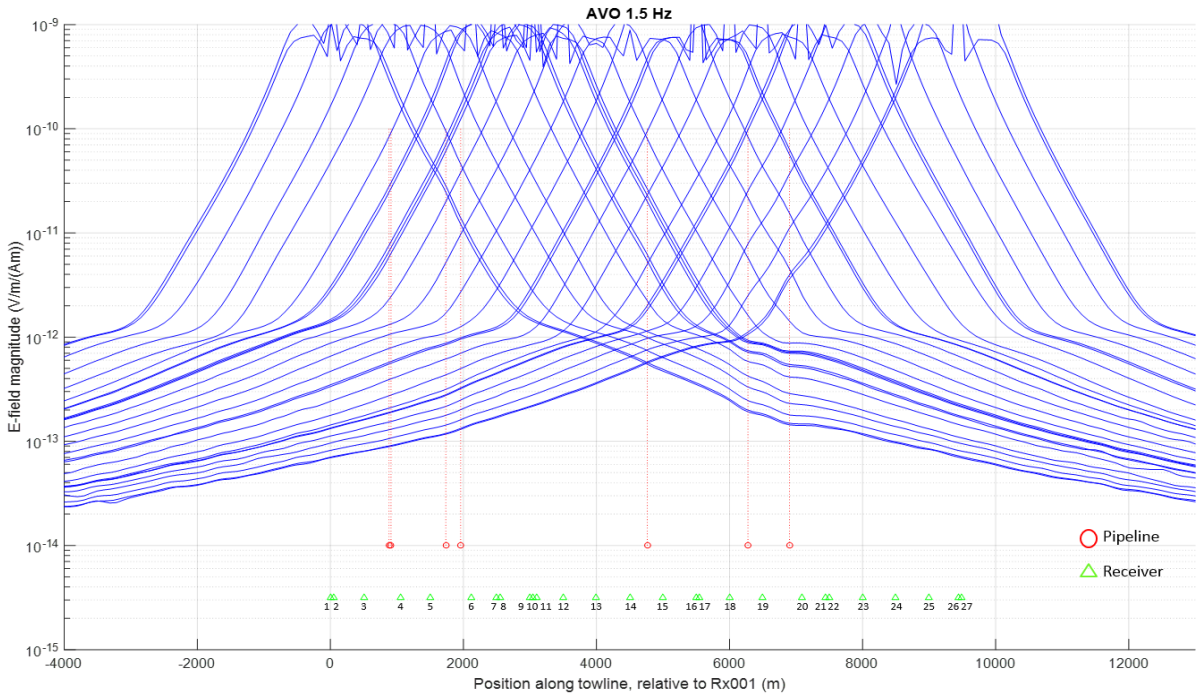

Figure 5.6: AVO for each receiver along the towline, relative to Rx001, for the 1.5 Hz frequency signal. The receiver positions are marked with green triangles. The positions where the pipelines cross the survey line are marked by red circles, and extrapolated with red dotted lines.

Figure 5.7 shows the resistivity model resulting from the same inversion setup as in the previous section, but where data from the seven closely spaced receivers have been removed. The data was filtered out employing Matlab, creating a new data file where the data from the specified receivers was removed. The results before and after these data had been filtered out are nearly identical, which leads to the assumption that the remaining 20 receivers provide sufficient information to provide a representative resistivity image of the subsurface. Based on this, only data from these 20 receivers have been included in the inversions performed further on in the study. However, the resistivity is slightly reduced in the center of the CO_2 plume, which is 18.8 Ωm in this case.

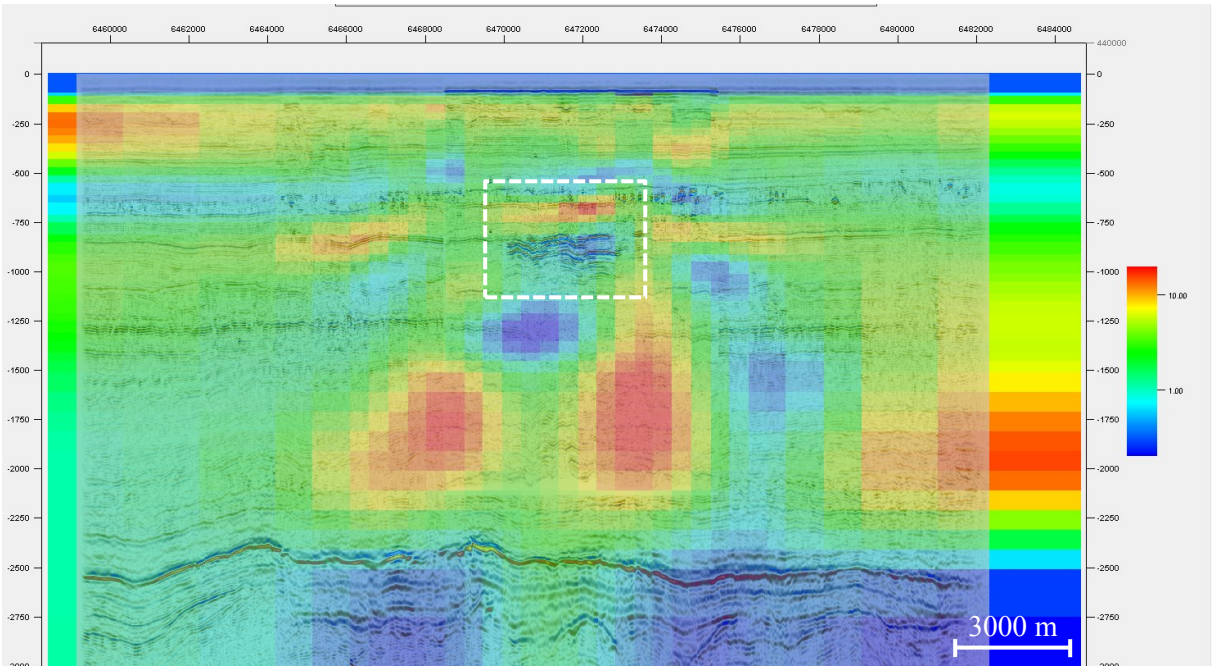

Figure 5.7: Vertical resistivity profile resulting from inversion of the CSEM dataset after removing data from seven closely spaced receivers.

5.5 Tuning of inversion parameters

In the process of developing an inversion strategy, tuning of different inversion parameters was performed, in order to optimize the resulting resistivity model. The inversion process can be very demanding when it comes to computational power, and the more source and receiver data and/or denser subsurface model, the more calculations have to be performed, and longer time is required for each iteration in the inversion process. Tuning of inversion parameters such as the inversion grid, sampling density and what data to include when it comes to frequency, offset range, etc., is a compromise between reducing the amount of data to minimize the computational time, and at the same time optimizing the resistivity model resulting from the inversion. The inversion result depends on all these parameters, and the right combination may yield an improved resistivity image.

Frequency

Initially, inversions for single frequencies were carried out, to see how well they reflected the subsurface separately, and study the target sensitivity for each frequency. Lower frequencies have a lower resolution, but they are sensitive to deeper parts of the model due to the larger skin depth. Higher frequencies are characterized by smaller skin depths, and will be sensitive to the shallower parts of the model. The skin depths for the six frequencies in the Sleipner CSEM survey, in the case of a subsurface resistivity of 2 Ωm, was calculated using equation 2.8 in section 2.1.1. The results are listed in Table 5.1 to demonstrate the skin depth variations.

Table 5.1: Skin depths for the six frequencies in the Sleipner CSEM dataset, calculated from equation 2.8 in section 2.1.1, for a resistivity of 2 Ωm.

Frequency (Hz)	0.5	1	1.5	2	2.5	7
Skin depth (m)	1006.6	711.8	581.2	503.3	450.2	269.0

For the single frequency inversions, Grid 1 and a priori model M1 was applied, and data from offsets between 1000 and 8000 m were included. When only including one frequency in the inversions, the amount of data, and thus the required calculations, are significantly reduced. Hence the denser Grid 1 could be applied, while the time of the inversion still was reduced significantly compared to the initial inversion where all the frequencies were included.

The results from the single frequency inversions are presented in Figure 5.8. For the lowest frequencies, 0.5 and 1 Hz, the tendency of a more resistive area can be observed above the area of the CO_2 plume defined in the seismic, but in none of the results the resistivity anomaly match the seismic well. For the frequencies of 2 and 2.5 Hz, a strong negative resistivity anomaly partly coincides with the plume observed in the seismic, while in the 7 Hz inversion result this negative anomaly is located shallower, and more to the right. A more or less distinct negative anomaly can in fact be observed in all the single frequency inversion results, at the horizontal location of the CO_2 plume, but at varying depths. The depth of the anomaly decreases with increasing frequencies, while its size and strength varies. Another feature present in most of the single frequency inversion results, is two sets of diagonal positive resistivity anomalies. Their strength varies for the different frequencies, but in all the resistivity models they seem to start in the shallow part of the profile, around latitude coordinates 6468500 m and 6473400 m.

None of the single frequency inversion results seem to provide a good resistivity model of the subsurface, nor a satisfying response from the CO_2 plume, when compared to the seismic and the initial inversion result where all the frequencies were included. This implies that multiple frequencies need to be included to obtain a representative resistivity model from inversion.

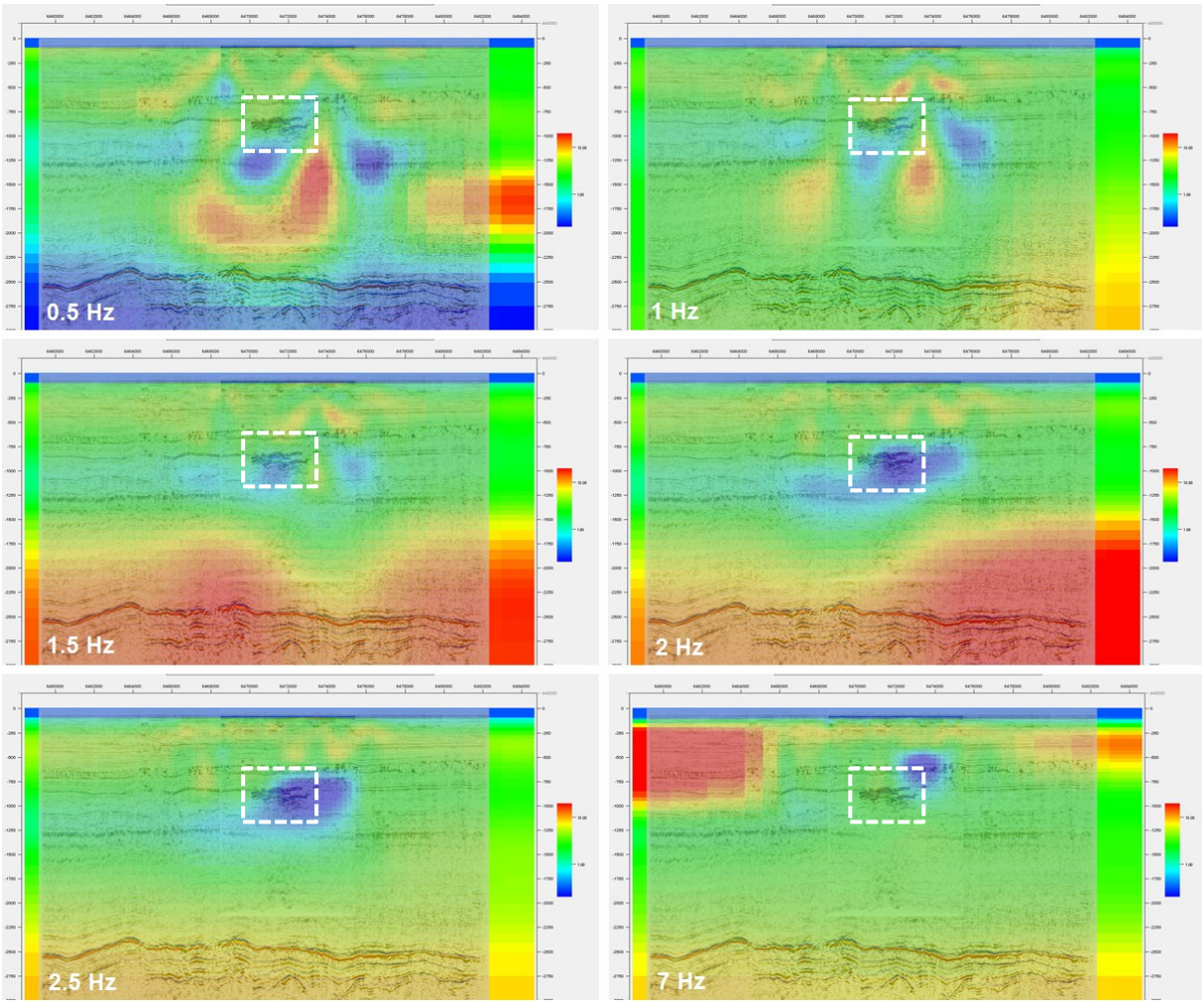

Figure 5.8: Inversion results when inverting for each of the six frequencies separately. The vertical and horizontal scales, and the color scale, are identical to the scales in Figure 5.7. The location of the CO_2 plume in the background seismic is indicated by the white rectangle.

Resampling

In the Sleipner CSEM dataset the average source point spacing is around 130 m. The computational time for each iteration in the inversion process can be significantly reduced by resampling the data at a larger source point interval. The idea is to find the best compromise between computational time and resolution, by reducing the sampling density without losing significant resistivity information. Inversions with resampling of 100 m, 300 m and 600 m were tested for the Sleipner dataset. In spite of the unrealistic results, inversion of single frequencies was employed to see the effect of sampling density variations. This saves time, since these inversions are faster, and the results can still give indications of how the different sampling intervals will affect the inversion results.

Inversions for the different source sampling intervals were performed for data of three different frequencies in the Sleipner dataset, one low (0.5 Hz), one intermediate (2 Hz) and one high (7 Hz).

Figure 5.9 shows the resulting resistivity profiles for the 2 Hz signal, when sampled at 100 m, 300 m and 600 m. For the upper half of the resistivity model, the 100 m and 300 m source sampling interval seem to yield very similar results, while in the result from the 600 m spacing case, larger differences occur. The deeper parts of the model are quite different for all the three sampling intervals. However, the focus should be on the upper half of the model, since the 2 Hz signal is not very sensitive to the deeper parts.

Resampling variations performed for the other frequency signals showed similar results, indicating that resampling the source points in the dataset at 300 m still provides sufficient information to obtain a representative resistivity image of the subsurface. Resampling the data at 600 m proved to be too coarse, and did not provide a representative resistivity model. Based on this, the data is resampled at 300 m in the datasets employed further on in the inversion study.

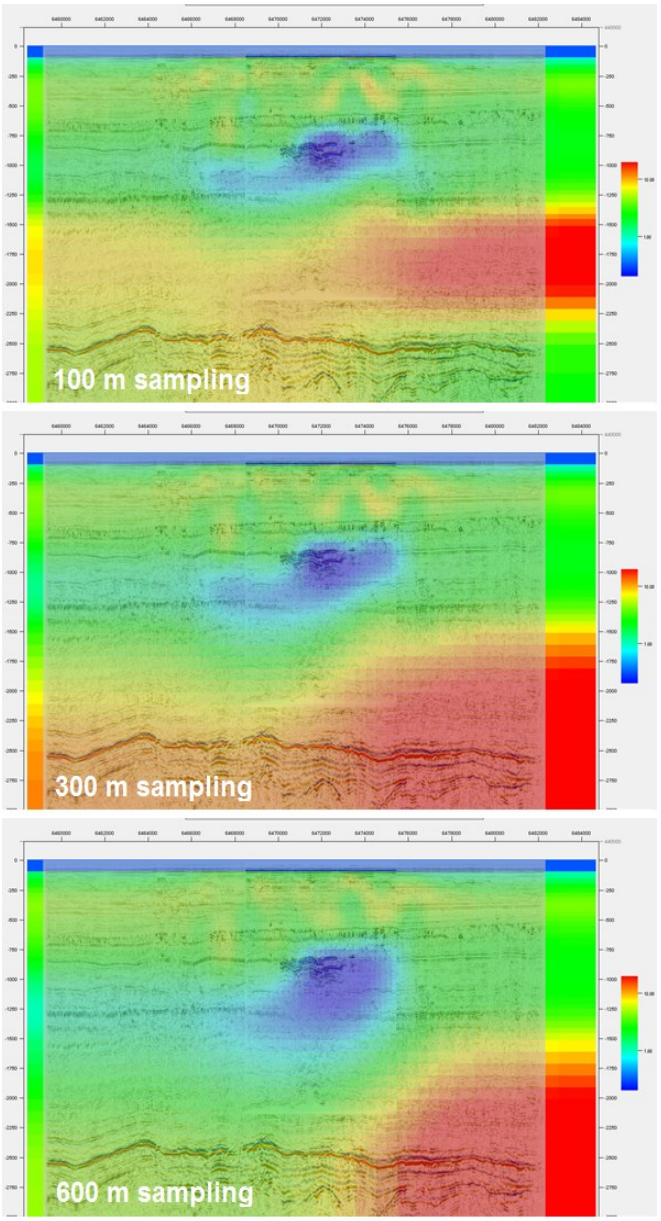

Figure 5.9: Inversion results for the 2 Hz data with a sampling interval of 100 m, 300 m and 600 m. The vertical and horizontal scales, and the color scale, are identical to the scales in Figure 5.7.

A priori model

The inversion setup and dataset employed in section 5.4, where all frequencies were included, the source points resampled at 300 m, and data from the seven closely spaced receivers had been removed, was used as a basis for varying the a priori model and offset range in the inversion setup. Figure 5.10 shows the inversion result when the a priori model M2 was employed instead of M1. Compared to the inversion result where M1 was employed (Figure 5.7), the two starting models give quite similar inversion results, but some differences occur. The high-resistivity area representing the CO_2 plume is located at shallower

depths in the inversion result where M2 was employed. Also, the resistivity at the center of the plume is weaker, only 14.8 Ωm. Based on this, M1 seems to provide the best result with respect to target depth and strength of the resistivity anomaly. This may be explained by M1 representing the real subsurface resistivity better, providing a better starting point for the inversions. M1 is therefore used as starting model further on in the inversion study.

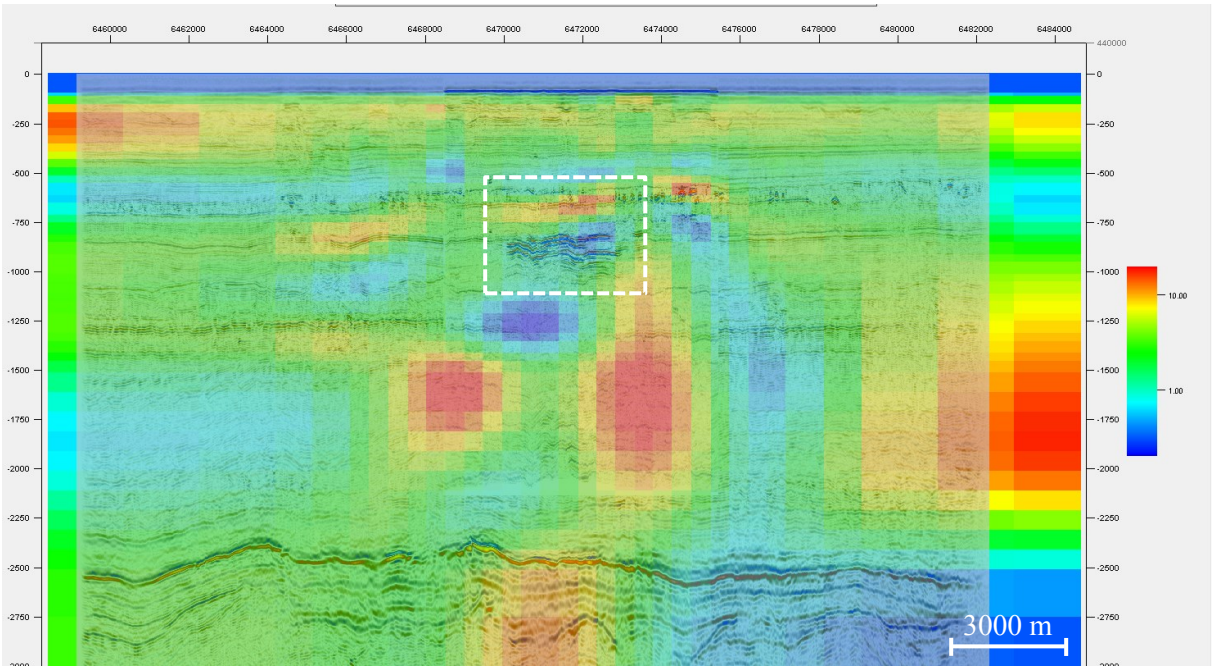

Figure 5.10: Vertical resistivity profile resulting from inversion of the CSEM dataset after removing data from seven closely spaced receivers, employing M2 as the initial model.

Offset range

For near offsets the guided mode generated by the CO_2 plume is masked by the dominating direct mode, so data from these offsets are not necessary to include in the inversions. The forward modeling study of a 0.25 Hz signal and a very simplified 1D model in section 4.2 suggested that the guided mode would start to dominate at an offset around 2000 m. However, since all the frequencies in the Sleipner dataset are higher, smaller minimum offsets should be included. Inversions for minimum offsets of both 1000 m and 1500 m were performed, and Figure 5.11 shows the inversion result when including data from a minimum offset of 1500 m instead of 1000 m. In this case the depth of the high-resistivity area representing the CO_2 plume in the resistivity profile seems to have improved, compared to in the inversion result where a minimum offset of 1000 m was employed (Figure 5.7). However, the response at the center of the plume is reduced to just below 11.5 Ωm, compared to 18.8 Ωm. Based on this, the data for offsets between 1000 m and 1500 m seem to carry significant information about the target, and therefore a minimum offset of 1000 m is employed for the inversions performed further on in this study.

Since information about the target seemed to be lost when a minimum offset of 1500 m was employed, larger minimum offsets were not tested.

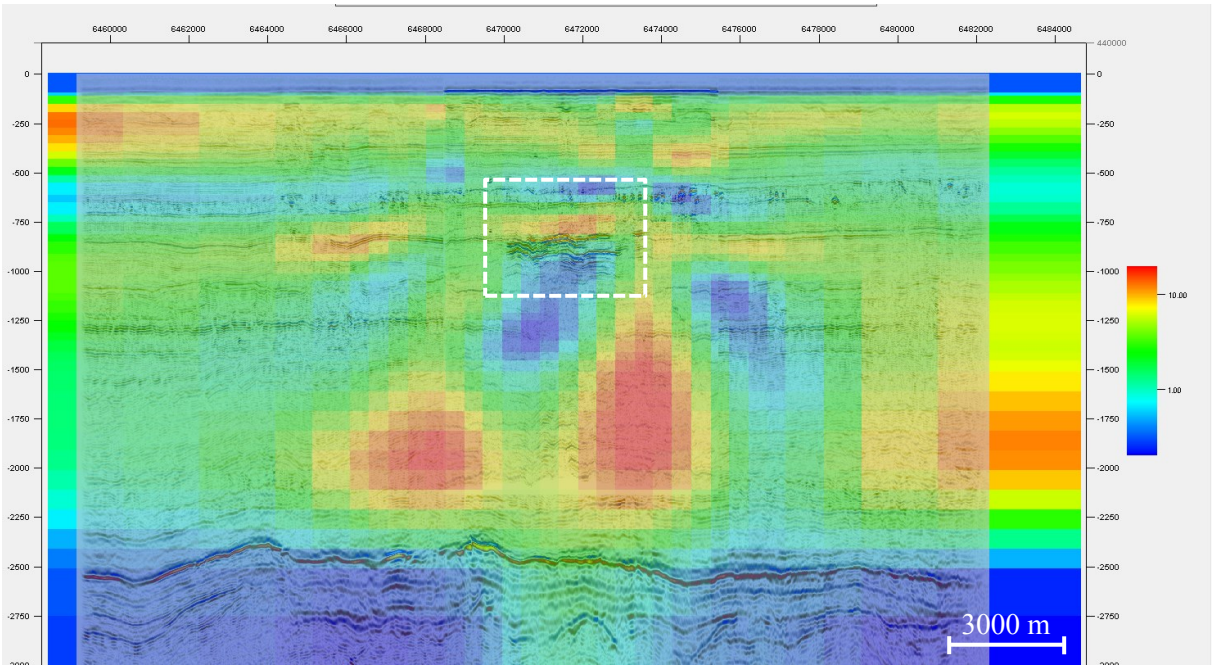

Figure 5.11: Vertical resistivity profile resulting from inversion of the CSEM dataset after removing data from seven closely spaced receivers, employing a minimum offset of 1500 m instead of 1000 m.

Due to the shallow water in the Sleipner area, the airwave might mask parts, or all, of the guided mode response from the CO_2 plume. This makes it difficult to decide the maximum offset to include in the inversions. The forward modeling study suggested that a maximum offset smaller than 10000 m should be sufficient for the Sleipner dataset, so inversions were performed for maximum offsets of 10000 m, 8000 m and 6000 m.

Figure 5.12 shows the inversion result when reducing the maximum offset data included in the inversion from 8000 m to 6000 m, and Figure 5.13 shows the inversion result when the maximum offset was increased to 10000 m. In both the 6000 m and 10000 m offset results, the location of the high-resistivity area representing the CO_2 plume is very similar compared to the 8000 m offset case in Figure 5.7. In the 6000 m offset result, the resistivity in the center of the plume is increased, to 19.2 Ωm, compared to 18.8 Ωm, while in the 10000 m offset result, it is reduced to 16.5 Ωm. This may be explained by the fact that for a 10000 m offset, more of the airwave response will be present in the data, masking the target response. For a 6000 m offset, less of this airwave dominated response is included in the inversion, and the guided mode response from the target represents a larger part of the total response.

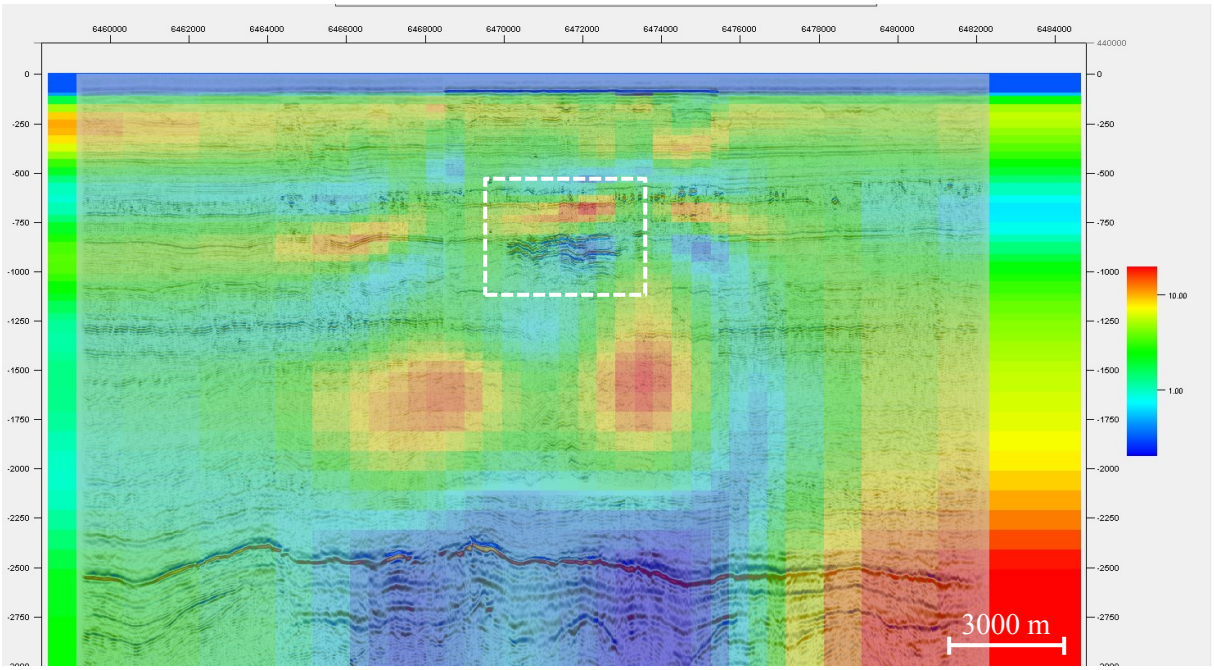

Figure 5.12: Vertical resistivity profile resulting from inversion of the CSEM dataset after removing data from seven closely spaced receivers, employing a maximum offset of 6000 m instead of 8000 m.

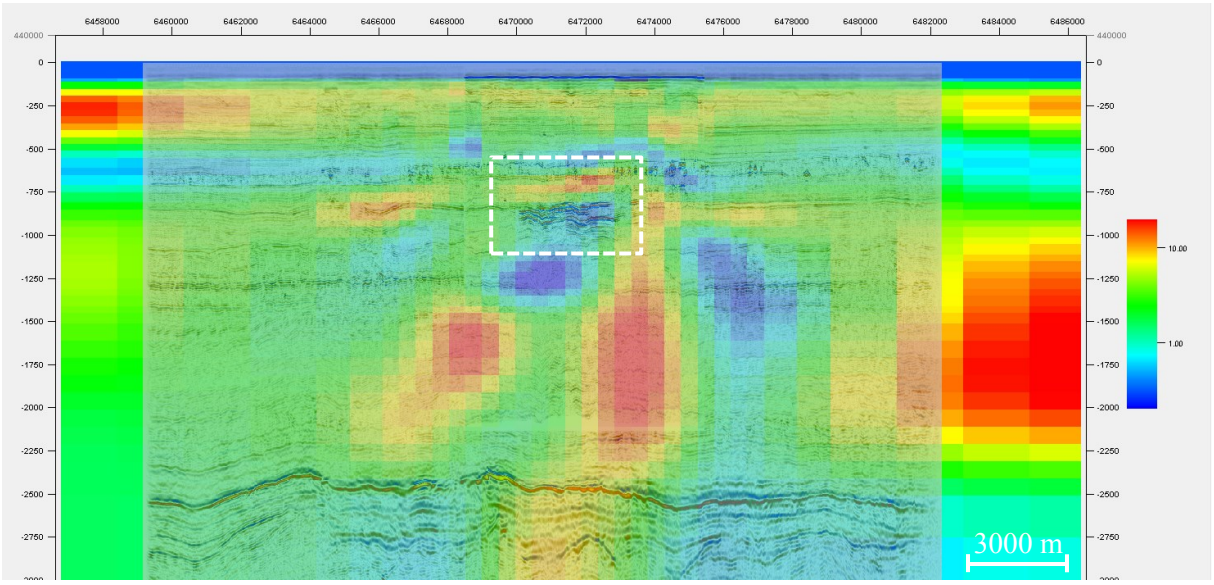

Figure 5.13: Vertical resistivity profile resulting from inversion of the CSEM dataset after removing data from seven closely spaced receivers, employing a maximum offset of 10000 m instead of 8000 m.

5.6 Filtering to remove pipeline effect

Figure 5.5 shows how the pipelines at seabed cross the survey line at six different places. There are in total nine pipelines, but only seven of them can be distinguished from the figure due to close spacing. The pipelines interfere with the CSEM signal, and represent one of the major challenges related to inverting and interpreting the data (Park et al., 2011; Park et al., 2013). By identifying the data that are

strongest influenced by the pipelines, these data can be filtered out, and hopefully the artefacts generated by the pipelines will be removed, or at least reduced, in the inversion result.

The pipeline effect on the data can be seen in the plot of AVO for each receiver along the towline in Figure 5.6. A drop in the magnitude of the electric field can be seen at some of the pipeline positions (along the red dotted lines), but mainly for the two pipelines to the northeast. The effect is also different for the different frequencies. Based on such plots alone it is difficult to determine what data to filter out to reduce the pipeline influence. One approach is to use the map of the seabed pipelines and filter out data from receivers positioned near the pipeline crossings, and this is attempted in section 5.6.1. Another is to analyze the data in more detail to try to identify the largest influenced data, which is attempted in section 5.6.2.

The dataset where data from the seven closely spaced receivers already have been removed was employed when filtering out data strongly influenced by pipelines. After the pipeline data had been filtered out inversions were performed for varying offset ranges, to check whether the optimal offset range might have changed when data from specified receivers were removed. For these datasets, the optimal minimum offset still proved to be 1000 m, while a maximum offset of 6000 m and 8000 m gave very similar results, with respect to the strength and location of the resistivity anomaly representing the CO_2 plume. For the deeper parts of the model, a larger maximum offset will give a more representative image, so the results where an offset range between 1000 m and 8000 m was employed will be presented. Inversions with both a priori model M1 and M2 were also performed. M1 proved to give the best result, also after the pipeline data was filtered out, and the results where M1 was defined as the initial model is therefore presented.

5.6.1 Pipeline data filtering based on pipeline locations

From the map of where the pipelines cross the CSEM survey line (Figure 5.5), the position of nine receivers, Rx003, Rx004, Rx005, Rx006, Rx014, Rx015, Rx018, Rx019 and Rx020 can be observed to be next to a pipeline crossing point. Also Rx022 seem to be located quite close to the northernmost pipeline crossing. This is also the case for Rx021, but data from this receiver was removed from the dataset when the closely spaced receiver data were filtered out. In the inversion result in Figure 5.14 data from the ten receivers listed above, located near seabed pipeline crossings, have been filtered out. In Figure 5.15 source points from approximately the same areas have also been removed, since these data also can be assumed to be influenced by the pipelines. The effect of the pipeline data filtering can be seen by comparing the results with Figure 5.7, where the same inversion setup parameters were employed. The location of the CO_2 plume is improved in both of the results, but the response of the center of the plume is reduced to 15.7 Ωm for the case when only receiver data was removed, and to 9.5

Ωm when the source points also were removed. However, artefacts presumably generated by the pipelines in the shallow parts of the profile, have been significantly reduced for the case where the source points also were removed, indicating that the filtering of the pipeline influence was successful.

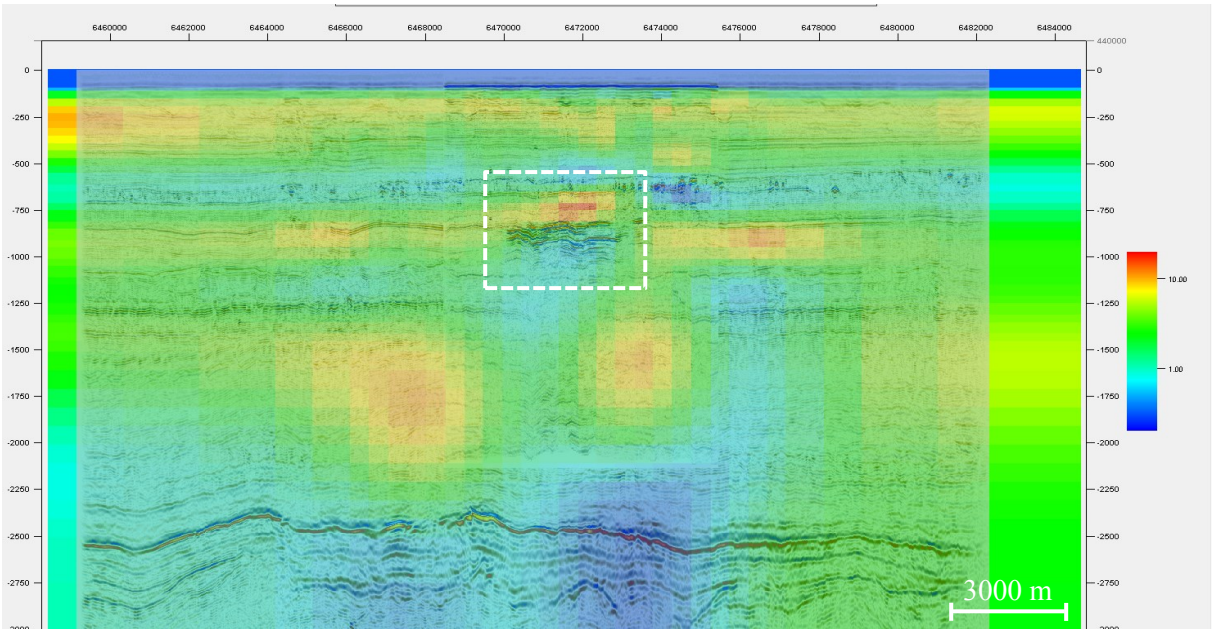

Figure 5.14: Vertical resistivity profile resulting from inversion of the CSEM dataset after removing data from seven closely spaced receivers, and additionally ten receivers positioned close to pipeline crossing points.

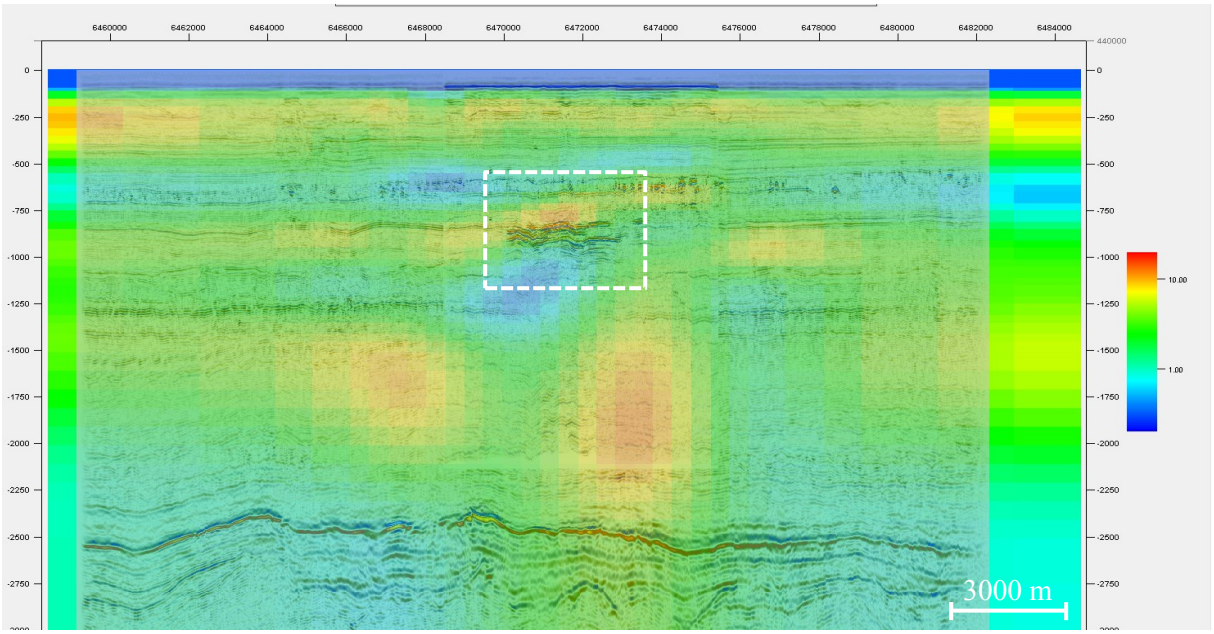

Figure 5.15: Vertical resistivity profile resulting from inversion of the CSEM dataset after removing data from seven closely spaced receivers, and additionally ten receivers positioned close to pipeline crossing points. Source points from the same areas have also been removed.

5.6.2 Pipeline filtering based on data analysis

The pipeline effect on the data is more evident when plotting the normalized magnitude with respect to common midpoint (CMP) position between source and receiver along the towline (x-axis), and half offset (y-axis). The half-offset gives an indication of the depth, and is therefore plotted along the vertical. Since no baseline CSEM survey without the pipelines exists, an average of the end receivers was used as reference data for the normalization. To avoid the effect of the CO_2 in the reference data, an average between Rx001 and Rx002 was used as reference for negative offsets, while an average between Rx026 and Rx027 was used for positive offsets. The magnitude of the response at each receiver was then divided by this background response, and the normalized result (minus 1) plotted for each frequency. The normalized response for the 0.5, 1 and 1.5 Hz signal can be seen in Figure 5.16, and the normalized 2, 2.5 and 7 Hz response in Figure 5.17

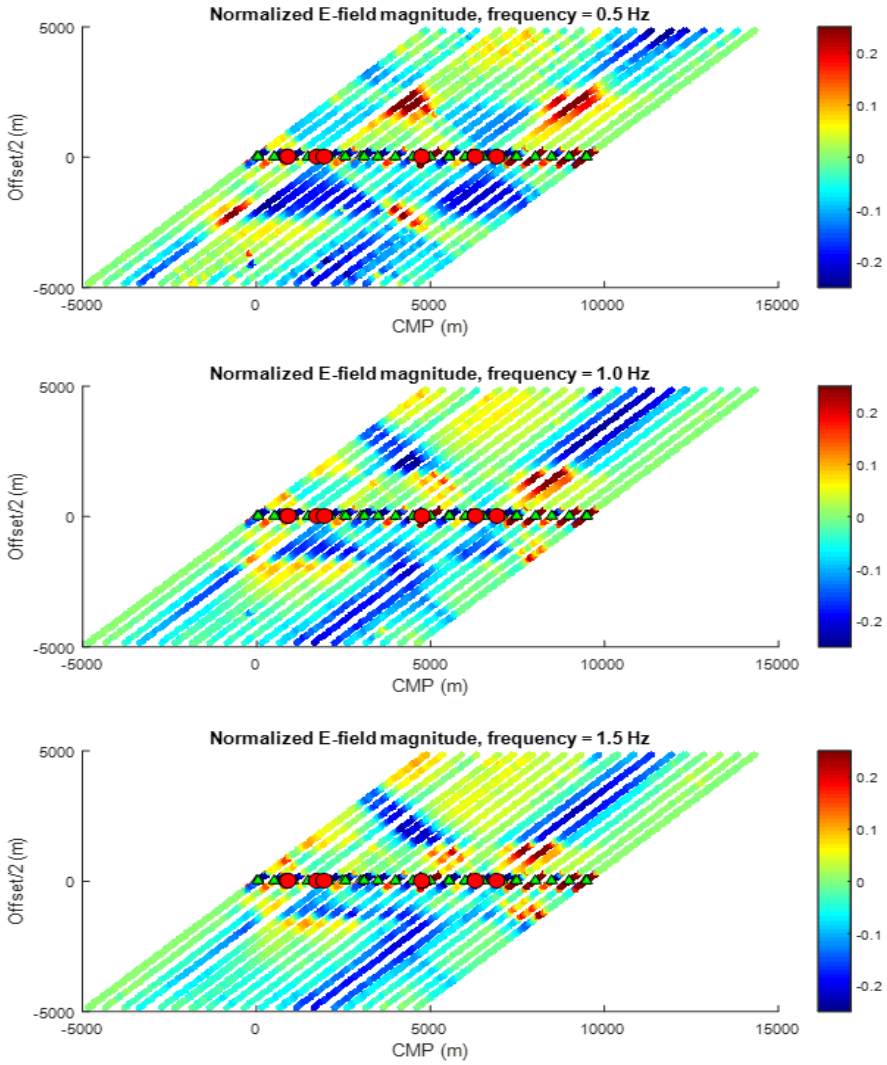

Figure 5.16: Normalized magnitude of the inline electric field (color scale) plotted as a function of CMP position along the towline, relative to Rx001 (x-axis), and half offset (y-axis), for the 0.5, 1 and 1.5 Hz response. Green triangles represent receiver positions, and red circles represent pipeline positions. In the plots, 1 have been subtracted from the normalized magnitude.

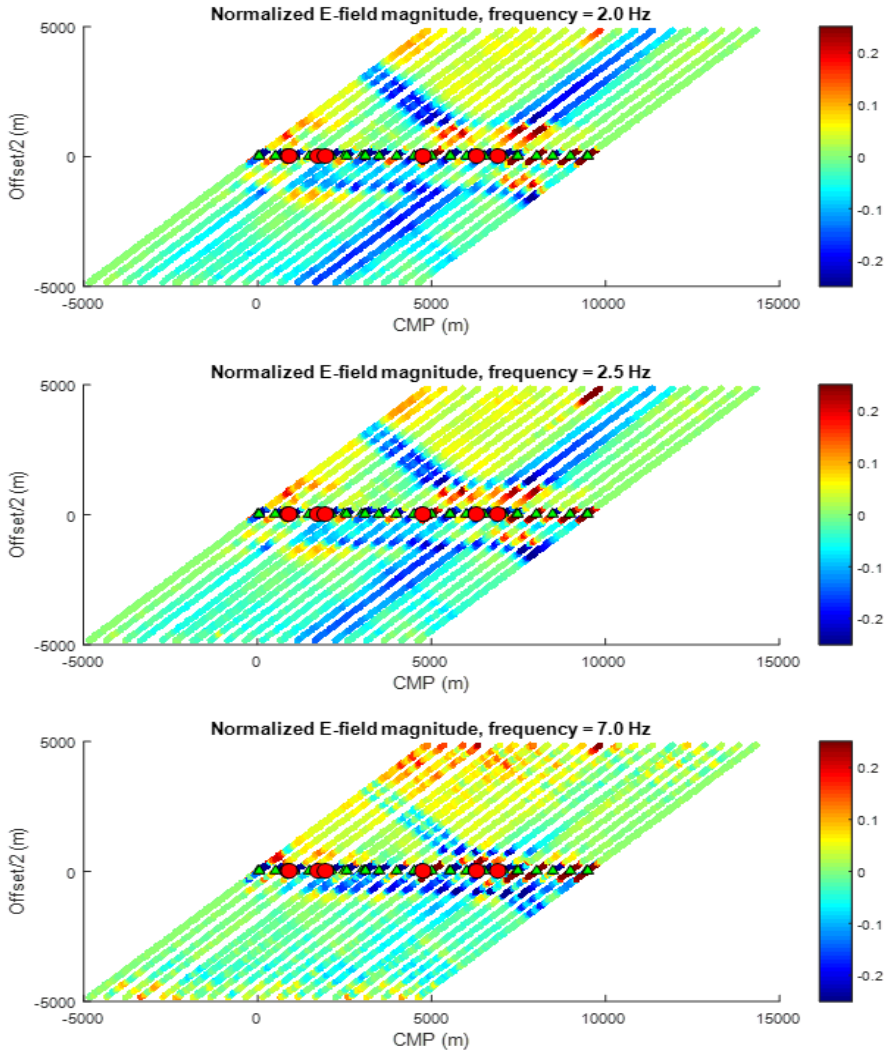

Figure 5.17: Normalized magnitude of the inline electric field (color scale) plotted as a function of CMP position along the towline, relative to Rx001 (x-axis), and half offset (y-axis), for the 2, 2.5 and 7 Hz response. Green triangles represent receiver positions, and red circles represent pipeline positions. In the plots, 1 have been subtracted from the normalized magnitude.

The plots of the normalized magnitude show two more or less distinct negative anomalies for all six frequencies, each in the form of two diagonals crossing at 90 degrees at zero half offset. These anomalies seem to be generated by the pipelines located at the crossing points of the diagonals, with locations around CMP 1900 m and 6600 m. This theory is supported by Park et al. (2011), where normalized synthetic CSEM data show similar tendencies when pipelines were included in the forward modeling. This also corresponds well to the meeting points of the two sets of diagonal anomalies observed in the single frequency inversion results described in section 5.5, indicating that these anomalies are generated by the pipelines at seabed. The influence from the pipelines thus seem to be largest in these two areas, corresponding to where the pipelines cross the profile between Rx005 and Rx006, and between Rx018 and Rx020. These pipelines generally have a larger diameter than the rest, which can explain their larger influence on the CSEM data. The two northernmost pipelines, crossing between Rx018 and Rx020, have

the largest effect on the data, with the largest anomalies in the normalized magnitude for all the frequencies. This may be due to the fact that they cross the towline with the smallest angle, and thus the inline electric field is more sensitive to these.

Based on this more systematic method of identifying the data strongly affected by pipelines, data from Rx005, Rx006, Rx018, Rx019 and Rx020, which are the receivers next to the pipelines with the largest influence on the data, were filtered out. Figure 5.18 shows the inversion result when data from these five receivers were removed to reduce the pipeline influence, instead of data from the ten receivers presented in the previous section. Figure 5.19 shows the inversion result when source point data also were removed from the same areas. The location of the CO_2 plume is improved in both of these results as well, and the response of the center of the plume is reduced. For the case when only the receiver data have been removed, the resistivity is around 15.4 Ωm, but is further reduced to 10.1 Ωm when the source points also have been removed. Also in this case, artefacts presumably generated by pipelines in the shallow parts of the model are significantly reduced for the case when the source points have been removed (Figure 5.19), indicating that the pipeline filtering was just as successful when only filtering out data from the five most strongly influenced receivers and the corresponding source points.

The results presented in this and the previous sections shows that it is unnecessary to filter out data from all the ten receivers located close to the pipeline crossing points to reduce the pipeline influence in the data. By removing data from the five receivers next to the pipelines generating the largest anomalies in the nAVO plots, approximately the same result was obtained, and the influence from the pipelines seem to be reduced to the same degree in both cases. However, the resistivity of the CO_2 plume is also reduced, most likely because some of the receivers where the data was filtered out, were located above the CO_2 plume. Since the data filtering seemed to remove the artefacts generated by the pipelines successfully, as well as improving the vertical position of the CO_2 anomaly, the dataset where data from the five receivers most strongly influenced by the pipelines, together with source points from the same areas were filtered out, is employed in the proceeding of the inversion study.

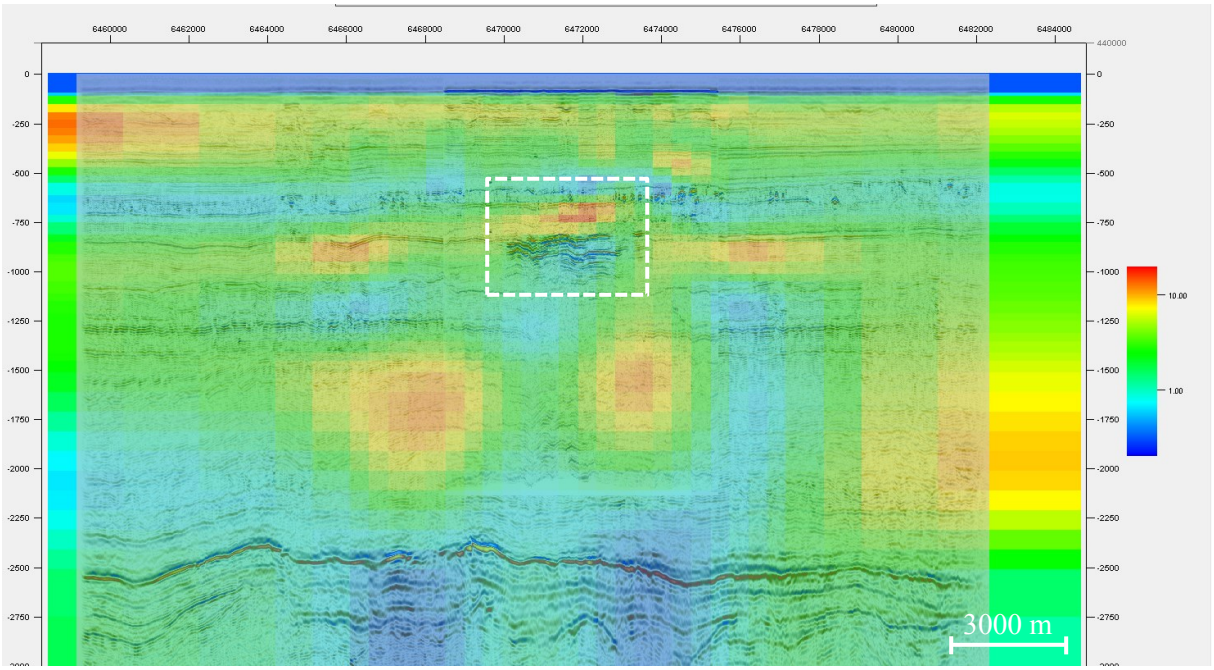

Figure 5.18: Vertical resistivity profile resulting from inversion of the CSEM dataset after removing data from seven closely spaced receivers, and additionally five receivers positioned close to the crossing points of the pipelines with the strongest influence on the data.

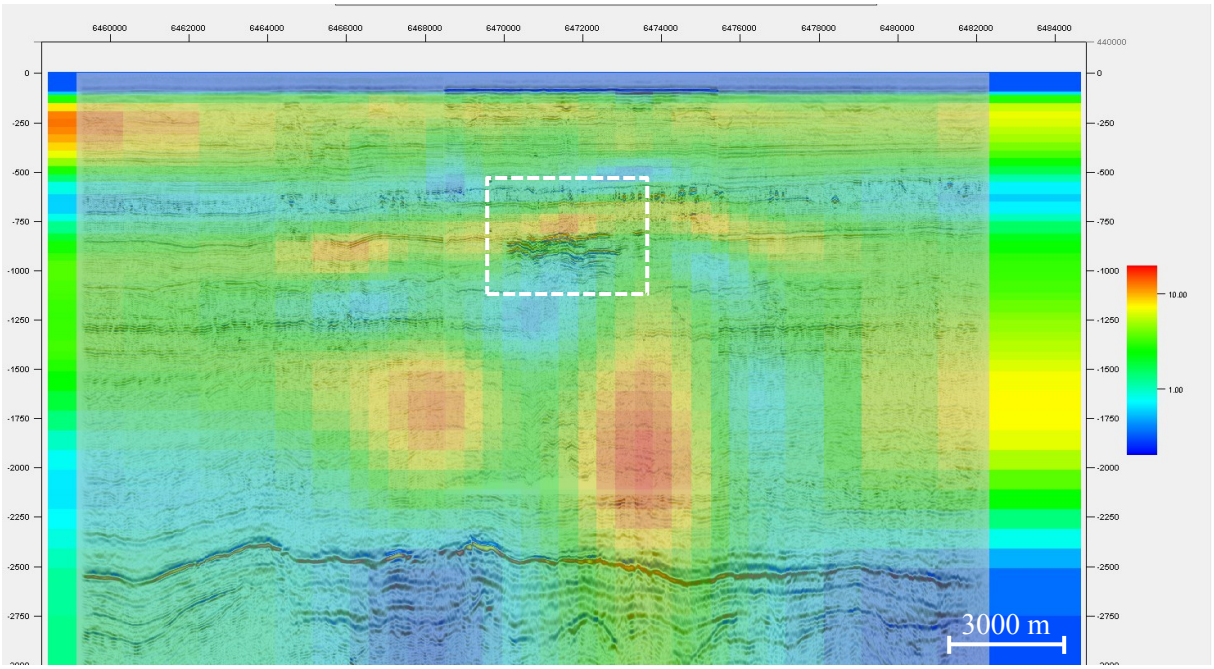

Figure 5.19: Vertical resistivity profile resulting from inversion of the CSEM dataset after removing data from seven closely spaced receivers, and additionally five receivers positioned close to the crossing points of the pipelines with the strongest influence on the data. Source points from the same areas have also been removed.

5.6.3 Source point interpolation

When filtering out source points from specific areas, in the process of filtering out pipeline influenced data, data from these points will be missing for each of the remaining receivers. In order to attempt to recover these data points, they could be interpolated between the remaining data points. If such an interpolation is successful, it can provide data from these areas without the influence from the pipelines, and thus maybe improve the inversion result. An attempt to do this was performed using the *spline* function in Matlab, for the dataset where data from the five receivers with the largest pipeline influence, and source points from the same areas, were filtered out. Figure 5.20 shows the vertical resistivity model resulting from the inversion of this interpolated dataset, with the same inversion setup as in Figure 5.19. The attempt to improve the inversion result failed, as the location of the high-resistivity area representing the CO_2 plume was significantly worsened. However, the resistivity of the center of the anomaly increased to 16.6 Ωm, and maybe a better interpolation of the data could have given an improved inversion result.

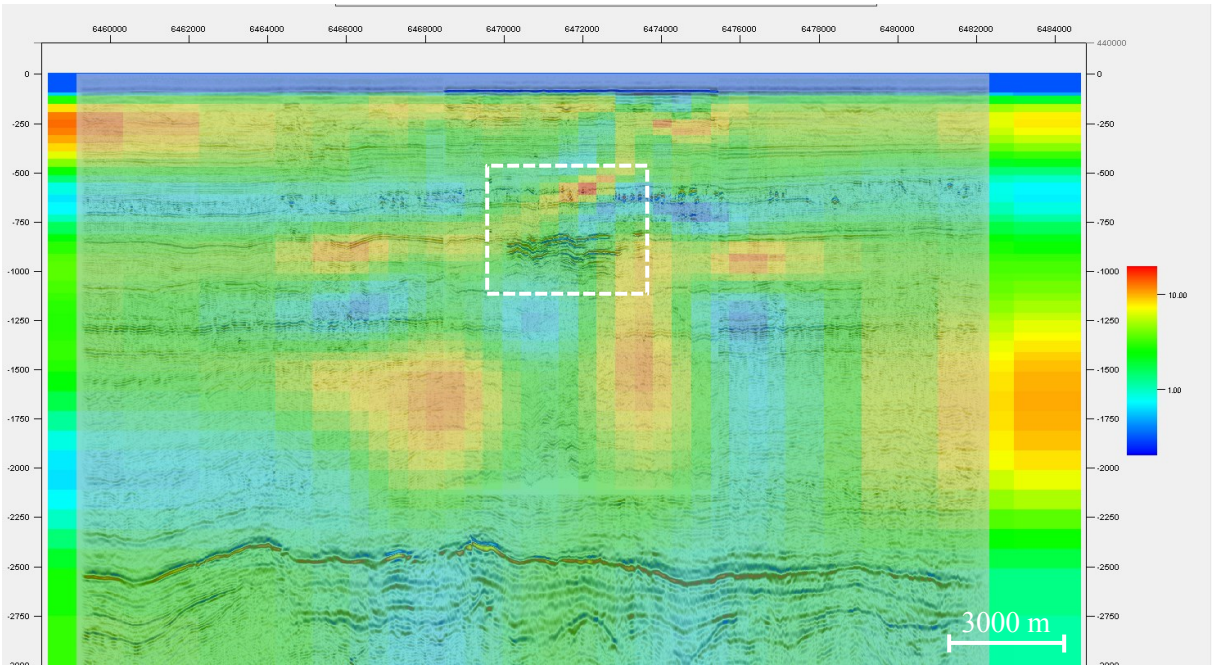

Figure 5.20: Vertical resistivity profile resulting from inversion of the CSEM dataset after removing data from seven closely spaced receivers, and additionally five receivers positioned close to the crossing points of the pipelines with the strongest influence on the data. Source points from the same areas have also been removed, and new source point data interpolated between the remaining data points.

5.7 Varying inversion setup to improve inversion result

After addressing the challenges related to the pipeline influence, the idea is to further improve the inversion result by trying to solve challenges related to the shallow location and weak resistivity anomaly of the CO_2 plume. The inversion result depends on the inversion setup, so different inversion setup variations were performed in an attempt to improve the inversion result. This includes varying the data error estimates, including the water layer in the inversion, moving the source positions to a fixed depth, and applying a denser inversion grid in the area of the CO_2 plume. An attempt was also made to reduce the data amount for the calculations, by only including three well-spaced frequencies, instead of all six. The inversions were carried out with the dataset where data from the five receivers strongly influenced by pipelines was filtered out, together with the source point data from the same area, as a starting point for the inversion setup variations. Consequently, the resistivity models resulting from this dataset, presented in Figure 5.19, was used for comparison in the evaluation of the results presented in this section.

5.7.1 Data error estimate variations

In none of the inversions presented so far the RMS misfit reached 1, meaning that the measured and modeled data was not fitted within the range of the data error estimates. Figure 5.21 shows the magnitude (left window) and phase (right window) of the recorded 0.5 Hz signal from Rx013, plotted with respect to offset, for the dataset where the pipeline influenced data from five receivers, and source points, were filtered out. The solid line represents the measured data, while the dashed line represents the modeled data. The missing data points at offsets between -1600 and -2800 m is due to the source points removed from the area around Rx005 and Rx006. From the figure it seems that the modeled magnitude data fits very well with the measured data, while the difference is larger for the phase. To have a closer look at this, separate inversions for magnitude and phase were conducted.

When inverting only for magnitude, the cost function was still converging when the misfit reached 1. This indicates an overestimation of the magnitude error, as the cost function has not yet flattened out and stabilized around a solution. It is still converging towards a better fitting of the data. This inversion was therefore rerun with the desired misfit specified to 0.7. The inversions result when inverting for magnitude and phase separately can be seen in Figure 5.22 and Figure 5.23, respectively.

Based on the results it seems like the phase carries most of the information about the subsurface, as inverting for magnitude alone provides much less resistivity variations in the subsurface model. No resistivity anomaly representing the CO_2 plume can be detected in the magnitude inversion result, while the phase inversion result is very similar to the inversion result when both magnitude and phase data

were included in the inversion (Figure 5.19). The location of the plume is more or less identical, and the resistivity of the center of the plume anomaly is only slightly reduced, from 10.1 Ωm, to 9.5 Ωm.

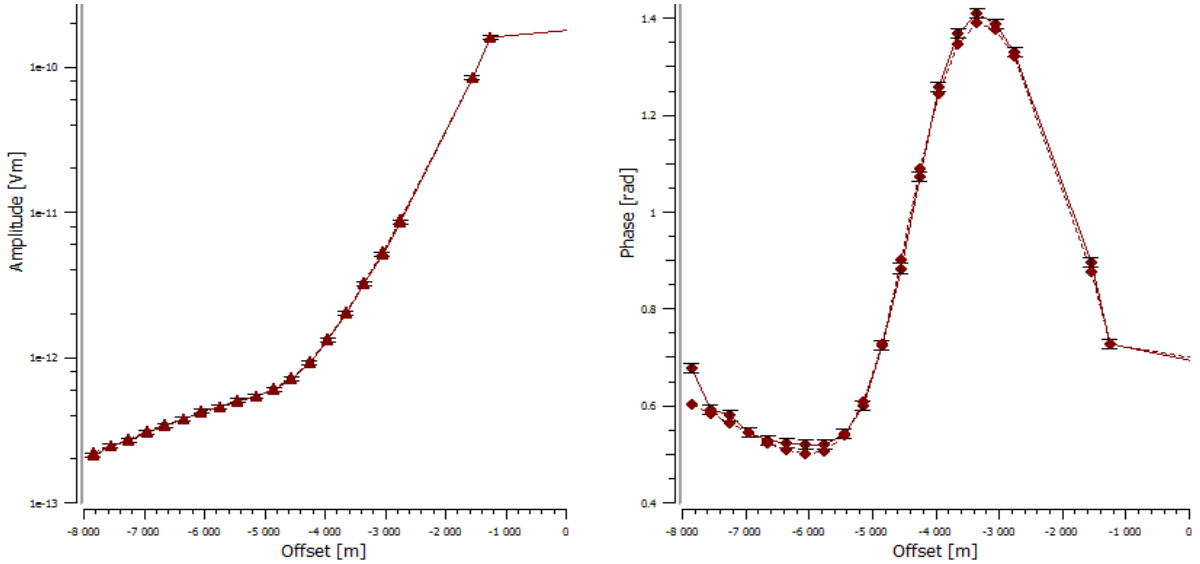

Figure 5.21: Modeled (dashed line) and measured (solid line) AVO (left) and PVO (right) for the 0.5 Hz signal at Rx013, for negative offsets. The modeled data is from the inversion result where pipeline data was filtered out.

The fact that the misfit function stabilizes around values below one for the magnitude data, and above one for the phase data, indicates that the data error estimates could be decreased for the magnitude data, and increased for the phase data. In the previous inversions the error estimates were set to 3.0 % for the magnitude and 0.01 radians for the phase, and two different inversions setups were employed to study the effect of changing these. For the first case, the values were set to 2.0 % for the magnitude and 0.02 radians for the phase, and for the second case, to 1.0 % for the magnitude and 0.05 radians for the phase.

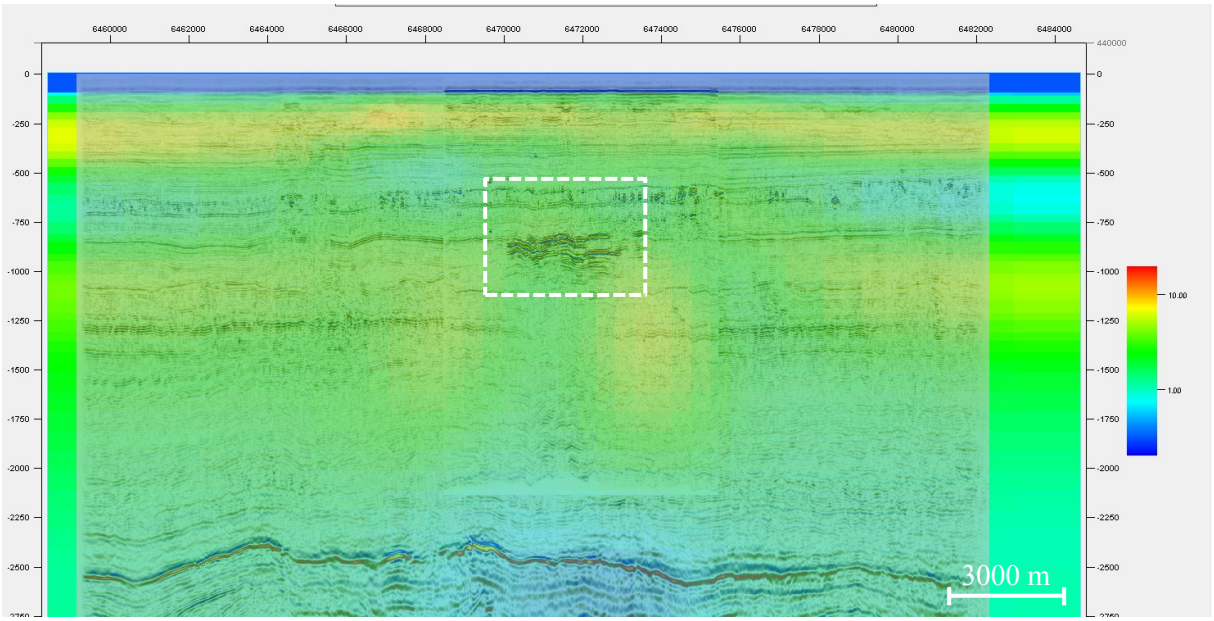

Figure 5.22: Vertical resistivity profile when only inverting for magnitude data, with desired misfit set to 0.7.

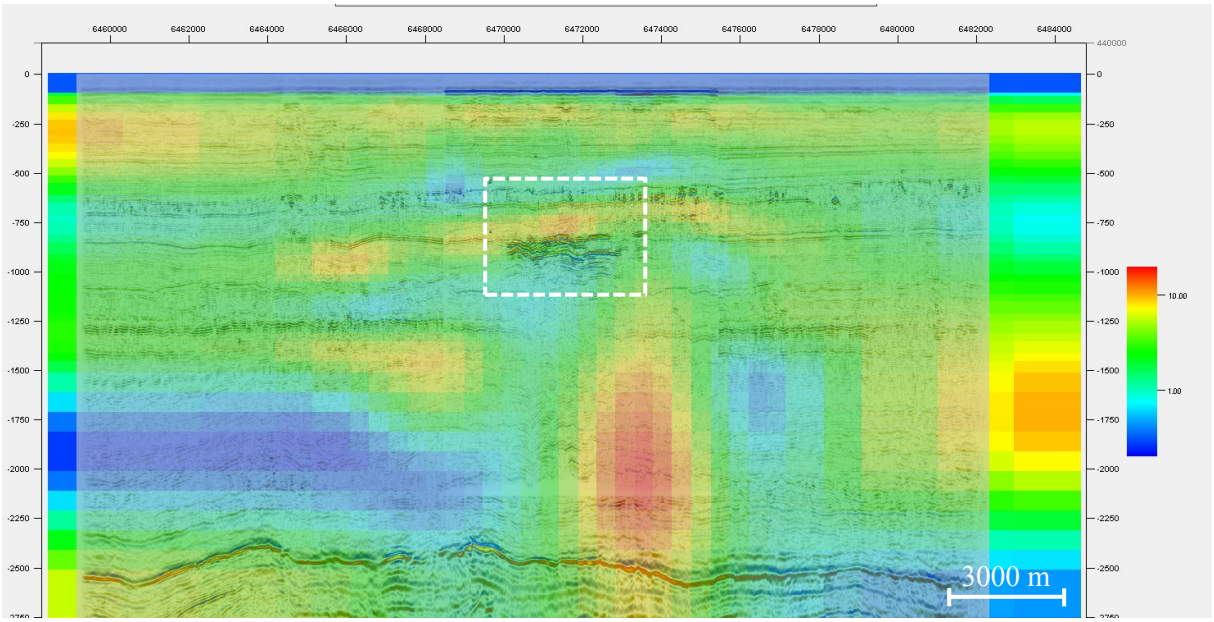

Figure 5.23: Vertical resistivity profile when only inverting for phase data, with desired misfit set to 1.

Figure 5.24 shows the inversion result from the first case, and the results from the second case is presented in Figure 5.25. In both results the strength of the resistivity anomaly is reduced compared to when the original error estimates were employed (Figure 5.19), to 7.6 Ωm for the first case, and 8.9 Ωm for the second case. The vertical location of the resistivity anomaly generated by the CO_2 has improved significantly for the second case, but the horizontal location has moved to the right of the plume defined by the seismic, and is significantly worsened. The best result therefore seem to be obtained with a data error estimate of 3 % for the magnitude and 0.01 radians for the phase, and these values are applied for the rest of the inversions performed in this study.

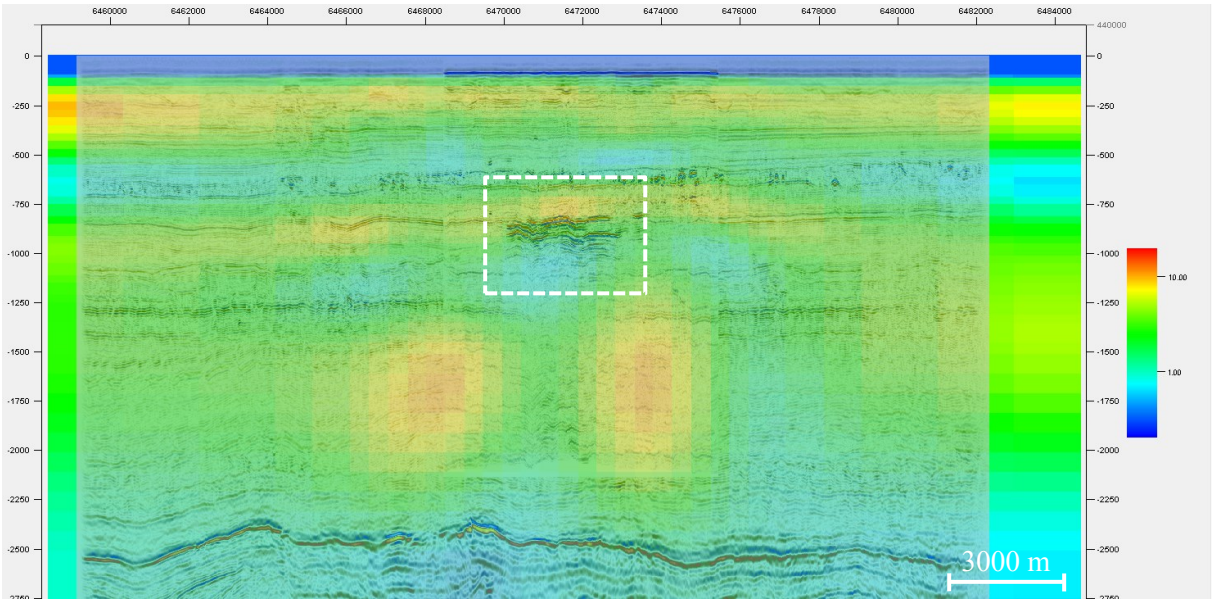

Figure 5.24: Vertical resistivity profile resulting from the inversion where the data error estimate was set to 2 % for the magnitude data, and 0.02 radians for the phase data.

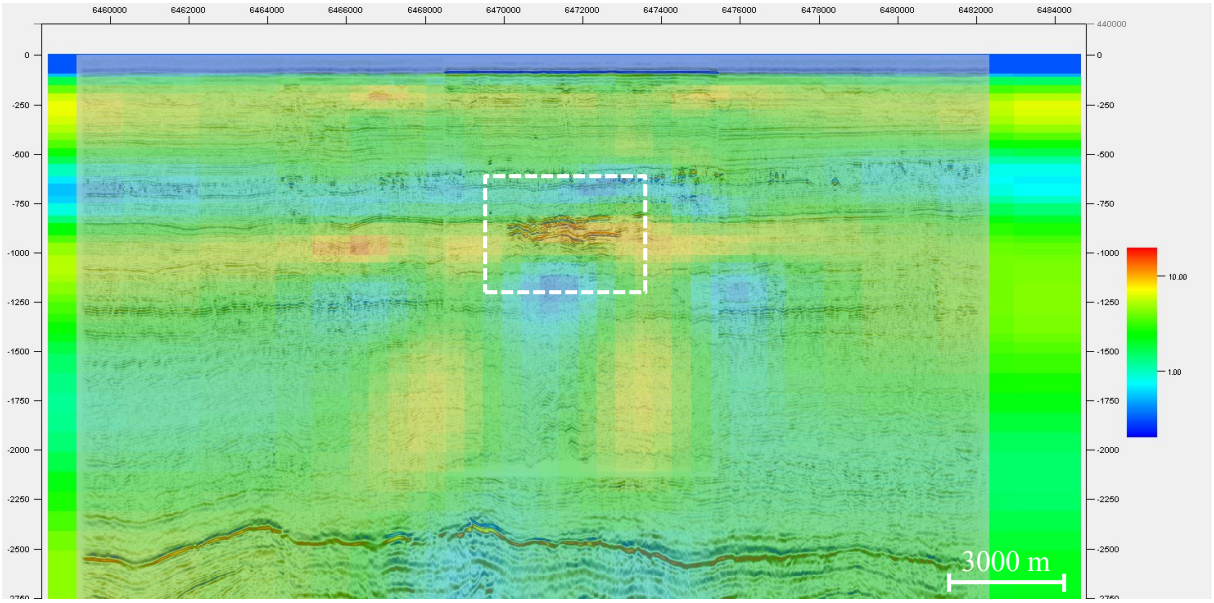

Figure 5.25: Vertical resistivity profile resulting from the inversion where the data error estimate was set to 1 % for the magnitude data, and 0.05 radians for the phase data.

5.7.2 Fixed source point depth

Taking a closer look at the source positions in the dataset, they seem to be quite irregular (Figure 5.26). During the acquisition of the survey, the source should be towed at a more or less constant depth, but in the Sleipner dataset the vertical source position vary from -50 to -64 m. A 14 m variation might not be very much when the horizontal stretch is around 30 km, and the vertical axis in Figure 5.26 is highly exaggerated compared to the horizontal. However, to determine if there might be something wrong with the source positions, and if so, how it affects the CSEM data, an inversion dataset where all the source positions were relocated at the average depth of -57 m was created (Figure 5.27). The resulting resistivity model is presented in Figure 5.28, and is more or less identical to the model resulting from the inversion of the same dataset without the relocation of the source points (Figure 5.19). The original source positions are therefore kept for the following inversions.

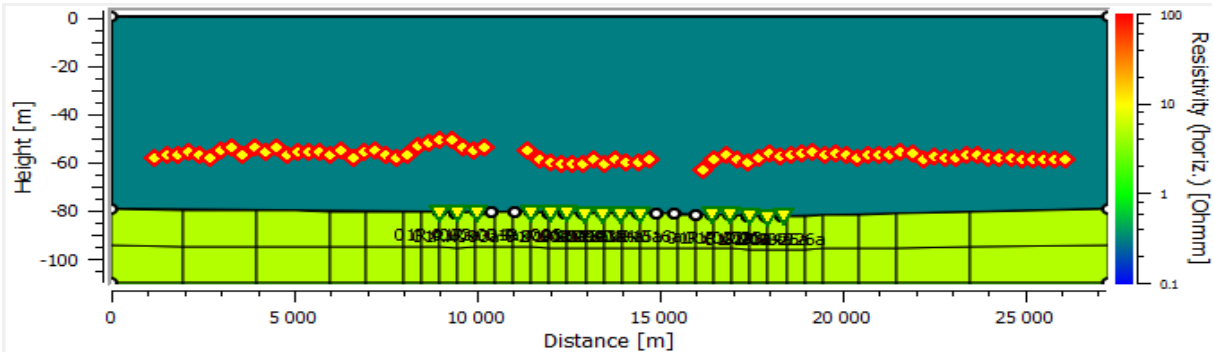

Figure 5.26: Original source point positions in the 2008 CSEM dataset from Sleipner where data from five receivers and source points strongly influenced by pipelines have been removed, resampled at 300 m.

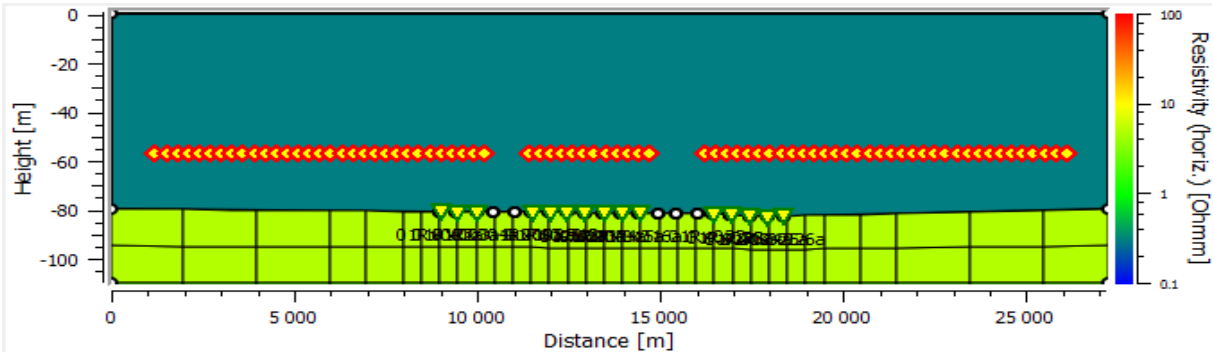

Figure 5.27: Source point positions at a constant depth of -57 m, resampled at 300 m.

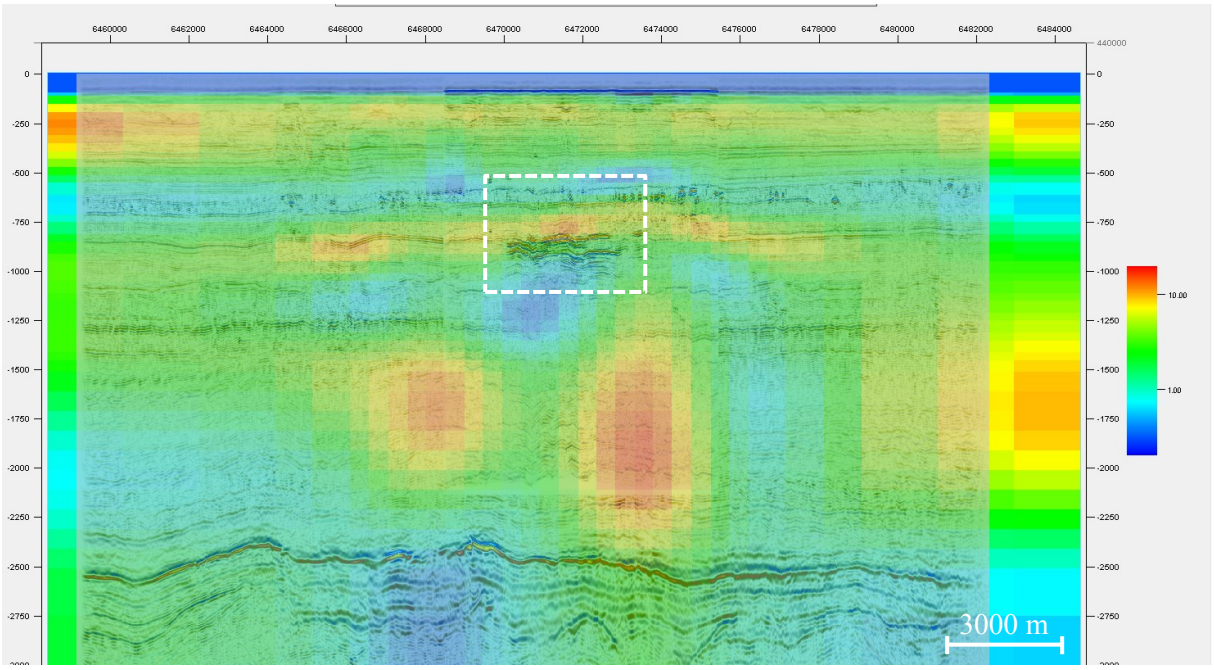

Figure 5.28: Vertical resistivity profile resulting from the inversion of the dataset where data from five receivers and source points strongly influenced by pipelines were filtered out, with source points relocated at -57 m.

5.7.3 Including the water layer

Until now, the seawater layer has been modeled as a homogeneous layer of 0.3125 Ωm resistivity, and excluded from the inversions. However, if this resistivity value doesn't represent the real water resistivity well, it might lead to errors in the modeled wave field in the inversions. If the real water resistivity is higher, the modeled signal would be more attenuated through the water than the real signal, while if the real resistivity is lower, the modeled signal would be less attenuated. To get an indication of the water resistivity, inversions should be performed where the water layer also is included in the inversions.

Resistivity variations will, to a higher or lower degree, always be present in the water layer, affecting the CSEM signal as it propagates through the water. These variations are mainly caused by temperature and salinity variations, but the mechanisms are quite complicated. Information about these mechanisms

is presented by e.g. Luz & Régis (2009) and Paramor et al. (2009). Layers of different temperature and salinity, which affects the resistivity of the water, often form in the water column, especially during the warmer months of the year. The top layer warms, and less winds and fewer storms cause less mixing with the lower layer. The near-surface layer has a higher temperature, and almost no temperature variation within the layer because of a high degree of internal mixing. The thickness of this mixed layer vary with season, and below this layer, the temperature decreases with depth. However, many areas in the North Sea are characterized by shallow water and strong tidal currents that keep the whole water column mixed. According to Paramor et al. (2009) the mean surface temperature when the CSEM dataset was acquired in September 2008 was 14-15 °C (Figure 5.29). Skjoldal (2007) modeled the seabed temperature in September the year before to between 6 and 8 °C (Figure 5.29), so the temperature can be assumed to have been around the same in 2008. This indicates a warmer upper layer in the Sleipner area. The salinity of seawater is normally around 3.5 %, but this can vary a lot near the surface and in bays and fjords with fresh water supply from rivers. The Sleipner area is located far from the coast, so a relatively low freshwater influx can be assumed, except for maybe at the surface.

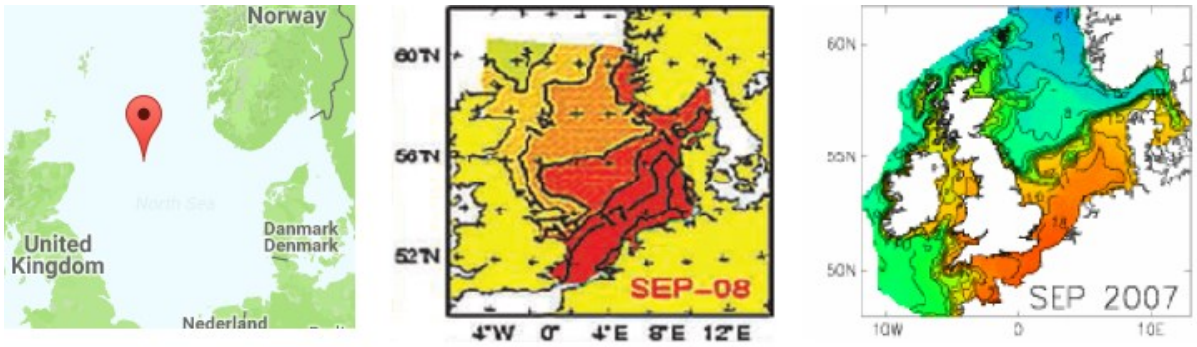

Figure 5.29: From left; the location of the Sleipner field (Global CCS Institute, 2016b); measured surface temperature in the North Sea in September 2008 (Paramor, et al., 2009); modeled seabed temperature in the North Sea in September 2007 (Skjoldal, 2007).

The effect on resistivity when changing parameters such as temperature and salinity can be found in e.g. Gelius (2016), who describes how increasing temperature and salinity leads to decreased resistivity. Higher temperatures in the upper layer, together with pretty stable salinity, makes it reasonable to assume lower resistivity in the upper layer. On the other hand, the water is pretty shallow, and it may be sufficient to model it as one layer. Based on these considerations, different inversions were performed where the water layer(s) also were included in the inversions, both as one layer and two layers. For the one-layered water inversion, the water layer was defined as homogeneous, with an initial horizontal resistivity of 0.3 Ωm. The resistivity was restricted between 0.2 and 0.5 Ωm, since values outside this range seem unlikely. For the two-layered water inversion, the water layer was divided into two different layers, with the boundary at -20 m. The initial parameters were the same as for the one-layered water model. The inversions were rather unsuccessful in terms of the resulting resistivity model, which are

presented in Figure 5.30 (one-layered water) and Figure 5.31 (two-layered water). The resistivity anomaly of the CO_2 plume is rather weak in both of the resistivity models, and is located deeper and more to the right than in the background seismic. However, one interesting observation can be made from the one-layered water model; the horizontal water resistivity in the inversion result was around 0.27 Ωm, significantly lower than 0.3125 Ωm used in the previous inversions. On the other hand, this water resistivity seem to mask some of the CO_2 anomaly, and might not be of importance.

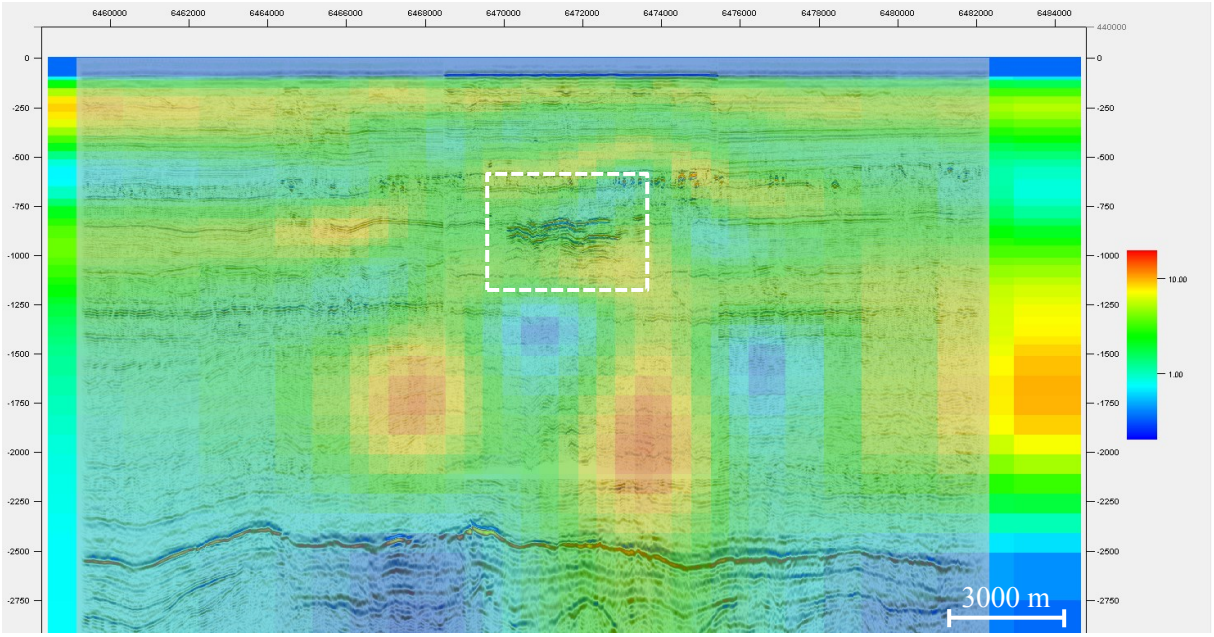

Figure 5.30: Vertical resistivity profile resulting from the inversion where the water, modeled as one layer, also was inverted for.

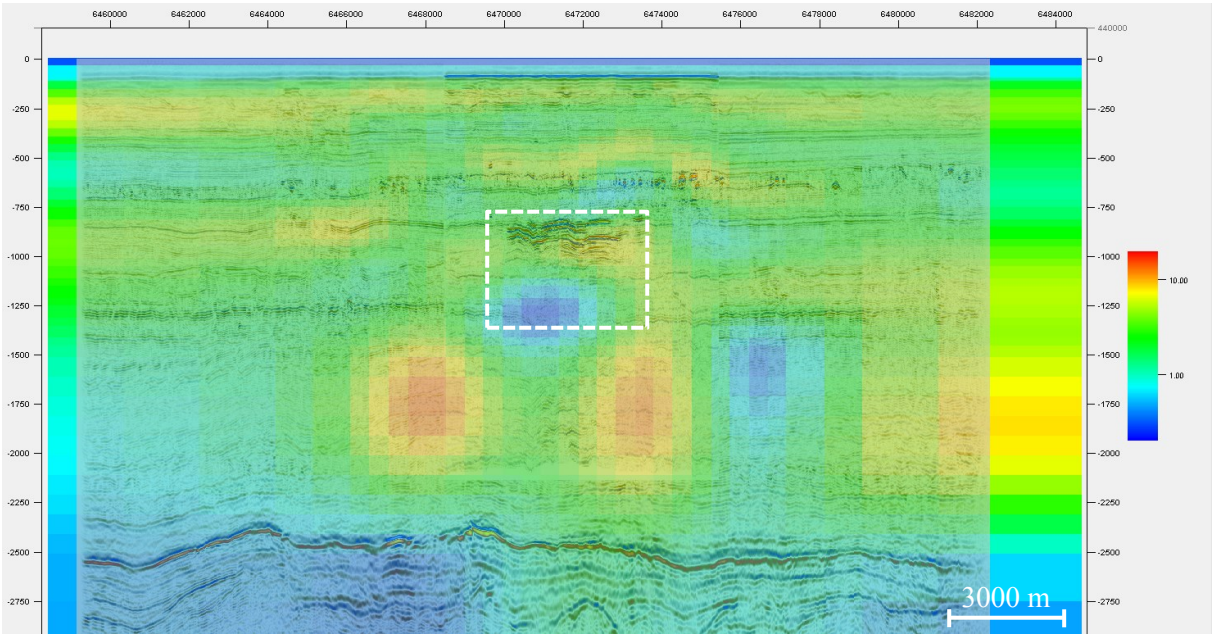

Figure 5.31: Vertical resistivity profile resulting from the inversion where the water, modeled as two layers, also was inverted for.

5.7.4 Reducing the number of frequencies

The results from the single frequency inversions presented in section 5.5 showed that inverting only for single frequencies did not result in satisfying resistivity models of the subsurface. This doesn't necessarily mean that all the six available frequencies need to be included in the inversions to obtain a representative resistivity image. Inversions for combinations of three different frequencies were therefore performed. Due to the different sensitivities of the different frequencies, the idea was to include one of the lower frequencies (0.5 or 1.0 Hz), one of the middle frequencies (1.5, 2 or 2.5 Hz), and the highest frequency (7 Hz). The inversion result when frequencies of 0.5, 2 and 7 Hz was included in the inversion, is presented in Figure 5.32. The results of other frequency combinations gave similar results; some with improved vertical location of the CO_2 anomaly, but in all the results the anomaly was rather weak and poorly defined horizontally. The conclusion from this is that all the six frequencies should be included in the inversion to obtain the best resistivity image.

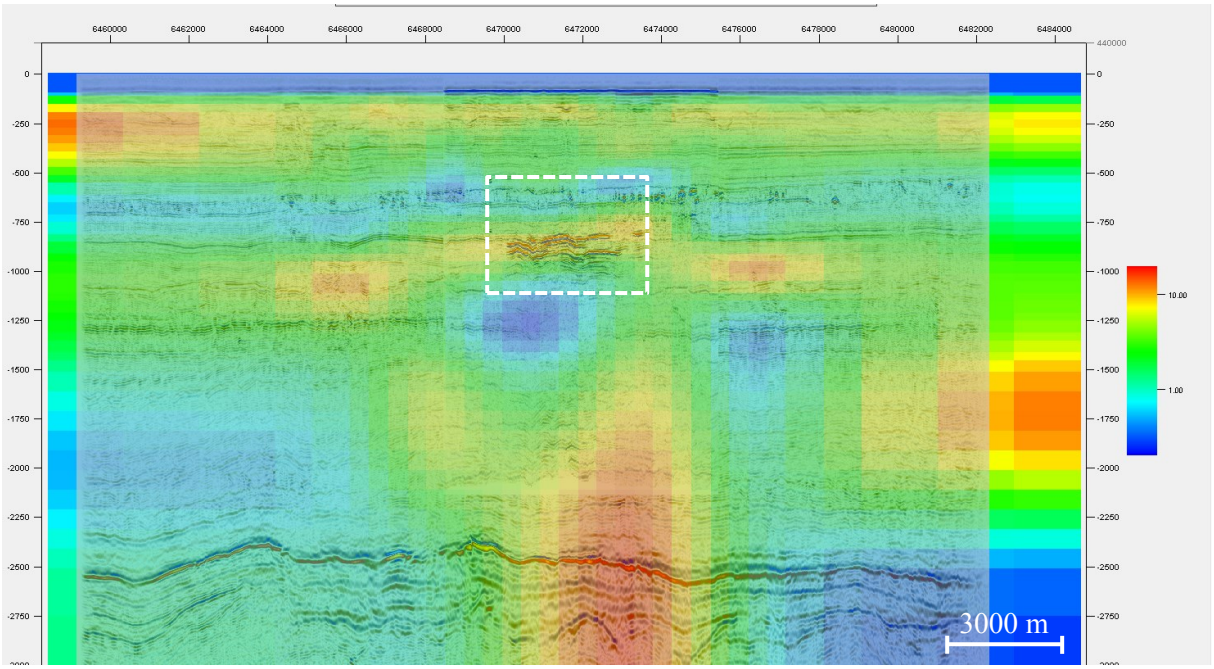

Figure 5.32: Vertical resistivity profile resulting from the inversion of data of three well-spaced frequencies; 0.5, 2 and 7 Hz.

5.7.5 Grid density

So far, the best inversion result was obtained when inverting the dataset where data from the seven closely spaced receivers, and additionally five receivers and source points strongly influenced by the pipelines, were removed, for offsets between 1000 and 8000 m, using M1 as the initial model and Grid 2 in the inversion setup (Figure 5.19). In another attempt to improve the response of the CO_2 plume in the resistivity model, a denser grid around the area of the plume was employed for this dataset. Since a

denser grid requires more calculations and increases the time of each iteration in the inversion, this was done after the other parameters had been optimized. Grid 3, where the area of the CO_2 plume is more densely gridded, was employed for this inversion.

The resistivity model resulting from the inversion is presented in Figure 5.33, and shows a significant improvement of the strength of the CO_2 resistivity anomaly, with 18.4 Ωm in the center of the anomaly, as well as a slightly improved extent and location with respect to the background seismic. The improved result may be explained by the increased resolution of the plume, resolving smaller areas of high resistivity, instead of averaging it over larger areas. Since the strength of the CO_2 anomaly has increased to around the same value as before the pipeline data was filtered out, while the pipeline influence is strongly reduced due to the pipeline data filtering, and the extent of the anomaly has improved, this is the best inversion result obtained so far in the study.

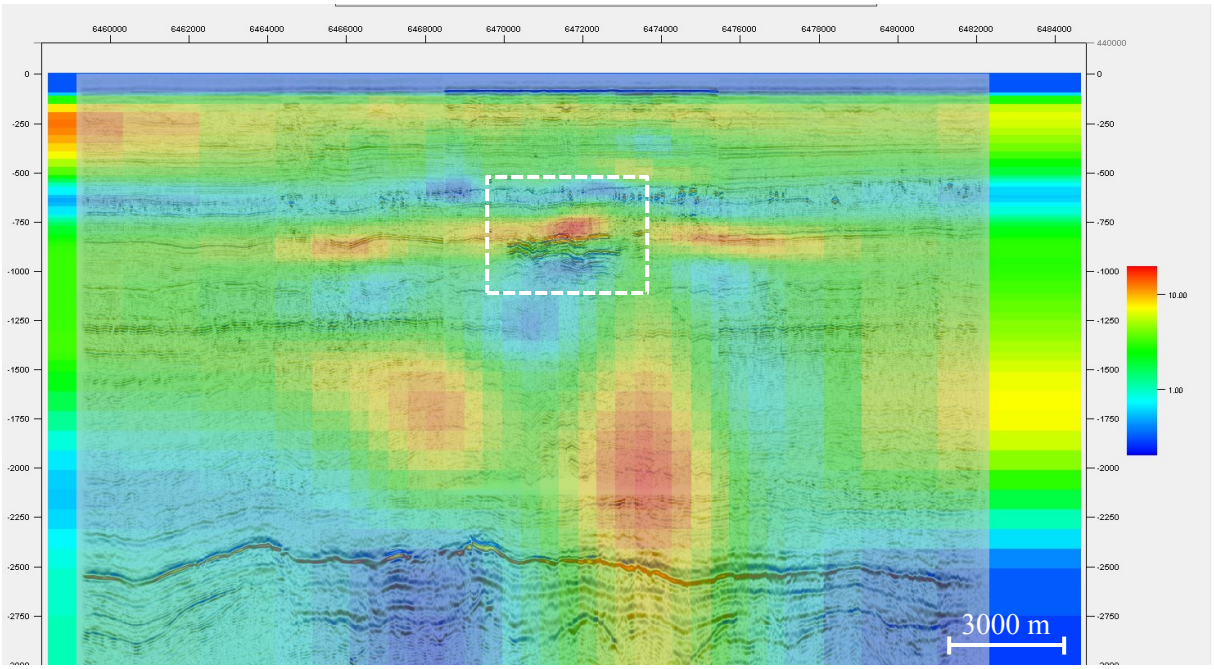

Figure 5.33: Vertical resistivity profile resulting from the inversion of the dataset where data from seven closely spaced receivers, and pipeline influenced data from five additional receivers and corresponding source points were filtered out. The denser Grid 3 was applied, together with an offset range of 1000 to 8000 m, and M1.

5.8 Constrained inversion

To try to improve the location and response of the CO_2 plume even further, an inversion constrained to the layer of the CO_2 plume were carried out. In the constrained inversion only the layer containing the CO_2 plume was inverted for, while the resistivity in the rest of the model were fixed. For this inversion it would be advantageous to have a baseline survey, and then use the inversion result from this background response as the fixed resistivity for the rest of the model in the constrained inversion. Since

a baseline survey was not acquired over the Sleipner area, the resistivity values from a previous inversion result had to be employed instead. This will most likely generate a less correct response compared to if a baseline model was used, since the presence of the CO_2 plume probably also affects other parts of the inversion result. For the inversions performed in this section, the resistivities from the model obtained from the denser grid inversion presented in the previous section (Figure 5.33) were defined as the fixed resistivities for all the layers except for the layer between -500 and -1000 m, containing the CO_2 plume. For this layer the initial resistivity was set to 2 Ωm. Since the inversion was constrained to only this one layer, this layer was more densely gridded, with the aim of obtaining a more detailed resistivity model of the CO_2 plume. A version of Grid 3 was applied, but with even denser vertical gridding of the whole layer, and denser horizontal gridding between 12000 and 15000 m along the CSEM towline. Figure 5.34 shows the initial model and inversion grid in the inversion setup for the constrained inversions.

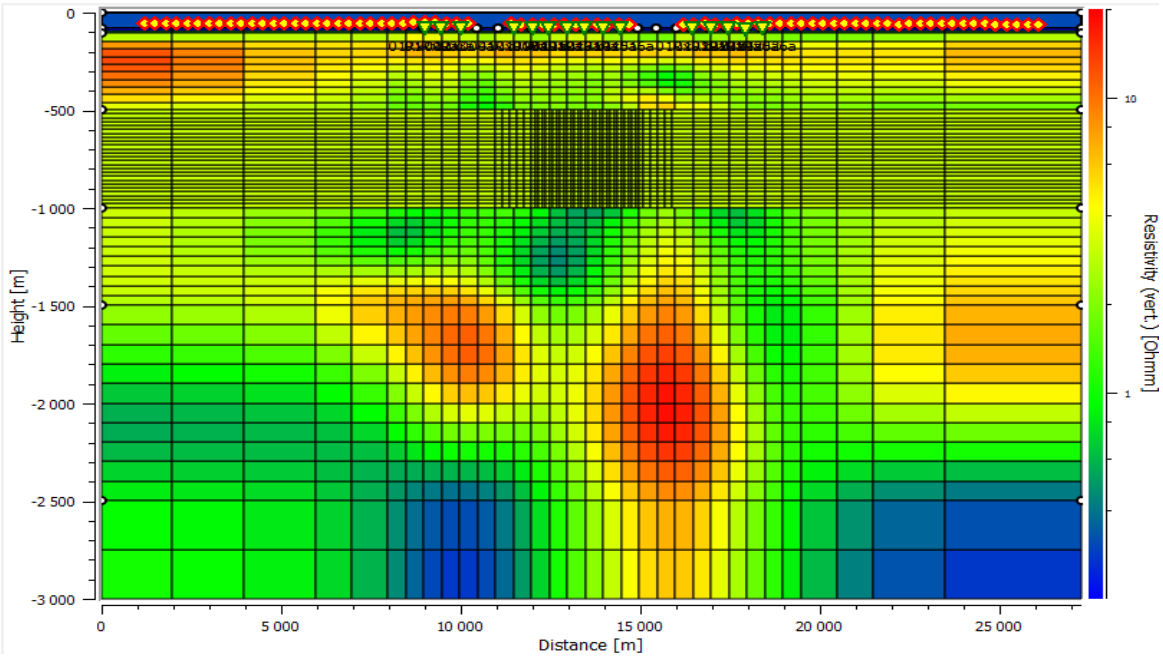

Figure 5.34: Initial model and inversion grid in the inversion setup for the constrained inversions. The resistivities from the model in Figure 5.33 was fixed for all layers except the layer containing the CO_2, between -500 and -1000 m. Only this layer was inverted for, with the initial resistivity set to 2 Ωm.

The resistivity model resulting from the constrained inversion is presented in Figure 5.35. The location of the CO_2 plume is quite similar to the result without the constraints in Figure 5.33, but the extent of the CO_2 plume is reduced, and the shape of the anomaly is a bit tilted. The strength of the resistivity anomaly at the center of the plume is 17.5 Ωm, so the result doesn't seem to have improved with respect to the response of the CO_2 plume. Due to the ambiguous results for the optimal maximum offset, the same inversion was also performed where the maximum offset was reduced from 8000 to 6000 m, in order to see if this could improve the resistivity image in the constrained inversion. Very few differences

could be observed in the resulting resistivity image, and the response of the CO_2 anomaly was more or less identical.

The inversion results in section 5.7.1, where the magnitude and phase data were inverted for separately, indicated that the phase contained most of the information about the subsurface, and that a very similar inversion result could be obtained by only inverting the phase data. The results from a constrained inversion where only phase data was included is presented in Figure 5.36. This inversion result is very similar to the constrained inversion result where both magnitude and phase were included, with a nearly identical resistivity anomaly for the CO_2 plume.

The resistivity model resulting from the inversion where the water layer was included (Figure 5.30) suggested a water resistivity of 0.27 Ωm, instead of 0.3125 Ωm which have been employed in the previous inversions. A constrained inversion was therefore performed where the resistivity of the water was set to 0.27 Ωm, and the result is presented in Figure 5.37. In this result, the vertical extent of the plume has increased, the location has improved, and the resistivity in the center has increased to 36.4 Ωm, compared to 18.4 Ωm in the inversion result without the constraints in Figure 5.33. However, the horizontal extent of the CO_2 from the result without the constraints seem to fit better with the observed extent in the seismic, and a distinct discontinuity can be observed along the lower boundary at of the constrained layer, at -1000 m. Discontinuities in the resistivity can be observed along the layer boundaries in all of the constrained inversion results, and indicates that the fixed background resistivity is incorrect. If the CO_2 plume was the only difference between the background and constrained inversions, these boundary transitions should be smooth, and the resistivities similar at each side of the layer boundaries. The method of applying the resistivities from another resistivity model that also included the CO_2 plume for the other layers of the model, did not provide an improved resistivity image.

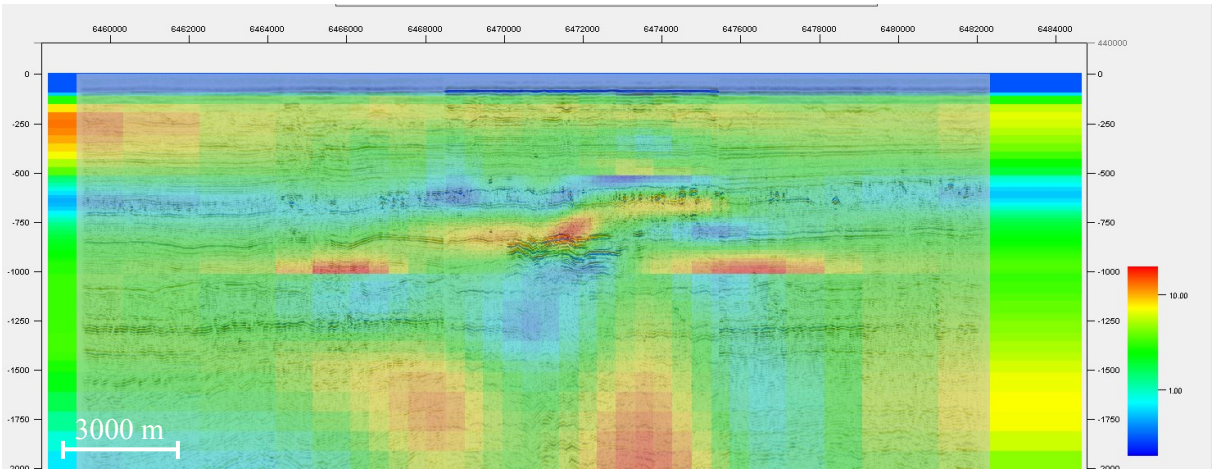

Figure 5.35: Vertical resistivity profile resulting from the constrained inversion where only the layer between -500 and -1000 m was inverted for, with the inversion result from Figure 5.33 employed as background resistivity for the rest of the model.

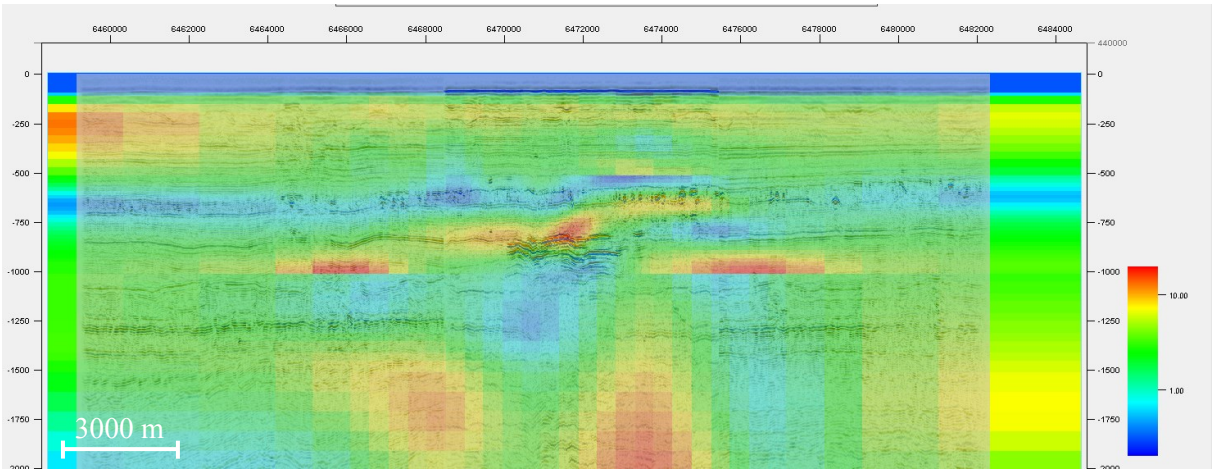

Figure 5.36: Vertical resistivity profile resulting from the constrained inversion where only the phase data and the layer between -500 and -1000 m was inverted for, with the inversion result from Figure 5.33 employed as background resistivity for the rest of the model.

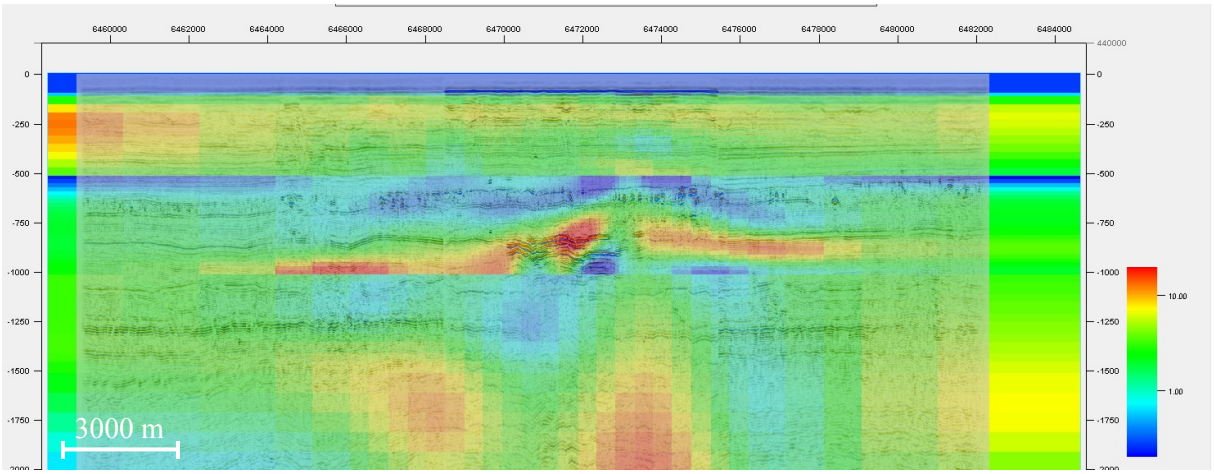

Figure 5.37: Vertical resistivity profile resulting from the constrained inversion where only the layer between -500 and -1000 m was inverted for, with the inversion result from Figure 5.33 employed as background resistivity for the rest of the model, and a water resistivity of 0.27 Ωm instead of 0.3125 Ωm.

5.9 Filtering to remove airwave response

Due to the shallow water in the Sleipner area, the CSEM data is strongly influenced by the airwave generated at the air-water interface. The shallow water causes the airwave do start to dominate at much shorter offsets than it would have done in deeper waters, and also to be of higher magnitude since the total attenuation of the signal on the way through the water is smaller. One way to address the airwave challenge in the inversions is to attempt to filter out the data strongly influenced by the airwave. One approach, which is tested in this study and presented in section 5.9.1, is to only include offsets smaller than where the airwave starts to dominate the response. Another is to separate the up-going and down-going response of the electromagnetic field, and remove the down-going component that represents the airwave response. This method has not been tested in this study, as this requires a more comprehensive

filtering process. The need for airwave removal in CSEM data is disputed, and different opinions exist (Amundsen et al., 2006; Constable, 2010). Some think that modeling the airwave response in a good way, will give better results than trying to remove it from the data. Since the *ngi25em* software models the airwave in the inversion calculations, airwave removal is not a large focus of this study.

5.9.1 Excluding data dominated by airwave

As described previously (section 4.2), the large skin depth of the air will cause a decreased attenuation of the total CSEM signal with offset when the airwave starts to dominate the response. The onset of the airwave can therefore be determined from the point where the magnitude and phase curves flatten out in AVO and PVO plots, respectively. Based on this, the data dominated by the airwave response can be determined and excluded from the inversions. For the 0.5 Hz signal, the airwave onset can be determined to offsets of about 4500 m, and around 2000 m for the 7 Hz signal. For the other four frequencies the airwave starts to dominate at offsets in between these. It is important to keep in mind that since the airwave starts to dominate at such short offsets, it masks part of the guided mode response from the CO_2 plume. Consequently, by removing the response for all offsets where the airwave dominates, some of the target response will also be lost.

Figure 5.38 shows the inversion result where data from offsets where the airwave dominates the response have been removed, in the dataset from section 5.4 (Figure 5.7) where data from the seven closely spaced receivers have been removed, but before the pipeline data had been filtered out. The inversion result is not very good compared to the result in Figure 5.7, as the strength of the CO_2 resistivity anomaly is significantly reduced, from 17.7 Ωm to 11.0 Ωm, and its location is shallower. When the same approach was applied for the dataset where data from additionally five receivers and corresponding source points were removed to reduce the pipeline influence, no distinct resistivity anomaly could be detected near the location of the CO_2.

The resistivity model presented in Figure 5.39 shows the result when data from offsets where the airwave dominates the response have been removed, for the constrained inversion setup in Figure 5.34. In this result, the strength of the CO_2 resistivity anomaly has improved, from 17.5 Ωm to 24.7 Ωm, compared to the constrained inversion result without the airwave filtering in Figure 5.35. However, the location of the resistivity anomaly is a bit deep, and centered at the lower northern part of the plume in the seismic. A distinct discontinuity can also be observed at the layer boundary at -1000 m, indicating that the resistivity image is incorrect. If a more accurate background resistivity had been employed for the constrained inversion, maybe this method of airwave filtering could have been more successful.

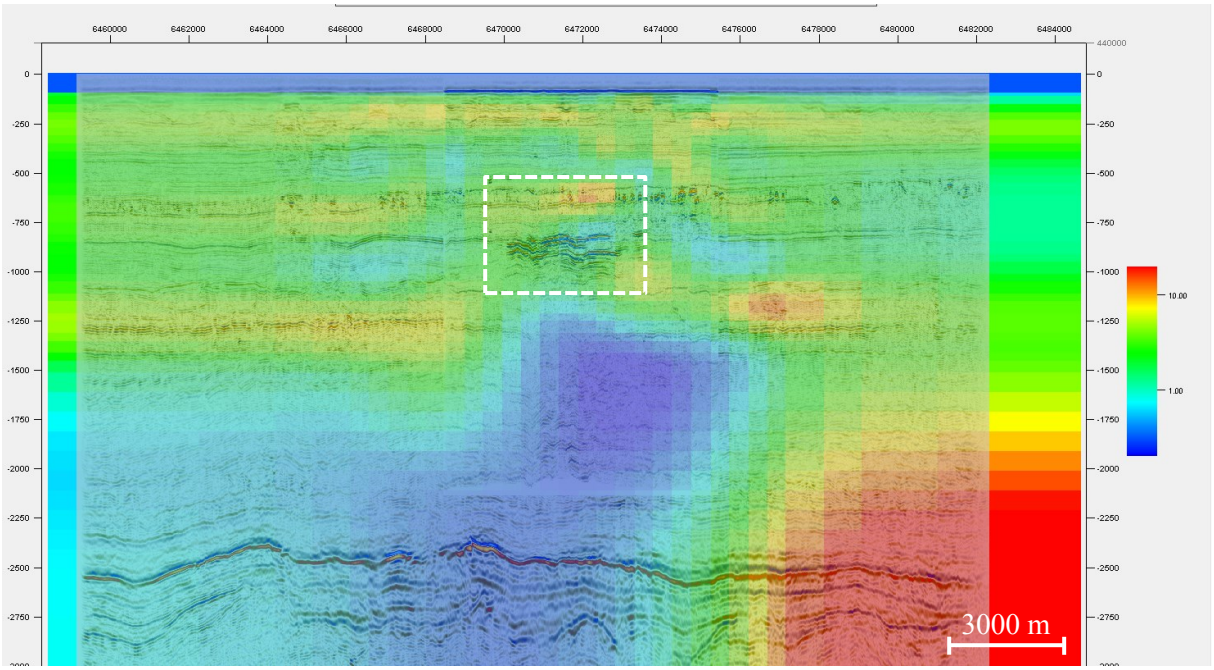

Figure 5.38: Vertical resistivity profile resulting from inversion of the dataset from section 5.4, where data from seven closely spaced receivers were removed, after removing data from the offsets where the airwave dominates the response.

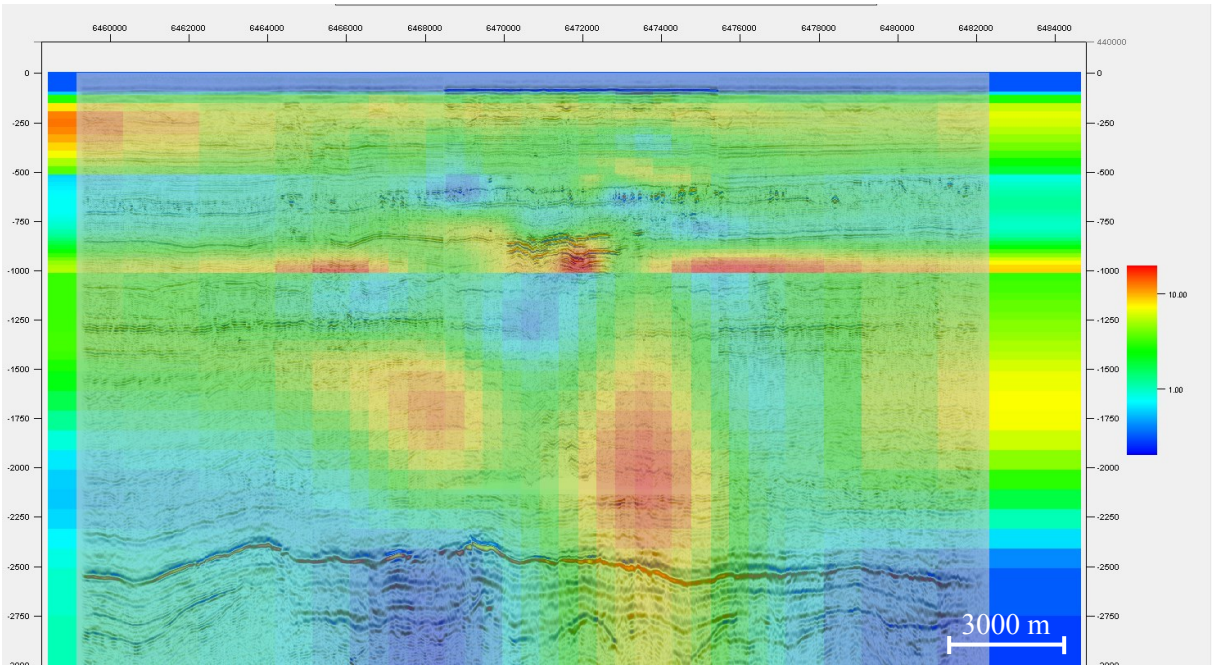

Figure 5.39: Vertical resistivity profile resulting from the constrained inversion of the dataset employed in the constrained inversion in Figure 5.35, after removing data from the offsets where the airwave dominates the response.

6 Discussion and inversion strategy

The most important findings from the different inversions performed for the Sleipner data are discussed in the following chapter, and summarized in an inversion strategy in section 6.8. The strategy is applicable for the Sleipner CSEM dataset and similar case studies, as well for hydrocarbon exploration, production and monitoring in similar environments.

6.1 Frequency analysis

The conclusion drawn from the single frequency inversion results presented in section 5.5, is that inverting for single frequencies does not provide a satisfying subsurface resistivity model. The explanation for this is, that by including only a single frequency response in the inversion, the restrictions put on the model is reduced compared to when including all, or at least multiple, frequencies. More solutions (resistivity models) exist that would provide the same response for one single frequency, than when including the responses from several frequencies. This is demonstrated by the sensitivity study presented by Constable et al. (2010) as well, briefly discussed in section 2.2.4.

Different frequencies are sensitive to different depths of the subsurface, and are affected differently by the presence of the CO_2 plume, due to the difference in skin depth. The more frequencies included in the inversion, the more constraints are put on the solution, which increase the probability of obtaining a representative inversion result. The inversions including three well-spaced frequencies (section 5.7.4) did give a better result than when only including single frequencies, but the best result was by far obtained when all the six available frequencies were included in the inversions.

In the forward modeling study in chapter 4, the magnitude of the modeled response in the presence of the target seem to be larger than the background response when it first starts to dominate, while at some offset the difference becomes negative. This negative difference may be the reason for the negative anomaly observed in the area of the CO_2 plume in some of the inversion results where single frequency data was inverted for. The offsets where the modeled target response goes from being larger to smaller than the background response will vary with frequency, and might explain why this negative anomaly appears shallower for higher frequencies. The positive and negative target response compared to the background response can either be explained by a positive anomaly at a given depth, or a negative anomaly at another given depth. The least-squares method distributes the anomaly between these two possibilities, but in lack of constraints, most of the anomaly response is assigned to the negative anomaly. Including data of several frequencies reduces this artefact, since this negative difference in response will be at different offsets for the different frequencies, indicating different depths of the artificial negative anomaly. However, a weak negative anomaly can also be observed below the positive

resistivity anomaly of the CO_2 plume in many of the resistivity models where all the frequencies are included in the inversion. This may be an artefact explained by that some of the anomalous response still is assigned to the artificial negative anomaly.

6.2 Offset range optimization

Testing of the optimal offset range were conducted at several stages in the inversion study. A minimum offset of 1000 m proved to be optimal for all the cases, but the optimal maximum offset of the dataset was trickier to determine. A maximum offset of 10000 m resulted in the weakest resistivity anomaly, and for the case where only data from the seven closely spaced receivers had been removed (section 5.4), a maximum offset of 6000 m resulted in the strongest resistivity anomaly. However, when the data from the five receivers which were strongly influenced by the seabed pipelines had been filtered out, together with source points from the same areas (section 5.6.2), maximum offsets of 6000 m and 8000 m gave very similar results with respect to the strength and location of the resistivity anomaly of the CO_2. Smaller maximum offsets will lead to less data, and thus less calculations in the inversion process, which will require shorter time to perform the inversion. On the other hand, smaller offsets will also reduce the sensitivity to the deeper parts of the model, increasing the uncertainty related to these areas. Since the difference seemed to be minimal for the CO_2 plume, a maximum offset of 8000 m was employed in majority of the inversions, since this provides higher sensitivity to larger parts of the model.

6.3 Magnitude and phase information

The results from the separate inversions of magnitude and phase data presented in section 5.7.1 indicates that the phase data seem to contain most information about the subsurface resistivity. In the magnitude data inversion result, little resistivity variations could be observed in the resistivity profile, while the inversion of the phase data gave a very similar resistivity model compared to when both phase and magnitude were included. This implies that one may only need to invert for phase to obtain a good resistivity model of the subsurface, and this was also tested for a constrained inversion in section 5.8. Also in this case, the inversion provided a resistivity model as good as when inverting for both magnitude and phase data.

6.4 Pipeline data filtering and data reduction

The effect of the seabed pipeline network on the CSEM data has proven to depend on frequency and offset, and also on the size of the pipeline and the angle between the pipeline and the survey line (section 5.6.2). Determining the data influenced by pipelines based on the location of the receivers relative to the pipeline crossing points from the map, therefore led to the removal of much more data than necessary.

The method of normalizing the magnitude with respect to the response of off-target receivers, and then plotting it with respect to CMP position along the towline and half offset, proved to be an efficient and systematic way to determine which data to filter out to reduce the pipeline influence. Data from the receivers with strong anomalies in the nAVO response should be filtered out, and since data from these areas can be assumed to be strongly influenced by the pipelines, source point data from these areas should also be filtered out.

This method would provide more accurate information if the data could be normalized with respect to a baseline resistivity model without the presence of the pipelines, instead of data from off-target receivers. The data from the off-target receivers may not be representative for the geology/resistivity in the target area, which increases the uncertainty related to the nAVO response, and is a possible source of error. However, baseline surveys without the pipeline network would be unrealistic to acquire, also for future projects, and the normalization by off-target receivers seems to be the best option.

Another approach that was considered related to the challenge with the pipeline influence, was to model the pipelines instead of removing data. Since the inversion software seem to model the airwave in a good way, it could also be able to model the pipelines if these were included in the initial model. On the other hand, the 2D model assumes homogeneous properties in the perpendicular direction of the model, while the software generates a 3D wave field. Since most of the pipelines cross the profile with an angle, it is very difficult to model an accurate response from the pipelines.

When removing closely spaced receivers, and data from receivers strongly influenced by pipelines, the amount of data included in the inversions was significantly reduced. However, the inversions still provide good resistivity models, compared to the initial inversion result. This implies that the number of receivers presumably can be reduced at the data acquiring stage, which will reduce the cost of the CSEM survey, as well as the time it takes to process the data, significantly. This will be further studied in the inversion study performed for the synthetic Skade data in chapter 7.

6.5 Constrained inversion

The resistivity images obtained in section 5.8, when constraining the inversions to the layer containing the CO_2, did not seem to improve the resistivity image of the CO_2 plume. Discontinuities were observed along the boundaries of the constrained layer, which implies that the fixed resistivities for the other parts of the model were incorrect, and deviates from the real resistivity of the subsurface. In lack of a baseline resistivity image, the resistivity from the best inversion result obtained was employed for these fixed resistivities. The presence of the CO_2 in these data is assumed to also affect other parts of the model than just the area of the CO_2, leading to incorrect fixed resistivities in the constrained inversion model.

If a baseline resistivity model had been available and employed instead, this may have given an improved resistivity image. This will also be further studied in the inversion study performed for the synthetic Skade data in chapter 7, where a baseline survey is available.

6.6 Airwave filtering

The airwave filtering performed in section 5.9.1, based on removal of data where the airwave dominates the response, was not very successful when inverting for the whole resistivity model. Neither the strength nor location of the resistivity anomaly of the CO_2 plume were good compared to the results where the airwave response was included. This was as expected, since the shallow water in the area leads to the airwave dominating the response from very small offsets, masking large parts of the response from the CO_2 target. When the data dominated by the airwave response were removed, so was large parts of the response from the CO_2 plume.

The method was more successful when a constrained inversion was carried out. In this case the resistivity response of the CO_2 plume was quite good, but the location was a bit deep and discontinuities at the layer boundaries indicated incorrect resistivities. If a baseline survey had been available, a better background resistivity could have been obtained, and the airwave filtering may have provided a better resistivity image. However, it seems like the *ngi25em* software models the airwave in a sufficiently good way, and airwave filtering doesn't seem to be necessary to provide a representative resistivity model of the subsurface.

6.7 Further interpretations

After obtaining a well resolved resistivity model of the CO_2 plume, EM rock physics can be employed to estimate the saturation and mass of the CO_2 plume. This information is valuable when it comes to CO_2 monitoring, as it can give strong indications of whether the reservoir is leaking, and also for hydrocarbon production and monitoring. Due to time restrictions, such calculations were not performed in this study, but in practice it can be done by extracting the resistivity values from the anomaly representing the CO_2 plume in the resistivity profile. By employing rock physic relations between resistivity and saturation, e.g. Archie's law (Archie, 1942), the saturation of CO_2 can be estimated. An estimate of the mass of the CO_2 can then be calculated by employing

$$M_{CO_2} = \sum \rho_{CO_2} \varphi S_{CO_2} V \tag{6.1}$$

where ρ_{CO2} is the density of the CO_2, which have to be estimated, and S_{CO2} is the calculated saturation of CO_2 for each grid cell in the resistivity model of the plume. φ is the porosity of the formation, which

is averaged to 0.37 by Chadwick, Arts, & Eiken (2005), and V is the volume of each grid cell in the model, defined by the 2D size of the grid cell, and an estimate of the extent of the CO_2 plume in the direction perpendicular to the model. A rough estimate of this can be determined based on the extent of the plume in Figure 1.5. The mass of CO_2 is summed over all the volume elements, and gives an estimate of the total mass of CO_2 (M_{CO_2}) present.

6.8 Inversion strategy

Based on the different inversions performed, and the observations made from the resulting vertical resistivity models, an inversion strategy has been developed for the Sleipner 2008 CSEM dataset. The strategy for inverting the Sleipner dataset is summarized in the points below, and is applicable for similar case studies, and for hydrocarbon exploration and production in similar environments. The results in the inversion study may be applied to modify the inversion strategy for different environments as well.

Data processing

- Data from closely spaced receivers with similar CSEM response, can/should be removed to reduce the amount of data and speed up the inversion process.

- Data strongly influenced by the pipeline network at seabed can be identified by normalizing the magnitude with respect to the response of off-target receivers, and then plotting it with respect to CMP position along the towline and half offset, as described in section 5.6.2. Data from the receivers determined from this data analysis should be filtered out, together with source point data from the same areas. This will reduce the influence from the pipeline network significantly.

- All frequencies should be included in the inversions to obtain the best result. However, it seems to be sufficient to invert only the phase data, as this carries the most information about the subsurface.

- An offset range between 1000 m and 6000 or 8000 m should be applied to obtain the strongest and best located resistivity anomaly for the CO_2 plume. A maximum offset of 8000 m is assumed to be sensitive to larger parts of the model.

- The data should be resampled at 300 m, as this will reduce the time of the inversions, but still provide a representative resistivity image of the subsurface.

- Data error estimates of 3 % for the magnitude and 0.01 radians for the phase data should be applied.

- The *ngi25em* software seem to model the airwave in a sufficiently good way, hence airwave filtering is not required to obtain a representative resistivity image.

Inversion setup

- Available a priori information should be studied to define a representative starting model for the inversions, and M1 can be used for the Sleipner dataset. To take into account the uncertainties related to the layer boundaries in the starting model, and avoid the resulting resistivity model to be constrained by this, an inter-layer smoothing fraction of 1 should be applied. This allows a smooth resistivity transition across the predefined layers in the starting model. A relatively high weight should be assigned to the smoothing operator to generate smooth models, while zero weight should be applied to the a priori model.

- The water layer can be modeled as a homogeneous layer of 0.3125 Ωm resistivity.

- The resistivity model should be parameterized with a grid that is coarsening with depth, and also towards the sides of the model, were the sensitivity is lower. A much denser gridding should be applied to the layer where the target is located, with the highest density at the location of the CO_2, decreasing density towards the sides of the model. Grid 3 can be applied for the Sleipner dataset.

7 Inversion of synthetic CSEM data from Skade

The inversion setup and results from an inversion study of the synthetic CSEM data from the Skade case study are presented in the following chapter. The aim of the study is to demonstrate the potential and sensitivity of the CSEM method when it comes to CO_2 injection monitoring, and also to show the advantage of acquiring a baseline CSEM survey. This was not available for the Sleipner data study, but would have been very helpful in the process of inverting and analyzing the data. Inversions with varying numbers of receivers have also been performed, in order to see the effect on the resulting resistivity model.

7.1 Synthetic inversion setup

Synthetic data from the area of the middle CO_2 injection simulation at Skade was available for the inversion study, and both the baseline data from year 2020 and the post injection data from 2070 was employed. The Sleipner and Skade CO_2 projects have several similarities, such as shallow water, shallow target location, and similar surroundings, so the inversion strategy presented in section 6.8 was applied in the study, with some modifications. Six well-spaced frequencies and 300 m source sampling seemed to be sufficient in the inversions performed with the Sleipner data, so this was also employed in the Skade case, and 0.1, 0.25, 0.5, 1, 2, and 5 Hz frequency data were included in the inversions. The same minimum offset of 1000 m was also employed, but the maximum offset was set to 10 000 m, due to the deeper location of the Skade formation, and the deeper water.

Prior to the inversions, noise was added to the synthetic data to make them more realistic. Noise will always be present in real data, so by adding noise to the synthetic data, the inversion results will be more realistic. 3 % noise was applied to the magnitude data, while a constant value of 0.01 radians was applied to the phase data. The same values were also defined for the data error estimates.

The resistivity model in the inversion results covers the profile along the simulated CSEM towline, down to a depth of 5000 m, with the upper 150 m representing the water layer. In the starting model the water resistivity was set to 0.3 Ωm, and this layer was excluded from the inversions. The rest of the model was divided into three layers, with the layer of the CO_2 accumulation ranging from 600 to 1600 m depth. All of the subsurface layers was given a horizontal resistivity of 1 Ωm, and an anisotropy factor of 2. This anisotropy factor was also employed in the model used to generate the synthetic data. The model was gridded according to the inversion strategy developed for the Sleipner dataset, with a finer grid in the upper, central parts of the model, coarsening to the sides and lower parts, where the resolution of the data decreases.

The approach of the study was to first invert the 2020 baseline data, to obtain a baseline resistivity model. This was then used as a starting model for the inversion of the 2070 data. Ideally, the only difference between the resistivity models resulting from these two inversions would be the higher-resistivity area representing the accumulated CO_2 plume. If other parts of the model also differ, which they most likely do, the inversion can be constrained to the layer where the CO_2 is located, employing the resistivity values from the baseline survey for the background and initial resistivity. Such changes in parts of the model outside the CO_2 accumulation can occur due to the impact from the CO_2 plume, noise in the data, and/or for real data, different circumstances leading to different conditions at the acquisition times of the time-lapse survey. When a good resistivity profile was obtained for the 2070 data, inversions were also performed where data from a reduced number of receivers was included. In the Sleipner data study, the inversion results proved to be representative when data from several receivers and areas of source points had been removed, and this is of interest to study further for the Skade data as well. If one can reduce the number of receivers, and still obtain the same resistivity profile, this can be a potential way of reducing the costs of time-lapse CSEM surveys significantly. The results from the Sleipner inversion study also indicated that only inverting phase data could provide equally good results as when both magnitude and phase data were inverted for. To further investigate this theory, separate inversions of magnitude and phase data were also performed for the synthetic Skade data.

7.2 Synthetic inversion results

The resistivity models resulting from inverting the synthetic Skade data is presented in this section. Like the results from the Sleipner inversion study, the vertical resistivity models resulting from the inversions are presented along the CSEM survey line, but no seismic was available for comparison and evaluation of the results. The models are evaluated based on the horizontal resistivity models in Figure 1.8. The color scale representing the vertical resistivity values in the inversion results is logarithmic, and ranges from 0.3 to 50 Ωm. The upper resistivity profile in Figure 7.1 shows the baseline inversion result for the 2020 data. The middle profile shows the result when inverting the 2070 data, using the 2020 baseline resistivity model as the starting model, and the bottom profile shows the result from the constrained inversion of the 2070 data, where only the layer between -600 and -1600 m was inverted for. In the baseline inversion result, large parts of the profile is characterized by a vertical resistivity around 2 Ωm. An area of lower resistivity, around 1 Ωm, can be observed around 2000 m depth, and the deeper parts of the model is characterized by an area of higher resistivity, between 10 and 15 Ωm. This baseline resistivity model is very similar to the model used as input when generating the synthetic data, shown in the upper profile in Figure 1.8 (note that this is the horizontal resistivity, with anisotropy factor 2).

The resistivity model from the unconstrained inversion of the 2070 data clearly shows a high-resistivity area in the middle of the profile, between 800 and 1300 m depth, and with a horizontal extent of around

8000 m, which represents the accumulated CO_2 plume. However, several differences from the baseline resistivity model can also be observed in other parts of the profile. The resistivity and/or location of the areas of high- and low resistivity observed in the baseline profile has changed, due to the presence of the CO_2. Also, two areas of higher resistivity can be observed towards each side of the profile, at around the same depth as the CO_2 plume. These are related to the two other CO_2 injection sites in the Skade Fm.

In the resistivity model from the constrained inversion of the 2070 data, the baseline inversion result was used as the initial model, and only the layer containing the CO_2 plume was inverted for (-600 to -1600 m). The grid density of the layer was increased, in order to improve the resolution. In the resulting resistivity profile, the position of the plume is similar to in the unconstrained inversion result, but the horizontal extent is increased to around 10000 m, and the vertical extent is slightly reduced, to between right below -800 m and -1200 m. This is closer to the extent of the plume in the model employed in the simulations, where the horizontal extent was about 12000 m, and the vertical extent was between -900 m and -1100 m. The vertical resistivity at the center of the CO_2 plume is increased to 46.5 Ωm, compared to 33.6 Ωm in the unconstrained inversion result. Quite large differences occur in the location and strength of the two resistivity anomalies related to the CO_2 accumulations at the other two injection sites, but these are located close to the sides of the model. Since only data from the area of the middle injection site is included in the study, the sensitivity and resolution over the other CO_2 accumulations are low.

The upper resistivity model in Figure 7.2 is the same as the lower one in Figure 7.1, only zoomed in at the upper half of the model where the CO_2 is located. The three resistivity models below are the results from the same constrained inversion, with the baseline resistivity model as starting model, but with reduced number of receivers. In the second resistivity model in Figure 7.2, only data from every other of the 21 receivers were included, 11 in total. In the third model, the receiver data was reduced to every fourth receiver, so only data from six receivers were included, while in the last model, data from additionally two receivers were excluded from the inversions, and only data from the two end receivers and two receivers above the CO_2 plume were included. At first glance, all the resistivity profiles look very similar. In the second model, where only data from every other receiver was inverted for, the response of the CO_2 plume is more or less identical as in the case where data from all the receivers were included, and the resistivity of the center of the plume is approximately the same, 47.5 Ωm. The largest differences from the first result are the reduced resistivity of the CO_2 injection in to the left in the model, and a lower resistivity area right below the CO_2 plume. For the third model, when only data from every fourth receiver was included in the inversions, the shape of the CO_2 plume is slightly changed, and the resistivity in the center is reduced to 37.5 Ωm. In the last model, where only data from four receivers were included, the resistivity is reduced to 35.4 Ωm, the shape differs more, and the extent is reduced.

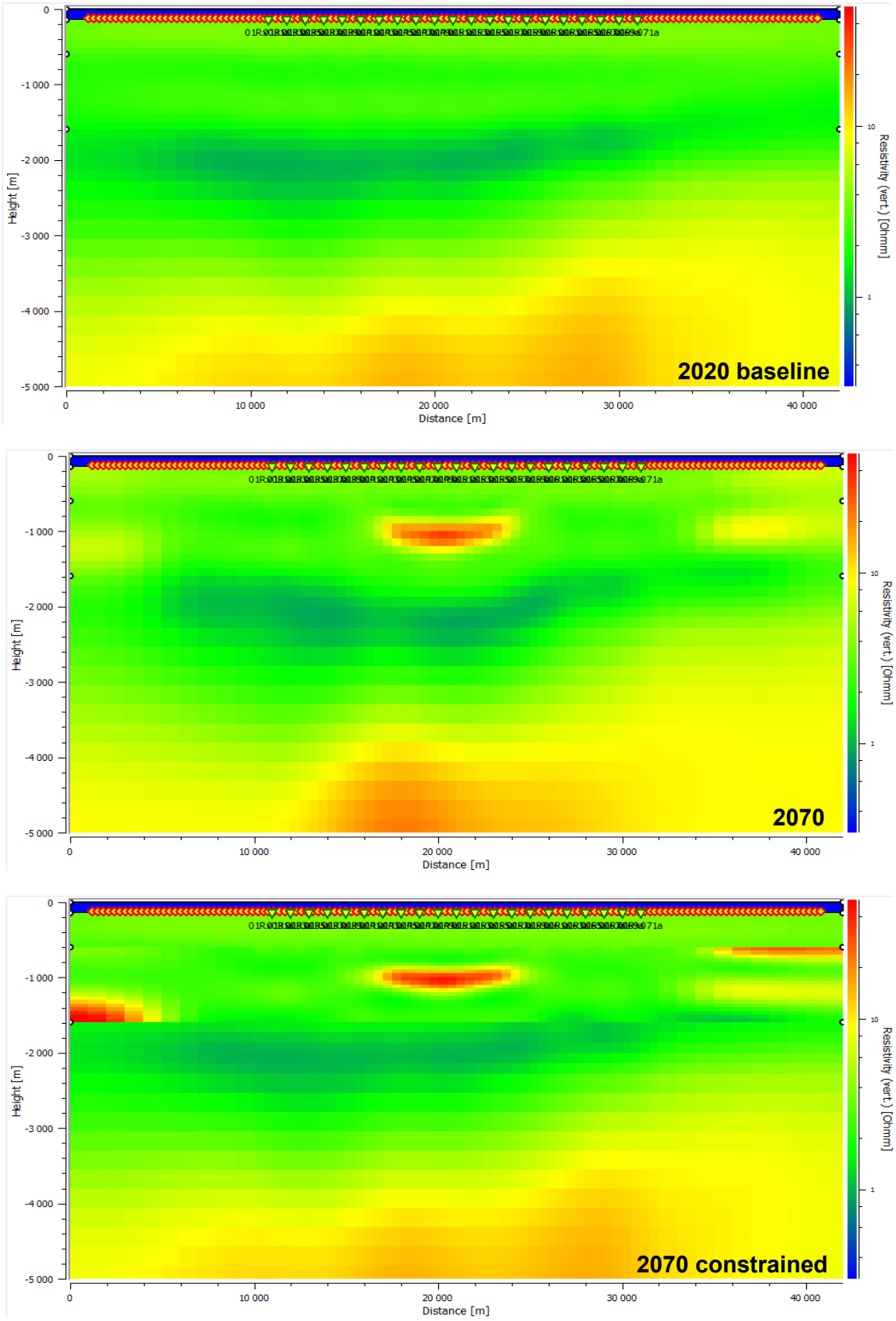

Figure 7.1: *Top*: baseline inversion result from the Skade 2020 data. *Middle*: resistivity model resulting from inversion of the 2070 Skade data, with the 2020 baseline result used as starting model. *Lower*: resistivity model from a constrained inversion of the 2070 Skade data, with the 2020 baseline result used as starting model, and only inverting for the interval between -600 and -1600 m.

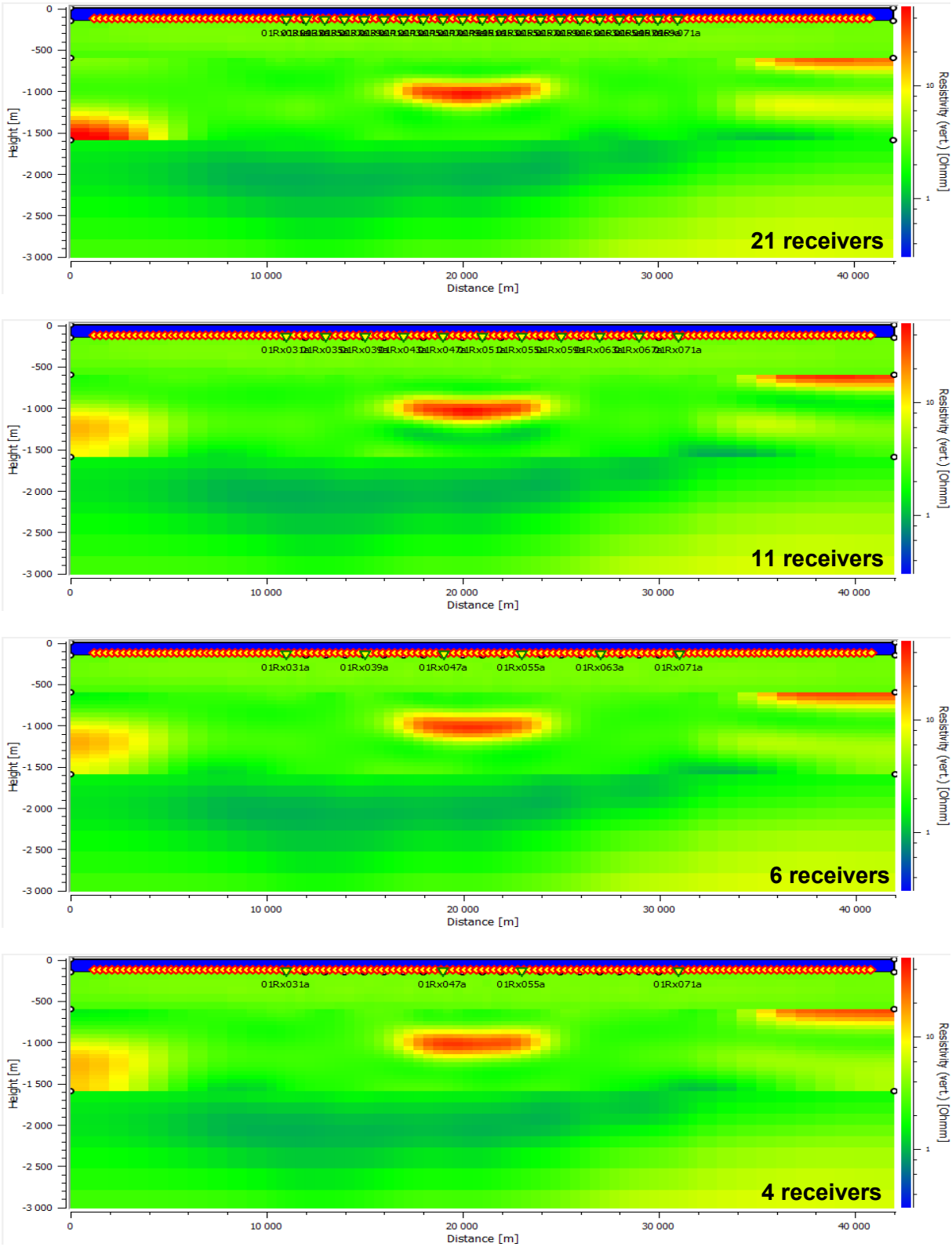

Figure 7.2: The upper resistivity model is the result of a constrained inversion of the 2070 Skade data, where the 2020 baseline result in figure 7.1 was used as starting model, and only the interval between -600 and -1600 m was inverted for. The second resistivity model is the result from the inversion of the same dataset, where only data from every other receiver was included (11 receivers in total). The next result shows the resistivity model where only data from every fourth receivers were included in the inversion (6 in total), while in the lower result, data from only 4 receivers were included.

Figure 7.3 shows the resistivity model from the constrained inversion of the 2070 Skade data where data from only 11 receivers were included (upper resistivity model), compared to the results from the same inversion when only inverting for magnitude (middle resistivity profile) and phase (bottom resistivity profile). When only inverting for magnitude data, the resistivity of the CO_2 anomaly is significantly reduced, to 30.9 Ωm, while an increase in the vertical extent, and decrease in the horizontal extent can be observed. The resistivity profile obtained when only inverting for phase data is nearly identical to the profile obtained when both magnitude and phase data was inverted for, also when it comes to the shape and strength of the resistivity anomaly of the CO_2 plume.

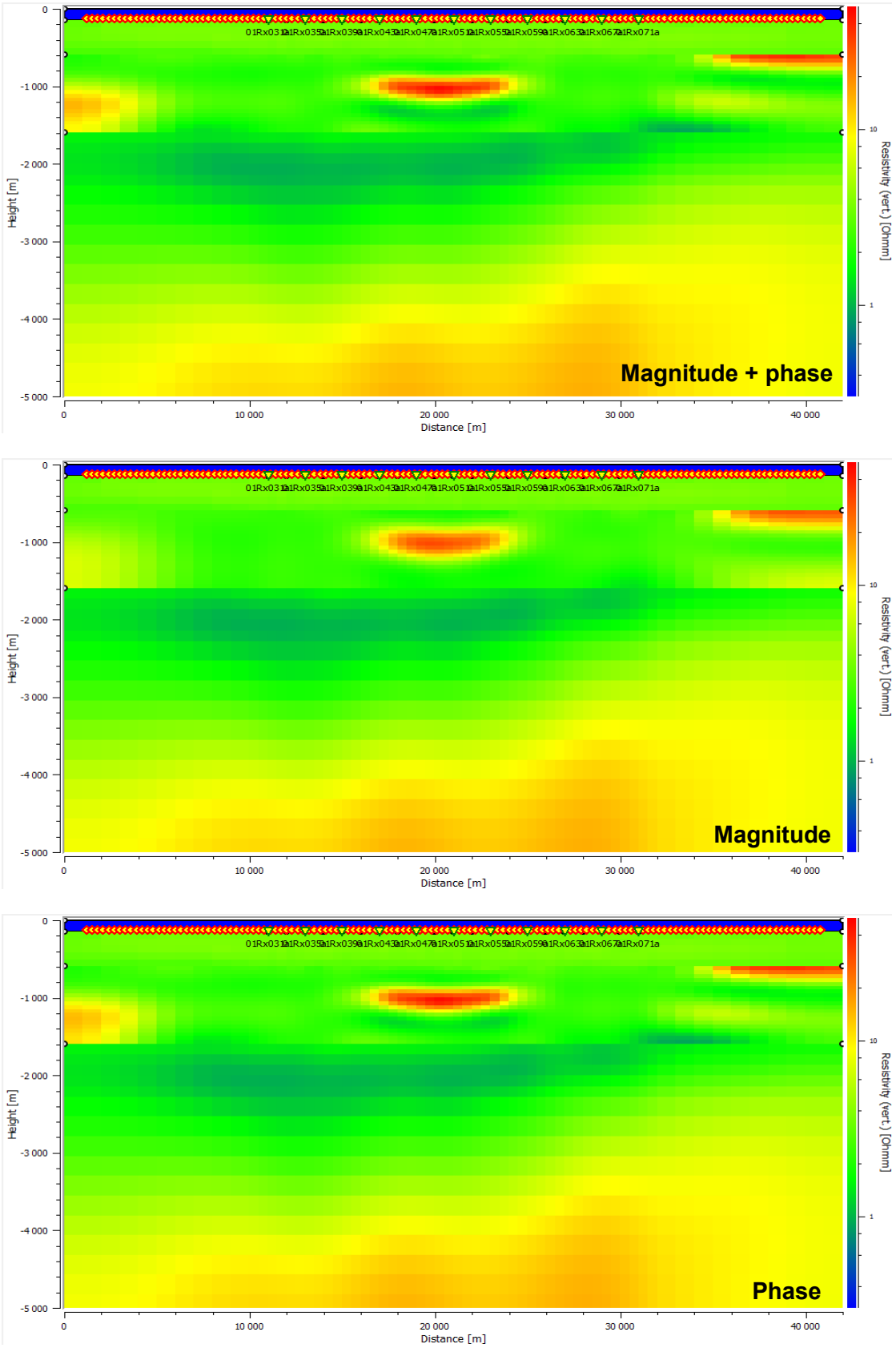

Figure 7.3: Resistivity model from the constrained inversion of the 2070 Skade data where data from 11 receivers were included (top), compared to the results from the same inversion when inverting for magnitude (middle) and phase (bottom) separately.

7.3 Discussion

The results in presented in Figure 7.1 shows how a good baseline inversion result can be employed to get an improved image of the target in a time-lapse CSEM survey. The baseline data is of great value when determining the background resistivity, and the changes in resistivity caused by the target structure are easier to determine. A constrained inversion where the baseline resistivity was used as initial model, proved to give an improved image of the CO_2 resistivity anomaly, with increased resolution. This method also provides a more representative resistivity image for the rest of the model.

When a good baseline resistivity model was obtained, constrained inversions for a reduced number of receivers also seemed to provide representative resistivity models. Even the inversion where only data from four of the receivers were included provided a fairly good resistivity image of the subsurface. However, in the resistivity models where data from only six and four receivers were inverted for, the resistivity of the CO_2 was lower, the vertical extent increased, and the horizontal extent decreased, compared to the resistivity models where data from more receivers were included. Considering the fact that this study is performed for synthetic data, larger differences may occur when inverting real data, and larger uncertainties might be related to the measurements. More measurements, e.g. data from more receivers, will increase the signal to noise ratio, and thus improve the inversion result. However, the resistivity model where data from every other receiver were included provided a very similar resistivity image, nearly identical for the CO_2 plume, compared to the result where data from all the receivers were included. This indicates that data from half of the receivers are sufficient to provide a representative resistivity model, and most likely would provide a good result if analyzing real data as well.

If an equally good inversion result can be obtained with a reduced number of receivers, this can reduce the cost of a time-lapse CSEM survey significantly. The need for less receivers will not only reduce the cost of the data acquisition, but also the time required for data processing and data inversion. It is important to keep in mind that this study was based on a good baseline resistivity model, and more data may be required to obtain a representative inversion result if a baseline survey is not available. Without the baseline data, the background resistivity is more uncertain, and an incorrect background model will affect the result from the constrained inversion. To get the best result, a good baseline result should therefore be used as the initial model, and the inversion constrained to only the layer containing the CO_2.

The resistivity images obtained when inverting for magnitude and phase data separately, indicates that inverting only for phase data is sufficient to provide the same result as when including both phase and magnitude in the inversion. This strengthens the theory about the phase carrying the most information about the subsurface, indicated by the Sleipner inversion study.

8 Conclusions

The main objective of this study was to establish an inversion strategy that could be applied to the 2008 CSEM dataset from Sleipner, in order to solve some of the challenges related to the pipeline network at seabed, the strong airwave response and the weak and shallow resistivity anomaly of the CO_2 plume. The inversion strategy presented in section 6.8 can be applied to obtain an improved resistivity image of the Sleipner CSEM dataset, compared to the resistivity image obtained in the initial inversion in Figure 5.4. The strategy is based on data processing and tuning of different inversion parameters, and defines the parameters, i.e. the inversion grid, offset range, a priori model, data density and error estimate, that provide the best resistivity image in terms of the response and location of the resistivity anomaly of the CO_2 plume. A systematic method for identifying and filtering out data strongly influenced by pipelines is also included in the strategy, which successfully reduces the artefacts generated by the pipelines in the resistivity image. The method identifies the strongly pipeline influenced data by normalizing the magnitude of the response measured at each receiver with respect to the mean response of off-target receivers, and plotting it with respect to CMP position along the towline and half offset. The inversion strategy is applicable for similar case studies, and also for hydrocarbon exploration and production in similar environments. The method for the pipeline filtering may also be modified to filter out unwanted influence from other features.

The study concludes that airwave filtering is not required to provide a representative resistivity image of the subsurface, since the *ngi25em* software models the airwave in a sufficiently good way. Airwave filtering is therefore not included in the inversion strategy. Inversions constrained to only the layer of the model containing the CO_2 plume did not improve the resistivity image already obtained by optimizing the other inversion parameters, so this was also excluded from the inversion strategy. However, the inversion study of the synthetic data from Skade indicated that if a good baseline resistivity image is available, this could be employed as the initial model in a constrained inversion to provide an improved resistivity image of the CO_2. To obtain the best resistivity image of the CO_2, the area of the plume should be densely gridded, whether the inversion is constrained or not.

Both in the Skade and Sleipner inversion studies representative resistivity images of the subsurface were obtained when only data from around half of the receivers were included in the inversions. For the Skade data, this corresponds to receivers every other km, and a total of 11 receivers in a stretch of 20 km above the target. For the Sleipner data, the receivers were more unevenly spaced, as receivers from two areas along the towline were removed in the pipeline data filtering. Representative resistivity images was obtained when data from 15 of 27 receivers, in a stretch of 9.5 km, was included in the inversions, so the receiver spacing was denser in this study. Since no baseline survey is available from Sleipner, in addition to larger uncertainties related to real data compared to synthetic, more data and denser receiver

spacing is probably required in this case. However, both studies indicate that a good resistivity image can be obtained with a significantly reduced number of receivers. If the number of receivers could be reduced at the acquiring stage, this would reduce the cost of the CSEM survey significantly.

In the inversion study of the Sleipner data, the best resistivity image was obtained when all the six available frequencies were included in the inversions. Only inverting for a few frequencies did not provide the necessary constraints on the inversion to obtain a representative resistivity image. Six well-spaced frequencies also provided a good resistivity image in the inversion study of the synthetic Skade data. In the Sleipner data study, the phase was discovered to contain more information about the subsurface resistivity, and only inverting the phase data was sufficient to obtain a good resistivity image. This is supported by the results from the synthetic Skade data study, where the resistivity model obtained when only inverting the phase data proved to be nearly identical to the result where both magnitude and phase were included in the inversions.

In the inversion study of the Sleipner data, a baseline survey would have been very useful in the inversion and interpretation of the data, and the inversion of the synthetic data from Skade demonstrated the value of this. For future CSEM projects related to CCS, and also hydrocarbon production monitoring, it would be advantageous to acquire baseline CSEM data prior to injection/drilling. This will ease the task of inverting and analyzing the data, and less uncertainty will be related to the effects of e.g. saturation changes in the target.

References

Amundsen, L., Løseth, L., Mittet, R., Ellingsrud, S., & Ursin, B. (2006). Decomposition of electromagnetic fields into upgoing and downgoing components. *Geophysics, 71*(5), G211-G223.

Archie, G. E. (1942). The Electrical Resistivity Log as an Aid in Determining Some Reservoir Characteristics.

Arts, R., Chadwick, A., Eiken, O., Thibeau, S., & Nooner, S. (2008). Ten years' experience of monitoring CO2 injection in the Utsira Sand at Sleipner, offshore Norway. *First break, 26*(1).

Auken, E., & Christiansen, A. V. (2004). Layered and laterally constrained 2D inversion of resistivity data. *69*(3), 752-761.

Carstens, H. (2009). *Technology: Changing exploration - using non-seismic technology*. Retrieved January 30, 2017, from GEO ExPro: http://www.geoexpro.com/articles/2009/01/technology-changing-exploration-using-non-seismic-technology

Carstens, H. (2015). Suksess for EM-data. *GEO365, 18*(4).

Chadwick, R. A., Arts, R., & Eiken, O. (2005). 4D seismic quantification of a growing CO2 plume at Sleipner, North Sea. *Vol. 6*, 1385-1399.

Constable, S. (2010). Ten years of marine CSEM for hydrocarbon exploration. *75*(5), 75A67-75A81.

Constable, S. (2016). *Marine EM: The Past, the Present, and the Future.* Retrieved November 14, 2017, from Home Page fro Steven Constable - SEG/AAPG Fall Distinguished Lecture Tour: http://marineemlab.ucsd.edu/Steve/SEGDL/index.html

Constable, S. C., Parker, R. L., & Constable, C. G. (1987). Occam's inversion: A practical algorithm for generating smooth models from electromagnetic sounding data. *52*(3), 289-300.

Constable, S., & Srnka, L. J. (2007). An introduction to marine controlled-source electromagnetic methods for hydrocarbon exploration. *72*(2), WA3-WA12.

Cox, C. S. (1981). On the electrical conductivity of the oceanic lithosphere. *Physics of the Earth and Planetary Interiors, 25*(3), 196-201.

de Groot-Hedlin, C., & Constable, S. (2004). Inversion of magnetotelluric data for 2D structure with sharp resistivity contrasts. *69*(1), 78-86.

Department of Earth, Ocean and Atmospheric Sciences, University of British Columbia. (2007). *Inversion concepts: Introducing geophysical inversion*. Retrieved May 22, 2016, from University of British Columbia: https://www.eoas.ubc.ca/ubcgif/iag/tutorials/invn-concepts/index.htm

Eidesmo, T., Ellingsrud, S., MacGregor, L. M., Constable, S., Sinha, M. C., Johansen, S. E., . . . Westerdahl, H. (2002). Sea bed logging (SBL), a new method for remote and direct identification of hydrocarbon filled layers in deepwater areas. *First break, 20*(3).

Ellingsrud, S., Eidesmo, T., Johansen, S., Sinha, M. C., MacGregor, L. M., & Constable, S. (2002). Remote sensing of hydrocarbon layers by seabed logging (SBL): Results from a cruise offshore Angola. *The Leading Edge, 21*(10), 972-982.

Gelius, L.-J. (2016). *Marine CSEM module* . Retrieved 2016, from GeoCLASS: http://www.unigeo.no/geoclass/node/843

Global CCS Institute. (2016a). *Understanding carbon capture and storage*. Retrieved March 2, 2016, from Global CCS Institute: https://www.globalccsinstitute.com/understanding-ccs

Global CCS Institute. (2016b). *Sleipner CO2 Storage Project*. Retrieved January 3, 2017, from Global CCS Institute: http://www.globalccsinstitute.com/projects/sleipner%C2%A0co2-storage-project

IPCC. (2005). *IPCC special report on carbon dioxide capture and storage.* Prepared by Working Group III of the Intergovernmental Panel on Climate Change [Metz, B., O. Davidson, H. C. de Coninck, M. Loos, and L. A. Meyer (eds.)]. Cambridge, United Kingdom and New York, NY, USA: Cambridge University Press, 442 pp.

Johansen, S. E., & Gabrielsen, P. T. (2015). Interpretation of Marine CSEM and Marine MT Data for Hydrocarbon Prospecting. In K. Bjørlykke, *Petroleum Geoscience: From Sedimentary Environments to Rock Physics* (pp. 515-544). Springer-Verlag Berlin Heidelberg.

Levenberg, K. (1944). A method for the solution of certain non-linear problems in least squares. *Quarterly of applied mathematics, 2*(2), 164-168.

Lowrie, W. (2007). Earth's age, thermal and electrical properties, Geoelectricity. In W. Lowrie, *Fundamentals of Geophysics, 2nd edition* (pp. 252-276). Cambridge university press.

Luz, E. D., & Régis, C. R. (2009). Influence of sea water resistivity on MCSEM data. *Revista Brasileira de Geofísica, 27*(3), 349-356.

Løseth, L. O., & Ursin, B. (2007). Electromagnetic fields in planarly layered anisotropic media. *Geophysical Journal International, 170*(1), 44-80.

Marquardt, D. W. (1963). An algorithm for least-squares estimation of nonlinear parameters. *Journal of the society for Industrial and Applied Mathematics, 11*(2), 431-441.

Mitsuhata, Y. (2000). 2-D electromagnetic modeling by finite-element method with a dipole source and topography. *Geophysics, 65*(2), 465-475.

NGI. (2010). *ngi25em Version 4.0 User Documentation.*

NIST. (2016). *Fundamental Physical Constants*. Retrieved March 1, 2017, from The NIST Reference on Constants, Units, and Uncertainty: http://physics.nist.gov/cuu/Constants/index.html

Norsk Petroleum. (2017). *Sleipner Øst*. Retrieved March 1, 2017, from Norsk Petroleum: http://www.norskpetroleum.no/fakta/felt/sleipner-ost/

NPD. (2011). *CO2 Storage Atlas Norwegian North Sea.* Retrieved April 6, 2017, from Norwegian Petroleum Directorate: http://www.npd.no/Global/Norsk/3-Publikasjoner/Rapporter/PDF/CO2-ATLAS-lav.pdf

NPD. (2017). *Wellbore*. Retrieved February 8, 2017, from Norwegian Petroleum Directorate - FactPages: http://factpages.npd.no/factpages/default.aspx?culture=en&nav1=wellbore

Paramor, O. A., Allen, K. A., Aanesen, M., Armstrong, C., Hegland, T., Le Quesne, W., . . . Frid, C. L. (2009). *MEFEPO North Sea Atlas.* University of Liverpool.

Park, J., Fawad, M., Viken, I., Aker, E., & Bjørnarå, T. I. (2013). CSEM sensitivity study for Sleipner CO2-injection monitoring. *Energy Procedia*, *37*, pp. 4199-4206.

Park, J., Vanneste, M., Bohloli, B., Viken, I., & Bjørnarå, T. I. (2014). In situ resistivity of CO2 plume at Sleipner from CSEM and gravity data. *Near Surface Geoscience 2014-First Applied Shallow Marine Geophysics Conference.*

Park, J., Viken, I., Bjørnarå, T. I., & Aker, E. (2011). CSEM data analysis for Sleipner CO2 storage. *Trondheim CCS-6 Conference, June 14-16.* Trondheim, Norway.

Ruppert, J. (1995). A Delaunay Refinement Algorithm for Quality 2-Dimensional Mesh Generation. *18*(3), 548-585.

Skjoldal, H. R. (2007). *ICES/EuroGOOS North Sea Pilot Project - NORSETT, Update report on North Sea conditions - 2nd quarter 2007.* Bergen: Institute of Marine Research.

Statoil. (2012). *Sleipner - Knowledge sharing in CCS projects - Workshop Mobile, Alabama*. Hentet March 16, 2017 fra SlideShare: https://www.slideshare.net/globalccs/hagen-13735499

Tveit, S., Mannseth, T., & Jakobsen, M. (2016). Discriminating time-lapse saturation and pressure changes in CO2 monitoring from seismic waveform and CSEM data using ensemble-based Bayesian inversion. *SEG Technical Program Expanded Abstracts 2016* (pp. 5485-5489). Society of Exploration Geophysicists.

Vöge, M., Park, J., & Viken, I. (2014). Multi-line 2D Inversion of Marine CSEM data using 3D Regularization, Extended Abstract for 22nd EM Induction Workshop, Weimar, Germany, August 24-30, 2014.

Appendix

Completion log well 15/9-13 (NPD, 2017)**:**

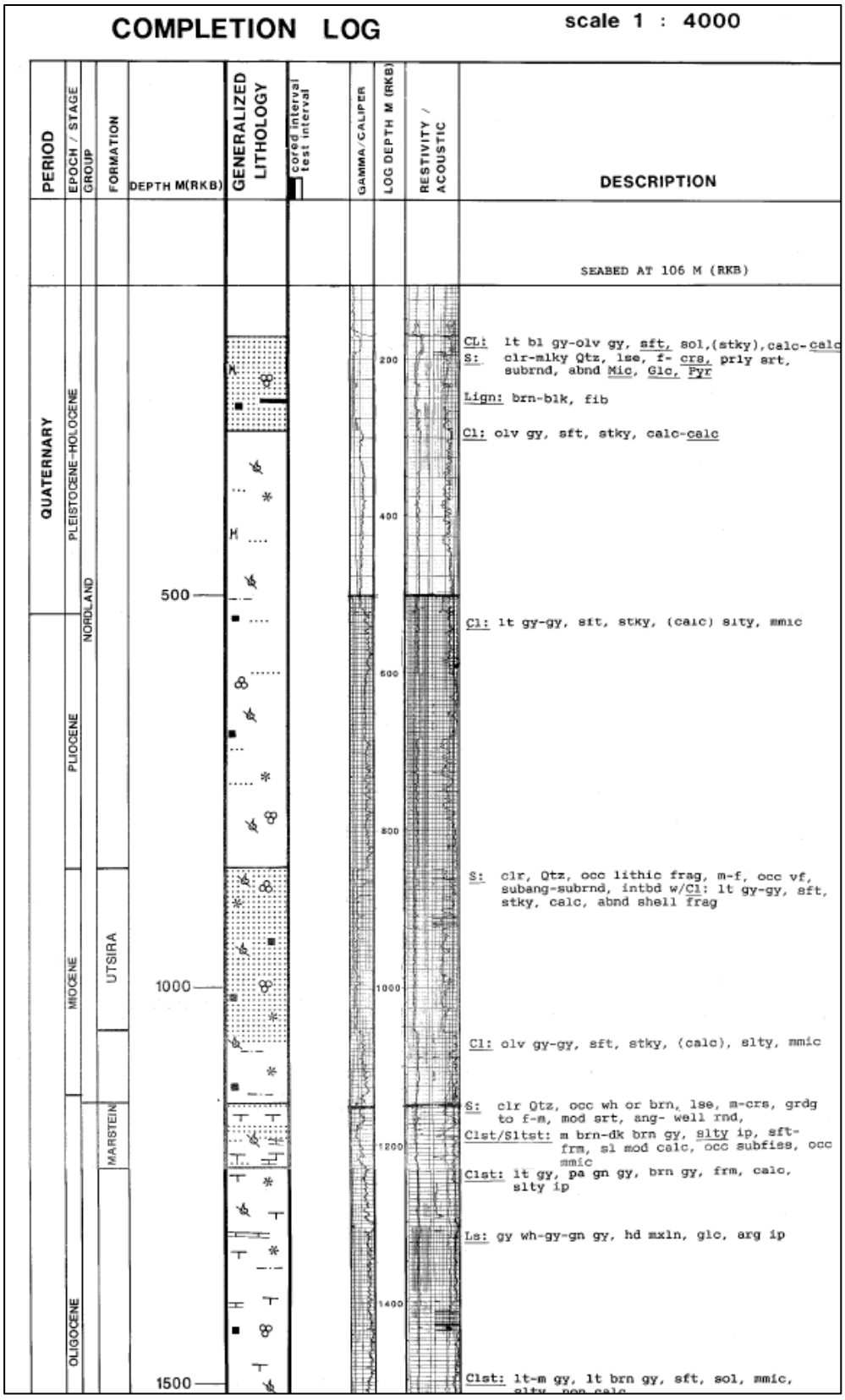

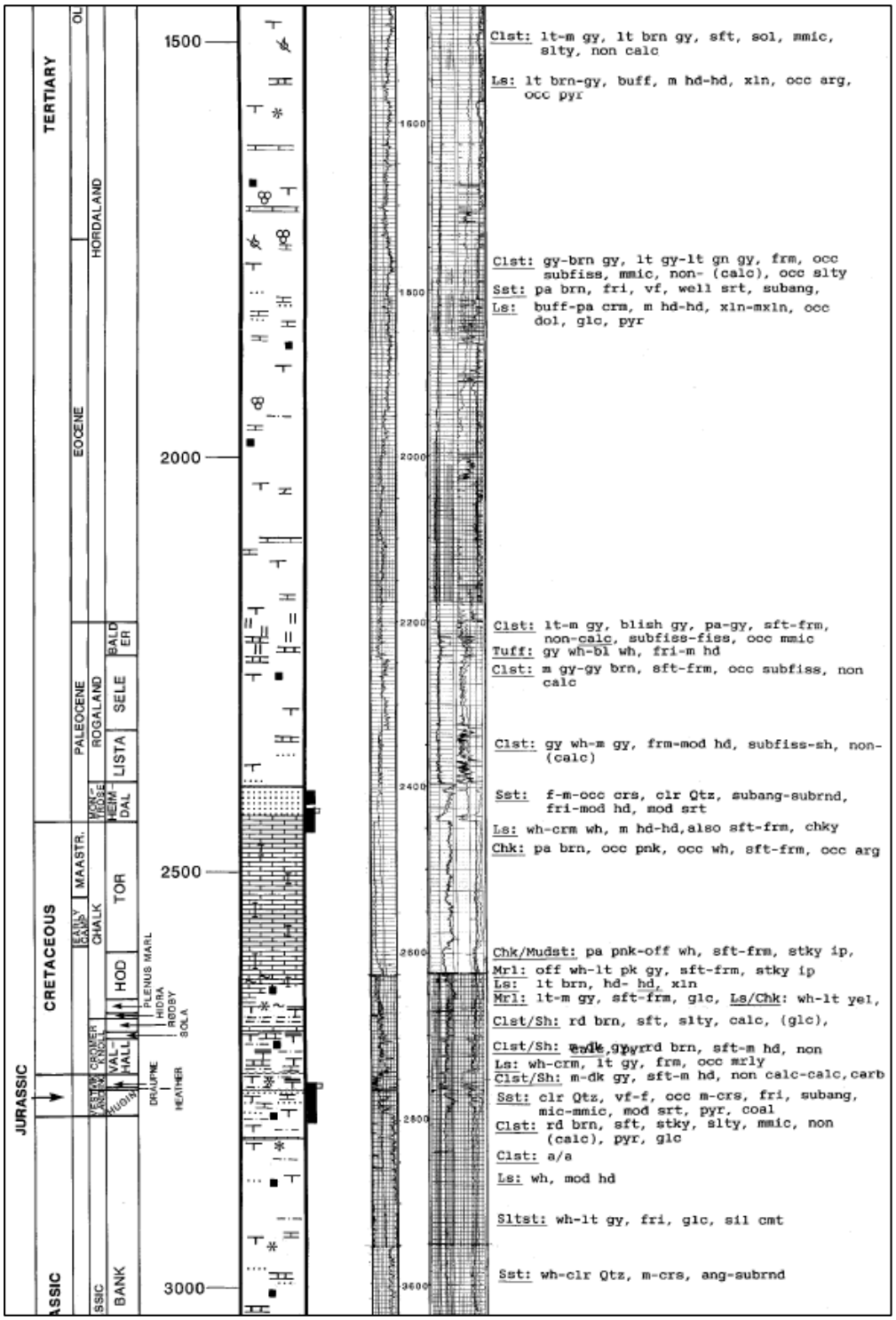
TERTIARY
CRETACEOUS
JURASSIC
EOCENE
PALEOCENE
MAASTR.
CHALK
HORDALAND
ROGALAND
SSIC
BANK
TOR
HOD
LISTA
SELE
BALDER
VAL-HALL
HUGIN
PLENUS MARL
HIDRA
RØDBY
SOLA
DRAUPNE
HEATHER
1500
2000
2500
3000
1600
1800
2000
2200
2400
2600
2800
3600
Clst: lt-m gy, lt brn gy, sft, sol, mmic, slty, non calc
Ls: lt brn-gy, buff, m hd-hd, xln, occ arg, occ pyr
Clst: gy-brn gy, lt gy-lt gn gy, frm, occ subfiss, mmic, non- (calc), occ slty
Sst: pa brn, fri, vf, well srt, subang,
Ls: buff-pa crm, m hd-hd, xln-mxln, occ dol, glc, pyr
Clst: lt-m gy, blish gy, pa-gy, sft-frm, non-calc, subfiss-fiss, occ mmic
Tuff: gy wh-bl wh, fri-m hd
Clst: m gy-gy brn, sft-frm, occ subfiss, non calc
Clst: gy wh-m gy, frm-mod hd, subfiss-sh, non-(calc)
Sst: f-m-occ crs, clr Qtz, subang-subrnd, fri-mod hd, mod srt
Ls: wh-crm wh, m hd-hd,also sft-frm, chky
Chk: pa brn, occ pnk, occ wh, sft-frm, occ arg
Chk/Mudst: pa pnk-off wh, sft-frm, stky ip,
Mrl: off wh-lt pk gy, sft-frm, stky ip
Ls: lt brn, hd- hd, xln
Mrl: lt-m gy, sft-frm, glc, Ls/Chk: wh-lt yel,
Clst/Sh: rd brn, sft, slty, calc, (glc),
Clst/Sh: m-dk gy,rrd brn, sft-m hd, non
Ls: wh-crm, lt gy, frm, occ mrly
Clst/Sh: m-dk gy, sft-m hd, non calc-calc,carb
Sst: clr Qtz, vf-f, occ m-crs, fri, subang, mic-mmic, mod srt, pyr, coal
Clst: rd brn, sft, stky, slty, mmic, non (calc), pyr, glc
Clst: a/a
Ls: wh, mod hd
Sltst: wh-lt gy, fri, glc, sil cmt
Sst: wh-clr Qtz, m-crs, ang-subrnd

Completion log well 15/9-13 (Park et al., 2011), provided by Statoil:

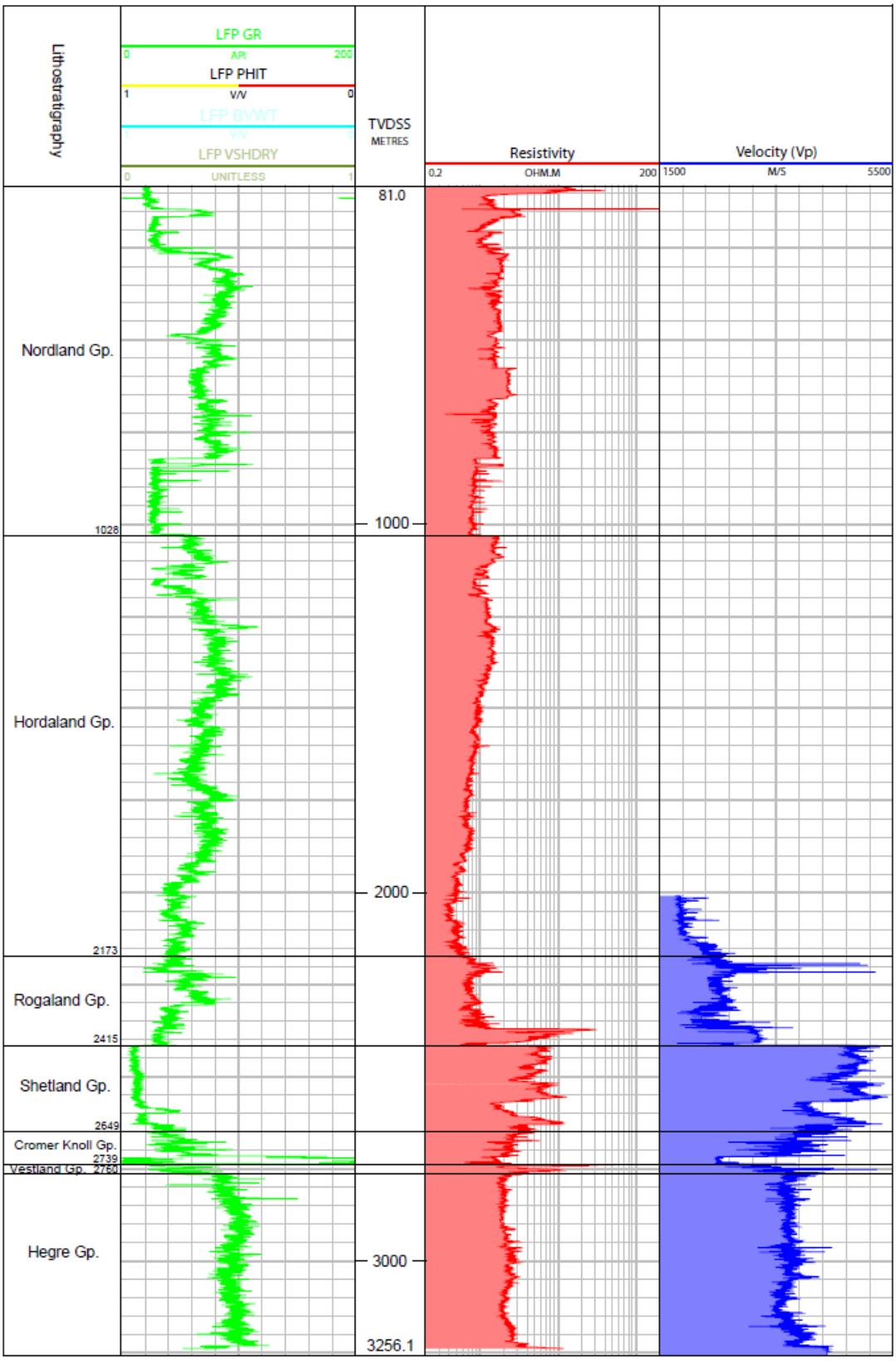

Completion log well 15/9-16 (NPD, 2017)**:**

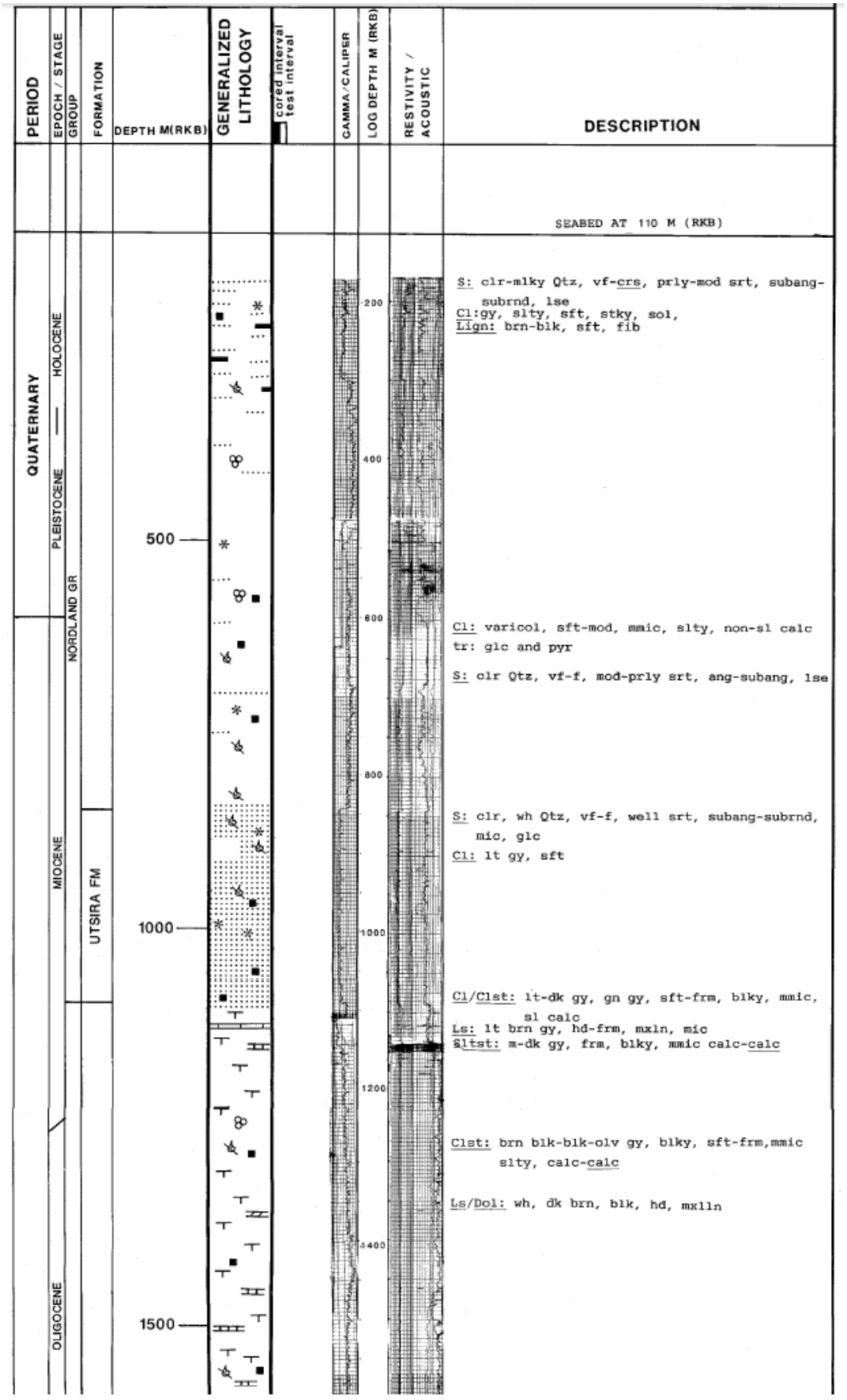

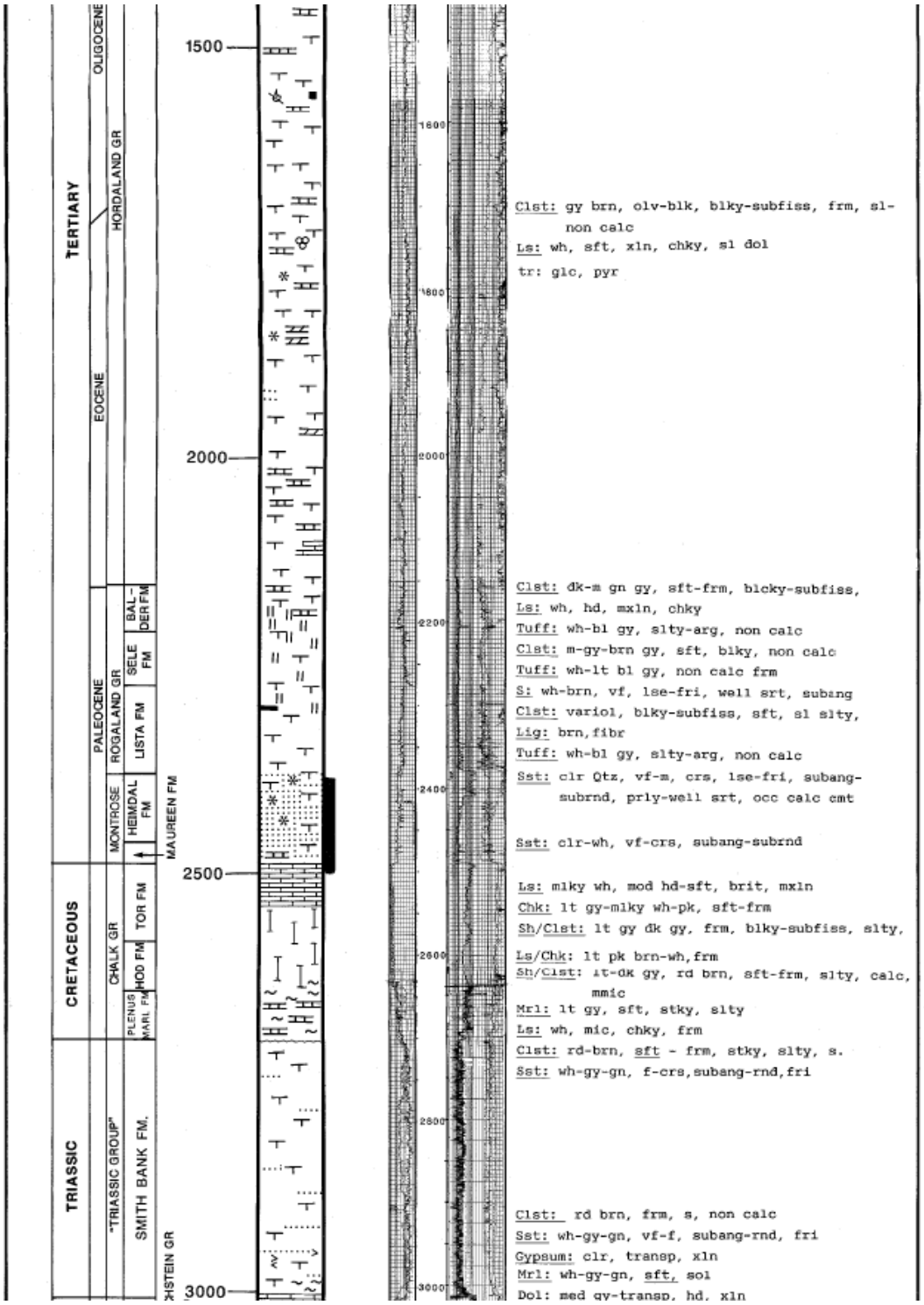
TERTIARY
CRETACEOUS
TRIASSIC
OLIGOCENE
EOCENE
PALEOCENE
HORDALAND GR
ROGALAND GR
MONTROSE
SELE FM
BAL-DER FM
LISTA FM
HEIMDAL FM
MAUREEN FM
CHALK GR
TOR FM
HOD FM
PLENUS MARL FM
"TRIASSIC GROUP"
SMITH BANK FM.
ZECHSTEIN GR
1500
2000
2500
3000
1600
1800
2000
2200
2400
2600
2800
3000
Clst: gy brn, olv-blk, blky-subfiss, frm, sl-non calc
Ls: wh, sft, xln, chky, sl dol
tr: glc, pyr
Clst: dk-m gn gy, sft-frm, blcky-subfiss,
Ls: wh, hd, mxln, chky
Tuff: wh-bl gy, slty-arg, non calc
Clst: m-gy-brn gy, sft, blky, non calc
Tuff: wh-lt bl gy, non calc frm
S: wh-brn, vf, lse-fri, well srt, subang
Clst: variol, blky-subfiss, sft, sl slty,
Lig: brn,fibr
Tuff: wh-bl gy, slty-arg, non calc
Sst: clr Qtz, vf-m, crs, lse-fri, subang-subrnd, prly-well srt, occ calc cmt
Sst: clr-wh, vf-crs, subang-subrnd
Ls: mlky wh, mod hd-sft, brit, mxln
Chk: lt gy-mlky wh-pk, sft-frm
Sh/Clst: lt gy dk gy, frm, blky-subfiss, slty,
Ls/Chk: lt pk brn-wh,frm
Sh/Clst: lt-dk gy, rd brn, sft-frm, slty, calc, mmic
Mrl: lt gy, sft, stky, slty
Ls: wh, mic, chky, frm
Clst: rd-brn, sft - frm, stky, slty, s.
Sst: wh-gy-gn, f-crs,subang-rnd,fri
Clst: rd brn, frm, s, non calc
Sst: wh-gy-gn, vf-f, subang-rnd, fri
Gypsum: clr, transp, xln
Mrl: wh-gy-gn, sft, sol
Dol: med gy-transp, hd, xln